HAL
open science

# Investigation of droplet flame interactions through experimental and numerical approaches

Deniz Kaya Eyice

## To cite this version:

Deniz Kaya Eyice. Investigation of droplet flame interactions through experimental and numerical approaches. Mechanics [physics]. Université d'Orléans; Orta Doğu teknik üniversitesi (Ankara), 2023. English. NNT : 2023ORLE1039 . tel-04019559

**HAL Id: tel-04019559**

**https://cnrs.hal.science/tel-04019559**

Submitted on 8 Mar 2023

**HAL** is a multi-disciplinary open access archive for the deposit and dissemination of scientific research documents, whether they are published or not. The documents may come from teaching and research institutions in France or abroad, or from public or private research centers.

L'archive ouverte pluridisciplinaire **HAL**, est destinée au dépôt et à la diffusion de documents scientifiques de niveau recherche, publiés ou non, émanant des établissements d'enseignement et de recherche français ou étrangers, des laboratoires publics ou privés.

ÉCOLE DOCTORALE

*ÉNERGIE, MATERIAUX, SCIENCES DE LA TERRE ET DE L'UNIVERS*

INSTITUT DE COMBUSTION AÉROTHERMIQUE RÉACTIVITÉ ET ENVIRONNEMENT / DÉPARTEMENT DE L'INGÉNIERIE MÉCANIQUE

**THÈSE EN COTUTELLE INTERNATIONALE** présentée par :


## Deniz KAYA EYICE


soutenue le : 12 Janvier 2023

pour obtenir le grade de :

**Docteur de l'Université d'Orléans**
**et de l'Université Technique du Moyen-Orient (Turquie)**

Discipline/ Spécialité : Mécanique - Énergétique

# Etude des interactions entre gouttelette et flamme par des approches expérimentales et numériques

**THÈSE dirigée par :**

| | |
|---|---|
| **M. CHAUVEAU Christian** | Directeur de Recherche, ICARE-CNRS |
| **M. YOZGATLIGİL Ahmet** | Professeur, Université Technique du Moyen-Orient |
| **M. HALTER Fabien** | Professeur, Université d'Orléans, ICARE-CNRS |
| **M. AKSEL Mehmet Haluk** | Professeur Émérite, Université Technique du Moyen-Orient |

**RAPPORTEURS :**

| | |
|---|---|
| **M. MOUREAU Vincent** | Chargé de Recherche, CORIA-CNRS |
| **M. MURADOĞLU Metin** | Professeur, Université de Koç |

---

**JURY :**

| | |
|---|---|
| **M. MURADOĞLU Metin** | Professeur, Université de Koç |
| **M. MOUREAU Vincent** | Chargé de Recherche, CORIA-CNRS |
| **M. CHAUVEAU Christian** | Directeur de Recherche, ICARE-CNRS |
| **M. YOZGATLIGİL Ahmet** | Professeur, Université Technique du Moyen-Orient |
| **M. HALTER Fabien** | Professeur, Université d'Orléans, ICARE-CNRS |
| **M. İLBAŞ Mustafa** | Professeur, Université de Gazi (Président) |
| **M. BARAN Özgür Uğraş** | Professeur Assistant, Université Technique du Moyen-Orient |
| **M. AKSEL Mehmet Haluk** | Professeur Émérite, Université Technique du Moyen-Orient (Invité) |
| **M. GÖKALP İskender** | Directeur de Recherche Émérite, ICARE-CNRS (Invité) |

to my other half, Kerem

## ACKNOWLEDGMENTS

I would like to present my deepest thanks to all those who gave me the possibility to complete this dissertation as a joint PhD between Middle East Technical University and Université d'Orléans.

First of all, I would like to express my sincerest gratitude to my supervisors at CNRS ICARE; Dr. Christian Chauveau and Prof. Dr. Fabien Halter, for their endless support, motivation, encouragement and all the precious knowledge and advices that they shared with me. It has been a privilege and a great honor to study with such exceptional professors and I am grateful to them for letting me to be a part of their research group. I also would like to present my gratitude to my supervisors at METU; Prof. Dr. Ahmet Yozgatlıgil for his support throughout this study and Prof. Dr. Haluk Aksel for his faith on me since the beginning.

I would like to express my gratitude to Prof. Dr. İskender Gökalp for giving me an opportunity to conduct my PhD studies at CNRS ICARE and for his endless patience and guidance throughout the process of cotutelle. I am grateful to him for allowing me a part of the research community.

I would like to thank the reviewers of this dissertation; Prof. Dr. Metin Muradoğlu for giving his valuable feedbacks and Dr. Vincent Moureau for allowing me to access the code YALES2 and sharing his evaluations on this dissertation. I also want to thank the jury members, Prof. Dr. Mustafa İlbaş, Assoc. Prof. Dr. Barış Yılmaz and Assist. Prof. Dr. Özgür Uğraş Baran for their valuable suggestions and comments.

I also would like to present my gratitude to Dr. Mehmet Karaca for his guidance, encouragement and all the knowledge that he shared with me since the initial phases of this study.

Embassy of France in Turkey is kindly acknowledged for the financial support in joint PhD program between METU and Université d'Orléans under the French Government Scholarship for Cotutelle.

The Scientific and Research Council of Turkey (TÜBİTAK) is also acknowledged for the financial support during this study under the program of BİDEB 2211-C.

I would like to present my sincere thanks to all at CNRS ICARE and to all members of Combustion Turbulente group. I would like to express my special thanks to Antoine Mouze-Mornettas for being the best office mate and all very (also not!) scientific discussions. I also would like to thank Alka Karan, Samuel Jeanjean and Fabian Cano for their friendship and supports in all kind during my stay in France. I also would like to present my thanks to former members of the research group; my predecessor Guillaume Renoux, for the vast heritage of "le projet diphasique", his guidance at the initial phases of this study and all the knowledge he shared with me, and Chaimae Bariki for her kind guidance.

I would like to present my lovely thanks to the people who are beyond being my friends; Berna Sezgin Öztok, Elif Kocaman Tan, Dilara Gülçin Çağlayan, Merve Tufan Köseoğlu and Zeynep Sümer for their priceless friendship throughout my whole university life. I would also like to share my many thanks to Berrak Erkmen, Özge Batır, Özge Şen and Aysu Özden for their lovely friendship.

I also would like to express many thanks to my colleagues at Roketsan YNİTB and specially to Hasan Fatih Çelebi and Başar Burak Özkahya, a.k.a. "The SJ Gurus", for their support during the creation of this dissertation.

I would like to present my sincerest thanks to my lovely mom for her unconditional faith and love under any circumstances. To my father, I know you are proud of me. I am also grateful to my sisters, my brother-in-law, my nephews and my little niece for their priceless love, care and support.

Last but not the least, I would like to express my deepest appreciation to my dear husband, Kerem, who has been there for me since the very beginning and put his faith on me when I could barely find the strength to continue. Thank you for being in my life as my best friend and my everything.

## TABLE OF CONTENTS

ACKNOWLEDGMENTS . . . . . ii

TABLE OF CONTENTS . . . . . iv

LIST OF TABLES . . . . . ix

LIST OF FIGURES . . . . . xi

LIST OF ABBREVIATIONS . . . . . xix

CHAPTERS

1 INTRODUCTION . . . . . 1

1.1 Objectives and Problem Definition . . . . . 3

1.2 Outline of the Thesis . . . . . 4

2 THEORETICAL BACKGROUND . . . . . 5

2.1 Mixture Properties . . . . . 5

2.1.1 Thermodynamics of a Mixture . . . . . 6

2.1.2 Equation of State . . . . . 6

2.2 Transport Modeling . . . . . 6

2.3 Conservation Equations for Reacting Flows . . . . . 7

2.3.1 Mass Conservation . . . . . 7

2.3.2 Species Conservation . . . . . 8

2.3.3 Momentum Equation . . . . . 9

2.3.4 Energy Equation . . . . . 9
2.4 Combustion Modeling . . . . . 10
2.4.1 Chemical Kinetics . . . . . 10
2.4.2 Combustion Regimes . . . . . 12
2.5 Two-Phase Flow Modelling . . . . . 13
2.5.1 Eulerian-Lagrangian Approach . . . . . 14
2.5.2 Evaporation of an Isolated Droplet . . . . . 16
2.5.2.1 Spalding Model . . . . . 16
2.5.2.2 Abramzon-Sirignano Model . . . . . 19
2.5.3 YALES2 Solver . . . . . 19
3 EXPERIMENTAL METHODS . . . . . 21
3.1 Microgravity Experiments: Spherically Expanding Aerosol Flame 21
3.1.1 Parabolic Flights . . . . . 21
3.1.2 Aerosol Setup . . . . . 23
3.1.2.1 Combustion Chamber . . . . . 25
3.1.2.2 Fuel Injection and Chamber Filling . . . . . 25
3.1.2.3 Aerosol Creation . . . . . 27
3.1.2.4 Ignition . . . . . 27
3.1.3 Experimental Procedure . . . . . 28
3.1.4 Experimental Configuration and Conditions . . . . . 28
3.2 Ground Experiments: Stagnation Flame . . . . . 29
3.2.1 Stagnation Burner . . . . . 29
3.2.2 Injector System . . . . . 30

3.2.3 Experimental Configurations and Conditions . . . . . 31
3.2.3.1 Studies on Droplet Evaporation . . . . . 31
3.2.3.2 Studies on Flame Surface Modifications . . . . . 33
3.3 Optical Diagnostics and Post-processing . . . . . 34
3.3.1 Schlieren Visualization . . . . . 34
3.3.2 Chemiluminescence Technique . . . . . 36
3.3.2.1 Local Extinction Phenomenon . . . . . 37
3.3.2.2 Wave Propagation . . . . . 39
3.3.3 Particle Image Velocimetry (PIV) . . . . . 40
3.3.4 Particle Tracking Velocimetry (PTV) . . . . . 41
3.3.5 Interferometric Laser Imaging for Droplet Sizing (ILIDS) 42
4 DROPLET EVAPORATION UNDER FLAME CONDITIONS . . . . 45
4.1 Introduction . . . . . 45
4.1.1 Experimental Studies . . . . . 47
4.1.2 Theoretical and Numerical Studies . . . . . 53
4.1.3 Droplet Evaporation Under Flame Conditions . . . . . 54
4.2 Results and Discussions . . . . . 55
4.2.1 Computation of Flame Characteristics . . . . . 56
4.2.1.1 Stagnation Flame Field Determination . . . . . 60
4.2.2 Stationary Droplet Evaporation . . . . . 61
4.2.2.1 Numerical Setup . . . . . 61
4.2.2.2 Evaporation Under Pure $N_2$ Ambient . . . . . 61
4.2.2.3 Evaporation in the Presence of Burnt Gases . . . . 63

4.2.3 Droplet Injection Through Stagnation Flame Field . . . . 66
4.2.3.1 Numerical Setup . . . . . 66
4.2.3.2 Evaporation Through Laminar $CH_4$/Air Flame . . 68
4.2.3.3 Rate of Evaporation . . . . . 73
4.2.3.4 Droplet Passage Criteria . . . . . 77
4.2.4 Simulations with the Stagnation Burner . . . . . 80
4.2.4.1 Numerical Setup of the Stagnation Burner . . . . . 80
4.2.4.2 Nonreactive Simulations . . . . . 82
4.2.4.3 Reactive Simulations . . . . . 84
4.3 Conclusions . . . . . 91
5 FLAME SURFACE MODIFICATIONS AND INSTABILITIES . . . . 93
5.1 Introduction . . . . . 93
5.1.1 Flame Front Instabilities . . . . . 93
5.1.1.1 Instabilities Due to Gravitational Forces . . . . . 94
5.1.1.2 Hydrodynamic Instabilities . . . . . 94
5.1.1.3 Thermodiffusive Instabilities . . . . . 96
5.1.2 Structural Changes on Flame Front . . . . . 99
5.1.2.1 Local Extinction Phenomenon . . . . . 100
5.2 Results and Discussions . . . . . 101
5.2.1 Interactions of a Spherically Expanding Flame With Aerosol102
5.2.2 Interactions of Stagnation Flame with an Isolated Droplet 106
5.2.2.1 Computation of Flame Characteristics . . . . . 106
5.2.2.2 Variation in Gaseous Phase Properties . . . . . 108

5.2.2.3 Flame Surface Extinction . . . . . 113

5.2.2.4 Wave Propagation on Flame Surface . . . . . 122

5.3 Conclusions . . . . . 133

6 CONCLUSIONS AND REMARKS . . . . . 137

6.1 Conclusions . . . . . 137

6.2 Remarks and Future Studies . . . . . 139

REFERENCES . . . . . 141

APPENDICES

A CHANGE IN GAS PROPERTIES IN 2D STAGNATION FLAME SIMULATIONS . . . . . 155

## LIST OF TABLES

TABLES

Table 3.1 Experimental conditions performed in aerosol chamber (AC) for $C_2H_5OH$/air spherically-expanding aerosol flames. . . . . 29

Table 3.2 Experimental conditions performed in stagnation burner (SB) for $CH_4$/air premixed stagnation flames with ethanol droplet for evaporation studies. . . . . 32

Table 3.3 Experimental conditions performed in stagnation burner (SB) for $C_3H_8$/air premixed stagnation flames with ethanol droplet for flame morphology studies. . . . . 34

Table 4.1 Parameters of 1D freely propagating adiabatic $CH_4$/air flame computed with the San Diego mechanism [115] at 300 K, 1 atm. . . 57

Table 4.2 Change in flame parameters with stagnation wall temperature, $T_{plate}$ for SBM-1. . . . . 58

Table 4.3 Parameters of 1D stagnation $CH_4$/air flame computed with the San Diego mechanism [115] at 300 K, 1 atm ($T_{plate}$=500 K). . . . . 59

Table 4.4 Coefficients of an exponential relation for evaporation constant, $K$ depending on $T_{gas,average}$. . . . . 76

Table 4.5 Coefficients of an exponential relation for evaporation constant, $K$ depending on flame parameters. . . . . 77

Table 4.6 Critical diameter values of ethanol droplets to cross the flame zone. . . . . 79

Table 4.7 Boundary conditions of the 2D stagnation burner simulations at $T$=300 K and $P$=1 atm. . . . . 81

Table 4.8 Comparison of evaporation behavior under different flame characteristics at MR-1 and MR-2 for an isolated ethanol droplet with $d_{p,0}$=50 $\mu$m. . . . . 90

Table 5.1 Parameters of 1D stagnation $C_3H_8$/air flame computed with the San Diego mechanism [115] ($T_{plate}$=500 K). . . . . 107

Table 5.2 Experimentally determined properties of a propagating wave on the flame surface after droplet passage. . . . . 129

## LIST OF FIGURES

FIGURES

Figure 1.1 Fundamental processes in spray combustion [107]. . . . . 2

Figure 2.1 (a) Premixed and (b) diffusion flame structures. . . . . 12

Figure 2.2 Flame thickness definitions for premixed flames [78]. . . . . 12

Figure 2.3 Temperature and mass fraction profiles from liquid through gas phase. . . . . 17

Figure 3.1 Airbus A310 ZERO-G airplane and durations of different gravity levels during the parabolic flights. . . . . 22

Figure 3.2 Measurement of accelerations on board A310 ZERO-G (VP158, flight 1, parabola 6) – Novespace data. . . . . 23

Figure 3.3 Photograph of the experimental device in flight configuration on board A310 ZERO-G with Schlieren configuration. . . . . 24

Figure 3.4 Experimental setup with Schlieren configuration. . . . . 25

Figure 3.5 Gas flowpath diagram of the experimental setup. . . . . 26

Figure 3.6 Schematic of the stagnation burner. . . . . 30

Figure 3.7 Schematic of the injection system. . . . . 31

Figure 3.8 Experimental configuration of stagnation burner with PIV/PTV and ILIDS for evaporation studies. . . . . 32

Figure 3.9 Experimental configuration of stagnation burner with chemiluminescence and ILIDS for flame morphology. . . . . 33

Figure 3.10 Schematic of a Schlieren setup. . . . . 35

Figure 3.11 Chemiluminescence spectrum of a hydrocarbon flame [4]. . 36

Figure 3.12 Chemiluminescence image of $C_3H_8$/air flame at SBP-4 with the region of interest (yellow) having different sizes depending on the flame thickness and initial droplet size. . . . . 37

Figure 3.13 Intensity measurement on the flame to update the ROI according to the flame position (a) Perpendicular line (green) (b) Change in intensity on the line. . . . . 38

Figure 3.14 Detection of the properties of a propagating wave on the flame surface. . . . . 39

Figure 3.15 Determination of (a) the flame front and (b) the velocity of unburnt gases based on PIV. . . . . 41

Figure 3.16 Determination of the trajectory of droplet based on PTV ($d_{p,0}$=35 $\mu$m). . . . . 42

Figure 3.17 The principle of ILIDS. . . . . 43

Figure 3.18 Combined sequence of ILIDS images illustrating the evaporation of a droplet while passing through the flame front (droplet diameters from bottom to top; 49 $\mu$m, 49 $\mu$m, 38 $\mu$m and 15 $\mu$m). 44

Figure 4.1 The interaction levels of a flame front and a spray; (a) Pre-evaporation (b) Homogeneous (c) Heterogeneous [86]. . . . . 46

Figure 4.2 Cross quartz fiber supporting technique for droplet evaporation [91]. . . . . 48

Figure 4.3 Sequence of droplet motion during free-falling [119]. . . . . 49

Figure 4.4 Temperature distribution inside an individual droplet captured via LIF technique [16]. . . . . 52

Figure 4.5 Comparison of unstretched $CH_4$/air flamespeeds measured by Halter et al. [34] and computed with GriMech 3.0 and San Diego [115] mechanisms at 300 K, 1 atm. . . . . 57

Figure 4.6 Comparison of 1D freely propagating adiabatic flame and 1D stagnation flame at SBM-3 (a) Velocity profile (b) Temperature profile. . . . . 59

Figure 4.7 Fitted stagnation temperature profile and droplet trajectory for SBM-1 with an ethanol droplet trajectory ($d_{p,0}$=47 $\mu$m). . . . 60

Figure 4.8 Computational domain of a stationary droplet evaporation. 61

Figure 4.9 Comparison of ethanol droplet evaporation from the experiments of Saharin et al. [91] and simulations via Spalding model under pure $N_2$ ambient at $P$=1 atm and at (a) low temperatures (b) high temperatures. . . . . 62

Figure 4.10 Temporal evolution of droplet diameter with ILIDS ($d_{p,0}$=47 $\mu$m, $T_{evap,average}$=2020.5±2.5 K) and Spalding model ($d_{p,0}$=50 $\mu$m, $T_\infty$=2000 K) in stagnant ambient conditions (SBM-3). . . . . 63

Figure 4.11 Temporal evolution of droplet parameters in the stoichiometric conditions (SBM-3) (a) Droplet temperature (b) Spalding numbers (c) Mass evaporation rate (d) Heat evaporation rate. . . 65

Figure 4.12 Sketch of the computational domain for 2D $CH_4$/air stagnation flame (SBM-1, $T_{plate}$=500 K). . . . . 67

Figure 4.13 Temporal evolution of computed and measured (a) gas and (b) droplet velocities at SBM-3 ($d_{p,0}$=50 $\mu$m). . . . . 68

Figure 4.14 Temporal evolution of particle Reynolds number at SBM-3 ($d_{p,0}$=50 $\mu$m). . . . . 70

Figure 4.15 (a) Spatial and (b) temporal evolution of droplet diameter with ILIDS and Abramzon-Sirignano model at SBM-3 ($d_{p,0}$=50 $\mu$m). 71

Figure 4.16 Temporal evolution of droplet parameters at stoichiometric conditions for an ethanol droplets having $d_{p,0}$=35, 50 and 65 $\mu$m (a) Droplet temperature (b) Spalding numbers (c) Mass evaporation rate (d) Heat evaporation rate. . . . . 72

Figure 4.17 Temporal evolution of droplet parameters at different flame conditions for an ethanol droplet having $d_{p,0}$=50 $\mu$m (a) Droplet temperature (b) Spalding numbers (c) Mass evaporation rate (d) Heat evaporation rate. . . . . 73

Figure 4.18 Changes in ethanol evaporation constant with respect to the initial droplet diameter at different equivalence ratios. . . . . 74

Figure 4.19 Comparison of ethanol evaporation constant with respect to ambient gas temperature. . . . . 75

Figure 4.20 Computed $Da_v$ numbers for all droplets. . . . . 78

Figure 4.21 The distance that the droplet travels after entering the flame zone ($T$=525 K) for all the droplets. . . . . 79

Figure 4.22 Sketch of the computational domain for the 2D stagnation burner. . . . . 80

Figure 4.23 (a) 2D computational domain with M3 (510K elements and 100 $\mu$m grid size at the flame zone) (b) Axial velocity profiles at the burner exit with M1, M2 and M3 meshes for MNR-1. . . . . 82

Figure 4.24 Velocity fields of (a) MNR-1 and (b) MNR-2 (c) Radial velocity profiles at the burner exit. . . . . 83

Figure 4.25 Streamlines and regions of stabilized stagnation flame at MR-1. . . . . 84

Figure 4.26 Velocity fields of (a) MR-1 and (b) MR-2 (c) Radial velocity profiles at the burner exit and (d) Axial velocity profiles between burner exit and the stagnation plate. . . . . 86

Figure 4.27 Temperature fields of (a) MR-1 and (b) MR-2 (d) Axial temperature profiles between burner exit and the stagnation plate. 87

Figure 4.28 Reaction rate fields of (a) MR-1 and (b) MR-2 (c) Axial profiles of $\dot{\omega}_{CH_4}$ between the burner exit and stagnation plate. . . 88

Figure 4.29 (a) Spatial and (b) temporal evolution of droplet diameter with the Abramzon-Sirignano model at MR-1 and MR-2 ($d_{p,0}$=50 $\mu$m). . . . . 90

Figure 5.1 A schematic illustration of instabilities due to gravitational forces. . . . . 94

Figure 5.2 A schematic illustration of hydrodynamic instabilities. . . . 95

Figure 5.3 A schematic illustration of thermodiffusive instabilities (a) $Le$<1, destabilizing effect (b) $Le$>1, stabilizing effect. . . . . 98

Figure 5.4 OH PLIF of the passage of an acetone droplet (200 $\mu$m) through methane/air diffusion flame (a) Droplet with higher $u_p$ (without ignition) (b) Droplet with lower $u_p$ (ignition) [59]. . . . . 100

Figure 5.5 Schlieren images of equivalent flames at AC-1 (a) Gaseous flame at ground conditions (6.2 ms after ignition) (b) Two-phase flame at ground conditions (6.4 ms after ignition) (c) Aerosol flame under microgravity (10.8 ms after ignition). . . . . 102

Figure 5.6 Comparison of (a) shadowgraphy [83], (b) CH* chemiluminescence [83] and (c) Schlieren images of equivalent flames and at a radius of 13.5 mm (aerosol ethanol/air flame at AC-1). . . . . 104

Figure 5.7 Formation of instabilities on the flame surface due to the presence of droplets (aerosol ethanol/air flame at AC-1). . . . . 105

Figure 5.8 Variation in global and effective Lewis numbers for propane/air flame at 300 K and 1 atm. . . . . 107

Figure 5.9 Variation in (a) $C_2H_5OH$ mass fraction and (b) $C_2H_5OH$ reaction source term on the isoline of droplet along $x$-axis through the flame at SBM-3. . . . . 108

Figure 5.10 Variation in (a) $C_2H_5OH$ mass fraction and (b) $C_2H_5OH$ reaction source term at the flame over time at SBM-3. . . . . 109

Figure 5.11 Variation in $C_2H_5OH$ and $CH_4$ mass fractions at the centerline of the domain through the flame. . . . . 110

Figure 5.12 Variation in $C_2H_5OH$ and $CH_4$ reaction source terms at the centerline of the domain through the flame. . . . . 111

Figure 5.13 Variation in temperature profile from the burner exit to the stagnation plate while the ethanol droplet having (a,b) $d_{p,0}$=50 $\mu$m and (c,d) $d_{p,0}$=250 $\mu$m is passing through the flame at MR-1. . . . 113

Figure 5.14 Variation in integral of signal on time due to droplet passage ($d_{p,0}$=48.5 $\mu$m) at SBP-5 with constant position ROI. . . . . 115

Figure 5.15 Variation in integral of signal on time due to droplet passage ($d_{p,0}$=48.5 $\mu$m) at SBP-5 with moving ROI. . . . . 116

Figure 5.16 Variation in integral of signal on time due to droplet passage ($d_{p,0}$=51.9 $\mu$m) at SBP-4 with constant position ROI. . . . . 117

Figure 5.17 Variation in integral of signal on time due to droplet passage ($d_{p,0}$=51.9 $\mu$m) at SBP-4 with moving ROI. . . . . 118

Figure 5.18 Variation in integral of signal on time due to droplet passage ($d_{p,0}$=58.9 $\mu$m) at SBP-3 with constant position ROI. . . . . 119

Figure 5.19 Variation in integral of signal on time due to droplet passage ($d_{p,0}$=58.9 $\mu$m) at SBP-3 with moving ROI. . . . . 120

Figure 5.20 Variation in integral of signal on time due to droplet passage ($d_{p,0}$=55.4 $\mu$m) at SBP-2 with constant position ROI. . . . . 121

Figure 5.21 Variation in integral of signal on time due to droplet passage ($d_{p,0}$=55.4 $\mu$m) at SBP-2 with moving ROI. . . . . 122

Figure 5.22 Propagation of a wave on the flame surface after the droplet passage at SBP-4 with ethanol droplet ($d_{p,0}$=51.93 $\mu$m) ($t$=0 ms: initially stable gaseous flame, $t$=2.8 ms: ethanol droplet passage through the flame front, $t$=4.1-10.6 ms: wave propagation on the flame surface, $t$=11.9 ms: recovered and stable gaseous flame). . . 123

Figure 5.23 Continuous time sinusoidal signal. . . . . 124

Figure 5.24 Variation of wavelength of the perturbation over time at (a) SBP-3, (b) SBP-4 and (c) SBP-5 for propane/air flames. . . . . 125

Figure 5.25 Variation of amplitude of the perturbation over time at (a) SBP-3, (b) SBP-4 and (c) SBP-5 for propane/air flames. . . . . 126

Figure 5.26 Variation of velocity of the perturbation over time at (a) SBP-3, (b) SBP-4 and (c) SBP-5 for propane/air flames. . . . . 128

Figure 5.27 Variation of frequency of the perturbation over time at (a) SBP-3, (b) SBP-4 and (c) SBP-5 for propane/air flames. . . . . 129

Figure 5.28 Propagation of the wave on the flame surface in time. . . . 130

Figure 5.29 Growth rate of (a) measured perturbations due to droplet passage and (b) perturbations at different wavelengths at SBP-3. . 131

Figure 5.30 Growth rate of (a) measured perturbations due to droplet passage and (b) perturbations at different wavelengths at SBP-4. . 132

Figure 5.31 Growth rate of (a) measured perturbations due to droplet passage and (b) perturbations at different wavelengths at SBP-5. . 132

Figure A.1 Variation in gas temperature at the flame over time. . . . . 155

Figure A.2 Variation in $C_2H_5OH$ mass fraction at the flame over time. 156

Figure A.3 Variation in $CH_4$ mass fraction at the flame over time. . . 157

Figure A.4 Variation in $O_2$ mass fraction at the flame over time. . . . 158

Figure A.5 Variation in $CH_4$ reaction source term at the flame over time. 159

Figure A.6 Variation in $C_2H_5OH$ reaction source term at the flame over time. . . . . 160

## LIST OF ABBREVIATIONS

| | |
|---|---|
| 1D | 1 Dimensional |
| 2D | 2 Dimensional |
| 3D | 3 Dimensional |
| AC | Aerosol Chamber |
| AS | Abramzon-Sirignano |
| CFD | Computational Fluid Dynamics |
| CFL | Courant–Friedrichs–Lewy |
| CHP | Chambre Haute Pression |
| CNES | Centre National d'Études Spatiales |
| CNRS | Centre National de la Recherche Scientifique |
| CORIA | Complexe de Recherche Interprofessionnel en Aérothermochimie |
| DEHS | Diethylhexyl-sebacate |
| DFT | Discrete Fourier Transform |
| DNS | Direct Numerical Simulation |
| ICARE | Institut de Combustion, Aérothermique, Réactivité et Environnement |
| IHP | Insert Haute Pression |
| ILIDS | Interferometric Laser Imaging for Droplet Sizing |
| KLT | Kanade-Lucas-Tomas |
| LES | Large Eddy Simulation |
| LIEF | Laser Induced Exciplex Fluorescence |
| LIF | Laser Induced Florescence |
| METU | Middle East Technical University |

| | |
|---|---|
| MNR | Methane - Nonreactive |
| MR | Methane - Reactive |
| PDA | Phase Doppler Anemometry |
| PID | Proportional–Integral–Derivative |
| PIV | Particle Image Velocimetry |
| PLIF | Planar Laser Induced Florescence |
| PSD | Power Spectral Density |
| PTV | Particle Tracking Velocimetry |
| ROI | Region of Interest |
| SB | Stagnation Burner |
| SBM | Stagnation Burner - Methane |
| SBP | Stagnation Burner - Propane |
| VDS | Variable Density Solver |
| VOF | Volume of Fluid |

# CHAPTER 1

# INTRODUCTION

Combustion is one of the oldest and the most essential technology in humankind's history. It will remain a key technology in the future due to the need for high energy demand in different applications such as heating, transportation, and energy production.

Today, the combustion of fossil fuels creates concerns about sustainability and environment. Pollutants produced by combustion are unburnt and partially burned hydrocarbons, nitrogen oxides ($NO_x$), carbon monoxide, sulfur oxides ($SO_x$), and particulate matter in various forms which cause serious health hazards, ozone depletion, etc. [76]. Also, carbon dioxide ($CO_2$) emissions have been proven to cause substantial changes in the climate, being one of the main greenhouse gases. These problems can only be avoided by designing cleaner, more efficient, and safer combustion systems. Because of the complexity in the design and operating conditions of the combustion systems and stability issues due to the complex dynamics of the flow and combustion interactions, it is necessary to achieve a detailed understanding of the combustion phenomenon.

Spray combustion occurs in various industrial applications such as internal combustion engines, gas turbine combustion, liquid-fueled rockets, and burners. The basic representation of spray combustion systems is given in Figure 1.1.

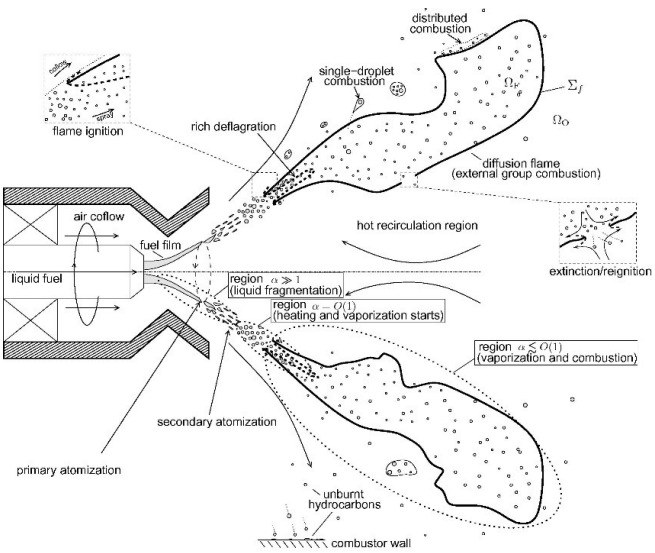


Figure 1.1: Fundamental processes in spray combustion [107].

In spray combustion systems, sprays are the results of high-pressure-driven hydrocarbon or any liquid fuels injected through one or several injectors into a combustion chamber. The jet atomizes into liquid fragments during a primary liquid break-up and, finally, into droplets during a secondary break-up. Then, it evaporates producing vapor and mixing with the oxidizer, forming a combustible mixture. After that, it ignites and, thus, initiates the combustion process. The combustion process proceeds in the form of a diffusion flame.

As it is seen from Figure 1.1, two-phase combustion is a very complex phenomenon involving many processes; atomization, droplet vaporization, mixing, turbulence, and chemical kinetics, as well as the interaction of these processes. These interactions have already been extensively studied even if the conditions were limited to restricted thermodynamic domains, and still there are many points to be clarified.

In industrial applications, high evaporation rates and mixing of liquid fuel with the gas phase are desired for high energy efficiency. Several droplet-droplet, droplet-turbulence, and droplet-flame interactions are observed in real-life applications. Among all situations occurring in combustion chambers, one of the fundamental processes is the interaction of a single droplet with a flamelet that is laminar and locally 1D structures of the flame. Additionally, it should be

emphasized that the combustion process involves chemical reactions that only occur in the gaseous phase [64]. Therefore, it is crucial to obtain the evaporation properties of liquid fuels in order to design atomizers and combustion chambers more efficiently. It is also known that the presence of liquid fuels may cause flame instabilities leading to failure and extinction of flame during the application. Hence, the effect of the presence of liquid droplets on the flame morphology is as important as their evaporation characteristics.

## 1.1 Objectives and Problem Definition

The main purpose of this study is to investigate the droplet and flame interactions with canonical experimental and numerical approaches to deepen the understanding of one of the fundamental processes occurring in combustion chambers; single droplet and flamelet interaction.

The experimental part of the study is conducted at CNRS ICARE after the thesis of G. Renoux [82]. Evaporation studies are carried out with an isolated ethanol droplet injection through methane/air stagnation flame at lean, stoichiometric, and rich conditions via several laser diagnostics to provide a validated database for alcohol evaporation at elevated conditions. After the identification of flame characteristics in the presence of droplets experimentally and numerically, the changes in the flame morphology due to the passage of droplets are evaluated. For this purpose, first, microgravity experiments are conducted during the parabolic flights of CNES with spherically expanding aerosol flame to qualitatively understand the onset of instabilities. Secondly, structural changes in rich propane/air stagnation flames due to the interaction with an isolated ethanol droplet are investigated. For the numerical simulations, the YALES2 solver from CNRS CORIA is utilized to compute single droplet evaporation under a quiescent, hot atmosphere and at flame conditions with burner geometry via Lagrangian evaporation models.

## 1.2 Outline of the Thesis

The thesis is organized as follows:

- **Chapter 2**: Basic concepts in reacting flows, as well as the evaporating spray equations, are introduced.
- **Chapter 3**: Experimental configurations and conditions to analyze droplet-flame interactions are reported. Fundamentals of the performed optical diagnostics and the post-processing are explained.
- **Chapter 4**: Analysis of an isolated ethanol droplet evaporation interacting with a flat, laminar methane/air flame is performed with the interpretations of experiments and numerical simulations. The dependence of vaporization rate on flame properties, as well as the droplet passage criteria, is proposed at different flame conditions.
- **Chapter 5**: Influences of the droplets on the flame surface morphology are studied with two different experimental approaches. The evidence of local extinction on the flame surface due to the droplet passage is interpreted, and resulted propagating wave properties are quantified.
- **Conclusions and Remarks**: Main interpretations on the evaporation of an isolated droplet through the stagnation flame and the flame morphology changes due to the presence of droplets are concluded. Complementary materials related to the computations are reported in the Appendix section.

# CHAPTER 2

# THEORETICAL BACKGROUND

This chapter reports the fundamental concepts and equations describing the reacting multi-phase gaseous flows. The evaporation models used in this study are summarized. Simulations of isolated droplet evaporation through a reactive ambient are performed with the YALES2 solver without any implementations.

## 2.1 Mixture Properties

In a mixture of $N$ species, the mass fraction for species $k$, $Y_k$ is defined as:

$$Y_k = \frac{m_k}{m}, \qquad \sum_{k=1}^{N} Y_k = 1 \tag{2.1}$$

where $m_k$ is the mass of species $k$ and $m$ is the total mass of mixture.

The mole fraction for species $k$, $X_k$ can also be defined as:

$$X_k = \frac{n_k}{n}, \qquad \sum_{k=1}^{N} X_k = 1 \tag{2.2}$$

where $n_k$ is the mole of species $k$ and $n$ is the total number of moles.

The relation between mass and mole fractions can be written as:

$$Y_k = \frac{X_k W_k}{W} \tag{2.3}$$

where $W_k$ is the molecular weight of species $k$ and $W$ is the molecular weight of mixture:

$$W = \sum_{k=1}^{N} X_k W_k = \left[ \sum_{k=1}^{N} \frac{Y_k}{W_k} \right]^{-1} \tag{2.4}$$

### 2.1.1 Thermodynamics of a Mixture

Total enthalpy of species $k$, $h_k$ is defined as the summation of sensible enthalpy, $h_{s,k}$ and enthalpy of formation, $\Delta h^0_{f,k}$:

$$h_k = h_{s,k} + \Delta h^0_{f,k} \tag{2.5}$$

The sensible enthalpy for species $k$ can be defined as:

$$h_{s,k} = \int_{T_0}^{T} C_p^k \, dT \tag{2.6}$$

where $T_0 = 300$ K is the reference temperature and $C_p^k$ is the heat capacity of species $k$ and it can be calculated using NASA polynomials as:

$$\frac{C_p^k(T, P_0)}{R} = \alpha_{1,k} + \alpha_{2,k}T + \alpha_{3,k}T^2 + \alpha_{4,k}T^3 + \alpha_{5,k}T^4 \tag{2.7}$$

where $T$ is the temperature and $R$ is the universal gas constant, 8.314 J/molK in SI units.

### 2.1.2 Equation of State

The gaseous mixture is assumed to be ideal. The relation between pressure, $P$, density, $\rho$ and temperature, $T$ is given as follows:

$$P = \frac{\rho R T}{W} \tag{2.8}$$

## 2.2 Transport Modeling

The dynamic viscosity of mixture, $\mu$ is calculated by the Wilke model [7]:

$$\mu = \sum_{k=1}^{N} \frac{X_k \mu_k}{\sum_i \Phi_{ki}}, \text{ with } \quad \Phi_{ki} = \frac{1}{\sqrt{8}\sqrt{1 + W_k/W_i}} \left(1 + \sqrt{\frac{\mu_i}{\mu_k}} \left(\frac{W_k}{W_k}\right)^{1/4}\right)^2 \tag{2.9}$$

The thermal conductivity of mixture, $\lambda$ is computed from the Brocaw formulation [13]:

$$\lambda = \frac{1}{2} \left[ \sum_{k=1}^{N} X_k \lambda_k + \left( \sum_{k=1}^{N} \frac{X_k}{\lambda_k} \right)^{-1} \right] \tag{2.10}$$

Critical dimensionless numbers can be defined as:

**- Prandtl number;** the ratio between momentum diffusivity and thermal diffusivity:

$$Pr = \frac{\mu}{\lambda/\rho C_p} \tag{2.11}$$

**- Lewis number;** the ratio between thermal diffusivity and mass diffusivity:

$$Le_k = \frac{\lambda}{\rho C_p D_k} \tag{2.12}$$

**- Schmidt number;** the ratio between momentum diffusivity and mass diffusivity:

$$Sc_k = \frac{\mu}{\rho D_k} = PrLe_k \tag{2.13}$$

## 2.3 Conservation Equations for Reacting Flows

Multi-species reacting Navier-Stokes equations are briefly reported as follows [78]:

### 2.3.1 Mass Conservation

The mass conservation in a control volume leads to continuity equation and it can be written for unsteady compressible flow as:

$$\frac{\partial \rho}{\partial t} + \frac{\partial \rho u_i}{\partial x_i} = 0 \tag{2.14}$$

where $u_i$ is the three dimensional velocity field. Note that the repeating index, $i$ implies a summation over it, also known as Einstein summation rule.

### 2.3.2 Species Conservation

In multi-species reacting flows, the mixture is composed of different chemical species. The local mass fraction of species changes by convective and diffusive transport and chemical reactions. For each species $k$, mass conversion is written as:

$$\frac{\partial \rho Y_k}{\partial t} + \frac{\partial}{\partial x_i}\rho(u_i + V_{k,i})Y_k = \dot{\omega}_k \tag{2.15}$$

where $V_{k,i}$ is the $i^{th}$ component of the diffusion velocity vector of the species $k$ and $\dot{\omega}_k$ is the reaction rate.

Summation of species equation for all species leads to:

$$\frac{\partial \rho}{\partial t} + \frac{\partial \rho u_i}{\partial x_i} = -\frac{\partial}{\partial x_i}\left(\rho \sum_{k=1}^{N} V_{k,i} Y_k\right) + \sum_{k=1}^{N} \dot{\omega}_k \tag{2.16}$$

The left hand side of the equation corresponds to the conservation of mass; hence, it is equal to zero. The reaction rate must satisfy the following relation to ensure species mass conservation:

$$\sum_{k=1}^{N} \dot{\omega}_k = 0 \tag{2.17}$$

which yields the constraint for the diffusion velocity necessary to be satisfied:

$$\sum_{k=1}^{N} V_{k,i} Y_k = 0 \tag{2.18}$$

The Hirschfelder & Curtiss mixture-averaged approximation for multi-species gas transport makes it possible to write the molecular diffusion of a species as a function of the composition and the species diffusion coefficients [41]:

$$V_k X_k = -D_k \nabla X_k, \qquad \text{with} \qquad D_k = \frac{1 - Y_k}{\sum_{j \neq k} X_j / \mathcal{D}_{jk}} \tag{2.19}$$

where $D_k$ is the mixture-averaged diffusion coefficient of species $k$ and $\mathcal{D}_{jk}$ is the binary diffusion coefficient between species $k$ and $j$. Hence, the species equation becomes:

$$\frac{\partial \rho Y_k}{\partial t} + \frac{\partial \rho u_i Y_k}{\partial x_i} = \frac{\partial}{\partial x_i}\left(\rho D_k \frac{W_k}{W}\frac{\partial X_k}{\partial x_i}\right) + \dot{\omega}_k \tag{2.20}$$

The summation of species equations must comply with the mass conservation. However, in the mixture averaged approach, the term $\frac{\partial}{\partial x_i}\left(\rho \sum_{k=1}^{N} D_k \frac{W_k}{W}\frac{\partial X_k}{\partial x_i}\right)$ is not equal to zero. In order to overcome this issue, correction velocity is introduced for diffusion velocity:

$$V_{k,i} = -\frac{D_k}{X_k}\frac{\partial X_k}{\partial x_i} + V_i^c, \qquad \text{with} \qquad V_i^c = \sum_{k=1}^{N} D_k \frac{W_k}{W}\frac{\partial X_k}{\partial x_i} \tag{2.21}$$

Consequently, species equation with the Hirschfelder & Curtiss approximation becomes:

$$\frac{\partial \rho Y_k}{\partial t} + \frac{\partial \rho u_i Y_k}{\partial x_i} = \frac{\partial}{\partial x_i}\left(\rho D_k \frac{W_k}{W}\frac{\partial X_k}{\partial x_i} - \rho V_i^c Y_k\right) + \dot{\omega}_k \tag{2.22}$$

### 2.3.3 Momentum Equation

Newton's second law of motion provides the following relation for momentum conservation:

$$\frac{\partial \rho u_j}{\partial t} + \frac{\partial \rho u_i u_j}{\partial x_i} = -\frac{\partial P}{\partial x_j} + \frac{\partial \tau_{ij}}{\partial x_i} \tag{2.23}$$

where $P$ is the static pressure and $\tau_{ij}$ is the viscous stress tensor that can be expressed as:

$$\tau_{ij} = -\frac{2}{3}\mu \frac{\partial u_m}{\partial x_m}\delta_{ij} + \mu\left(\frac{\partial u_i}{\partial x_j} + \frac{\partial u_j}{\partial x_i}\right) \tag{2.24}$$

where $\delta_{ij}$ is the Kronecker symbol: $\delta_{ij} = 1$ if $i = j$ and 0 otherwise.

### 2.3.4 Energy Equation

Energy conservation in total energy form can be expressed as:

$$\frac{\partial \rho e_t}{\partial t} + \frac{\partial \rho u_i e_t}{\partial x_i} = -\frac{\partial q_i}{\partial x_i} + \frac{\partial \tau_{ij} u_i}{\partial x_j} \tag{2.25}$$

where $q_i$ is the energy flux:

$$q_i = -\lambda \frac{\partial T}{\partial x_i} + \rho \sum_{k=1}^{N} h_k Y_k V_{k,i} \tag{2.26}$$

Total energy can be written as the summation of sensible ($e_s$), chemical ($\sum_{k=1}^{N} \Delta h_{f,k}^0 Y_k$) and kinetic ($\frac{1}{2} u_i u_i$) energies:

$$e_t = e_s + \frac{1}{2} u_i u_i + \sum_{k=1}^{N} \Delta h_{f,k}^0 Y_k \tag{2.27}$$

From the first law of thermodynamics, sensible energy can be written in terms of sensible enthalpy, $h_s$:

$$e_s = h_s + \frac{P}{\rho} \tag{2.28}$$

After some manipulations, energy equation can be written in terms of sensible enthalpy as:

$$\frac{\partial \rho h_s}{\partial t} + \frac{\partial \rho u_i h_s}{\partial x_i} = \frac{\partial P}{\partial t} + \frac{\partial u_i P}{\partial x_i} + \frac{\partial}{\partial x_i}\left(\lambda \frac{\partial T}{\partial x_i}\right) - \frac{\partial}{\partial x_i}\left(\rho \sum_{k=1}^{N} h_{s,k} Y_k V_{k,i}\right) + \dot{\omega}_T \tag{2.29}$$

where $\dot{\omega}_T = -\sum_{k=1}^{N} \Delta h_{f,k}^0 \dot{\omega}_k$ is the heat release rate.

## 2.4 Combustion Modeling

### 2.4.1 Chemical Kinetics

For combustion applications, a global reaction of any hydrocarbon with oxygen is expressed as:

$$C_n H_m O_p + \left(n + \frac{m}{2} - \frac{p}{2}\right) O_2 \longrightarrow n CO_2 + \frac{m}{2} H_2 O \tag{2.30}$$

This global reaction is actually composed of many elementary reactions, $N_{reac}$ and a large number of intermediate species, $N$. This chemical mechanism can be represented as:

$$\sum_{k=1}^{N} \nu_{kj}^{'} M_k \rightleftharpoons \sum_{k=1}^{N} \nu_{kj}^{''} M_k \qquad \text{for} \qquad j = 1, ..., N_{reac} \tag{2.31}$$

where $M_k$ is the symbol for species $k$, $\nu_{kj}^{'}$ and $\nu_{kj}^{''}$ are the molar stoichiometric coefficients of species $k$ in reaction $j$. In order to conserve mass:

$$\sum_{k=1}^{N} \nu_{kj}^{'} W_k = \sum_{k=1}^{N} \nu_{kj}^{''} W_k, \qquad \text{or} \qquad \sum_{k=1}^{N} \nu_{kj} W_k = 0 \tag{2.32}$$

where $\nu_{kj} = \nu_{kj}^{''} - \nu_{kj}^{'}$.

For species $k$, the mass reaction rate, $\dot{\omega}_k$ is the sum of rates $\dot{\omega}_{kj}$ of reactions in which species $j$ is involved:

$$\dot{\omega}_k = \sum_{j=1}^{N_{reac}} \dot{\omega}_{kj} = W_k \sum_{j=1}^{N_{reac}} \nu_{kj} Q_j, \qquad \text{with} \qquad \frac{\dot{\omega}_{kj}}{W_k \nu_{kj}} = Q_j \tag{2.33}$$

where $Q_j$ is the progress rate of reaction $j$:

$$Q_j = k_{fj} \prod_{k=1}^{N} [X_k]^{n_{kj}^{'}} - k_{rj} \prod_{k=1}^{N} [X_k]^{n_{kj}^{''}} \tag{2.34}$$

where $n_{kj}^{'}$ and $n_{kj}^{''}$ are the forward and reverse orders of species $k$ for the reaction $j$, and $k_{fj}$ and $k_{rj}$ are the forward and reverse rates of reaction $j$.

The Arrhenius law is used to model the reaction rate:

$$k_{fj} = A_{fj} T^{\beta j} exp\left(-\frac{T_{aj}}{T}\right) \tag{2.35}$$

where $A_{fj}$ is the pre-exponential constant, $\beta j$ is the temperature exponent, and $T_{aj}$ is the activation temperature (or equivalently the activation energy $E_j = RT_{aj}$).

The equilibrium constant, $K_{eq,j}$ makes a link between the forward and the reverse reaction rate for reversible reactions:

$$k_{br} = \frac{k_{fr}}{K_{eq,j}}, \text{with} \quad K_{eq,j} = \left(\frac{P^0}{RT}\right)^{\sum_{j=1}^{N_{reac}} \nu_{kj}^{''} - \nu_{kj}^{'}} exp\left(\frac{\Delta S_j^0}{R} - \frac{\Delta H_j^0}{RT}\right) \tag{2.36}$$

where $\Delta S_j^0$ and $\Delta H_j^0$ are entropy and enthalpy variations during the reaction $j$, respectively, and $P_0$ is the reference pressure at which $\Delta S_j^0$ and $\Delta H_j^0$ are defined.

### 2.4.2 Combustion Regimes

Combustion applications are mainly divided into two categories depending on the fuel and oxidant mixing before the ignition, as diffusion flames and premixed flames. Structures of diffusion and premixed flames are given in Figure 2.1.

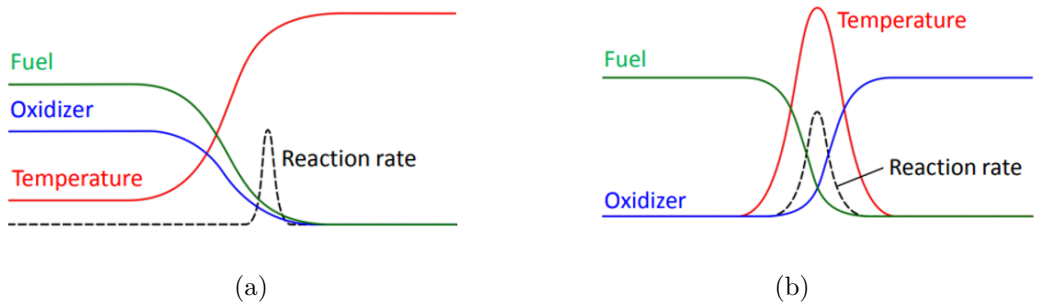


Figure 2.1: (a) Premixed and (b) diffusion flame structures.

In diffusion flames, oxidizer and fuel are not mixed before the combustion process, and the reaction proceeds as the molecules of the reactants diffuse towards the reaction zone.

In premixed flames, however, fuel and oxidizer are mixed before ignition. Unburnt and burnt gases are separated from each other with a reaction zone where the change in reaction rate is observed, reported in Figure 2.2.

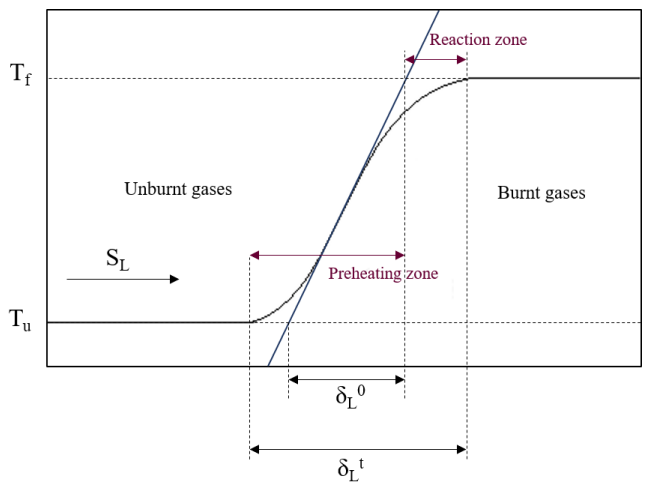


Figure 2.2: Flame thickness definitions for premixed flames [78].

The mass fractions of fuel and oxidizer at stoichiometric conditions at which both fuel and oxidizer are completely consumed relying on the global reaction is described as the mass stoichiometric ratio, $s$:

$$\left(\frac{Y_O}{Y_F}\right)_{st} = \frac{\nu_O^{'} W_O}{\nu_F^{'} W_F} = s \tag{2.37}$$

The equivalence ratio of mixture, $\phi$ can then be computed as:

$$\phi = s\frac{Y_F}{Y_O} = \left(\frac{Y_F}{Y_O}\right) / \left(\frac{Y_F}{Y_O}\right)_{st} \tag{2.38}$$

A sharp temperature gradient is observed for premixed flames where the unburnt gases are heated in preheating zone before burning. From this temperature profile, the thermal flame thickness can be computed as $\delta_L^0$:

$$\delta_L^0 = \frac{T_{burnt} - T_{unburnt}}{\left|\frac{\partial T}{\partial x}\right|_{max}} \tag{2.39}$$

Total flame thickness, represented as $\delta_L^t$ in Figure 2.2, can also be defined as the distance where the entire change in temperature is observed. Since thermal flame thickness directly measures the temperature gradient, it is more accurate to use it for physical definitions and comparisons.

Finally, flame speed, $S_L$ can also be defined as:

$$S_L = -\frac{1}{\rho(Y_{F,unburnt} - Y_{F,burnt})} \int_{-\infty}^{\infty} \dot{\omega}_k dx \tag{2.40}$$

## 2.5 Two-Phase Flow Modelling

A numerical simulation for two-phase flows should be able to capture the detailed flow field, species, and temperature distributions that are challenging to measure even with sophisticated experimental methods. These extensive numerical models use jump relations at the interface to couple the solutions to the governing equations for flow, species, and energy in the liquid and gas phases. The transport equations can be solved using numerical methods, such as the Volume of Fluid (VOF) and Level Set methods that consider the exchanges of

mass, momentum, species, and energy between the phases [85, 72]. These methods require high computational costs because they need a high enough spatial resolution to capture interface position. In order to overcome this demand, Eulerian-Lagrangian methods are developed, in which the gas phase is solved by using the Eulerian approach, while the dispersed phase is solved by flow models. Then, two solutions are coupled by introducing source terms to mass, momentum, and energy conservation equations [95].

### 2.5.1 Eulerian-Lagrangian Approach

In the Eulerian-Lagrangian approach, the liquid phase is defined as the Lagrangian particles where they are assumed to be spheres. The mass of the droplet can directly be computed from:

$$m_p = \rho_p \frac{\pi}{6} d_p^3 \tag{2.41}$$

where $m_p$, $\rho_p$ and $d_p$ are the mass, density and diameter of the particle. The properties of particles i.e., position, $\mathbf{x}_p$ and velocity, $\mathbf{u}_p$ are calculated at the corresponding spatial location:

$$\frac{d\mathbf{x}_p}{dt} = \mathbf{u}_p \tag{2.42}$$

$$\frac{dm_p\mathbf{u}_p}{dt} = \mathbf{F}_p^{ext} \tag{2.43}$$

where $\mathbf{F}_p^{ext}$ is the external forces acting on the particle, mainly gravitational forces, $\mathbf{F}_G$ and aerodynamic forces, $\mathbf{F}_A$. Gravitational forces, $\mathbf{F}_G$ can be defined as:

$$\mathbf{F}_G = (\rho_p - \rho)\frac{\pi}{6} d_p^3 \mathbf{g} \tag{2.44}$$

where $\rho$ is the carries phase density and $\mathbf{g}$ is the gravitational acceleration.

Aerodynamic forces are mainly the drag force and pressure force. Under a constant pressure environment, only the drag force is considered:

$$\mathbf{F}_A = m_p \frac{1}{\tau_p}(\mathbf{u}_p - \mathbf{u}_\infty) \tag{2.45}$$

where $\mathbf{u}_\infty$ is the velocity of the carrier gas and $\tau_p$ is the relaxation time:

$$\tau_p = \frac{4}{3C_D Re_p} \frac{\rho_p}{\rho} \frac{d_p^2}{\nu} \tag{2.46}$$

where $\nu$ is the kinematic viscosity of the carrier gas and $Re_p$ is the particle Reynolds number, is also defined as:

$$Re_p = \frac{d_p |\mathbf{u}_p - \mathbf{u}_\infty|}{\nu} \tag{2.47}$$

Drag coefficient, $C_D$ can be computed from Shiller and Nauman emprical correlation [67] for $Re_p < 1000$:

$$C_D = 24(1 + 0.15 Re_p^{0.687}) \tag{2.48}$$

The coupling between the gaseous and liquid phase is achieved via two-way coupling in which the influence of the particles on the gaseous phase is introduced via mass, $\Theta_M$, momentum,$\Theta_D$ and energy, $\Theta_H$ source terms into the Eulerian conservation equations.

$$\Theta_M(\mathbf{x}, t) = \frac{1}{\Delta V} \int_{\Delta V} \sum_{n=1}^{N_p} -\dot{m}_p^{(n)} \delta \left( \mathbf{x} - \mathbf{x}_p^{(n)}(t) \right) dV \tag{2.49}$$

$$\Theta_D(\mathbf{x}, t) = \frac{1}{\Delta V} \int_{\Delta V} \sum_{n=1}^{N_p} -\mathbf{F}_p^{(n)} \delta \left( \mathbf{x} - \mathbf{x}_p^{(n)}(t) \right) dV \tag{2.50}$$

$$\Theta_H(\mathbf{x}, t) = \frac{1}{\Delta V} \int_{\Delta V} \sum_{n=1}^{N_p} \left( m_p^{(n)} C_{p,l} \frac{dT_p^{(n)}}{dt} + \dot{m}_p^{(n)} L_v \right) \delta \left( \mathbf{x} - \mathbf{x}_p^{(n)}(t) \right) dV \tag{2.51}$$

where $\Delta V$ is the control volume of mesh cell containing the droplet $n$.

### 2.5.2 Evaporation of an Isolated Droplet

For the evaporation of a droplet, temperature and concentration gradients between liquid and gaseous phases control the heat and mass transfer processes. First, the droplet is heated by the heat transfer from the gaseous phase via conduction, resulted in an increase in the internal energy of the droplet's molecules. Hence, the molecules detach from the droplet, and the vapor concentration around the droplet surface increases. Due to high concentration gradient, the mass transfer occurs from the surface of the droplet towards the gaseous phase. Consequently, the rate of evaporation is defined as the rate of diffusion of the liquid from the droplet's surface to the surrounding gas. The simplest model for evaporation is proposed by Spalding [103]. After that, Abramzon and Sirignano extended the evaporation model by introducing the effects of convective flow around the droplet [1]. Recent evaporation models are summarized by Sazhin including the unresolved issues such as non-spherical droplets, the effect of moving interface, etc. [99].

In this part, the evaporation model of Spalding [103], and the extensions proposed by Abramzon and Sirignano [1] are introduced.

#### 2.5.2.1 Spalding Model

In the Spalding model, the main assumptions can be listed as [103]:

- The droplet is perfectly spherical and isolated from other droplets.
- Thermal conductivity of the droplet is infinite, and the temperature of the droplet, $T_p$ is constant.
- Thermodynamic equilibrium is valid for the surface of the droplet with the surrounding gas. Therefore, the partial saturated vapor pressure at the surface of the droplet can be calculated from the Clasius-Clapeyron relation:

$$P_s = P_{ref} \exp\left[\frac{W\,L_v}{R}\left(\frac{1}{T_{evap}} - \frac{1}{T_p}\right)\right] \tag{2.52}$$

where $W$ is the molar mass and $L_v$ is the latent heat of vaporization. $T_{evap}$ is the evaporation temperature of the droplet at the reference pressure, $P_{ref}$=1 atm.

- Thermal diffusivity of the droplet, $\mathcal{D}$ is lower than the thermal diffusivity of the gaseous phase. Therefore, the thermal response is quasi-stationary in the gas.

- The properties of the surrounding gas are constant from the droplet surface to the far field. These properties are calculated from 1/3 law proposed by Hubbard [42]:

$$T_{1/3} = \frac{2}{3}T_s + \frac{1}{3}T_\infty \tag{2.53}$$

$$Y_{1/3} = \frac{2}{3}Y_s + \frac{1}{3}Y_\infty \tag{2.54}$$

- The liquid phase is an ideal mixture, and no chemical reaction takes place.

- The solubility of the ambient gas in the liquid is negligible.

- The effects of gravity and radiation are negligible.

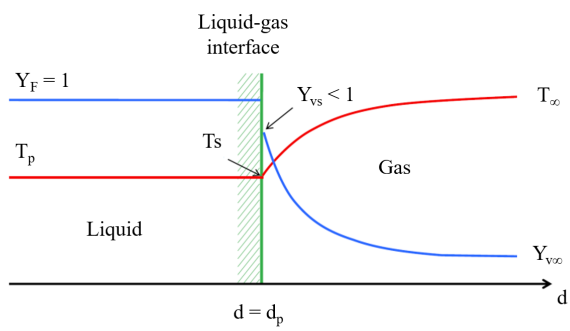


Figure 2.3: Temperature and mass fraction profiles from liquid through gas phase.

Droplet mass temporal evolution is determined assuming the fuel mass flux leaving the droplet surface equal to the variation of mass of the droplet:

$$\frac{dm_p}{dt} = \dot{m}_p = -\pi\, d_p\, Sh\, \rho_p\, \mathcal{D}\, ln(1 + B_M) \tag{2.55}$$

where $Sh$ is the Sherwood number, $\rho_p$ is the density of the particle, $\mathcal{D}$ is the diffusion coefficient and $B_M$ is Spalding mass number characterizing the effects of mass transfer defined as:

$$B_M = \frac{Y_s + Y_\infty}{1 - Y_s} \tag{2.56}$$

where $Y_s$ is the evaporated mass fraction of the droplet at the surface and $Y_\infty$ is the evaporated mass fraction at the far field.

Using the relation of mass variation, the change in droplet diameter is expressed as:

$$d_p^2 = d_{p,0}^2 - \frac{8\rho\mathcal{D}}{\rho_p} ln(1 + B_M)t = d_{p,0}^2 - Kt \tag{2.57}$$

where $d_{p,0}$ is the initial diameter of the droplet and $t$ is the time. Equation 2.57 is also known as d$^2$-law at which the evaporation rate, $K$ can directly be obtained.

The temporal evolution of the droplet temperature is estimated by integrating the energy conservation equation from the surface of the droplet to the far field:

$$\frac{dT_p}{dt} = \frac{\dot{m}_p}{m_p C_p} \left[ \frac{C_{p,ref}}{B_T} (T_s - T_\infty) + L_v \right] \tag{2.58}$$

where $C_p$ is the specific heat of the droplet and $B_T$ is the Spalding heat number defined as:

$$B_T = (1 - B_M)^{\frac{Sh\,Pr}{Nu\,Sc}} - 1 \tag{2.59}$$

where $Pr$ is the Prandtl number, $Sc$ is the Schmidt number. $Sh$ and $Nu$ are the Sherwood and Nusselt numbers, respectively and they are computed using the Ranz-Marshall correlation [80]:

$$Sh = 2 + 0.6{Re_p}^{1/2} Sc^{1/3} \tag{2.60}$$

$$Nu = 2 + 0.6{Re_p}^{1/2} Pr^{1/3} \tag{2.61}$$

#### 2.5.2.2 Abramzon-Sirignano Model

The convective flow around the droplet creates a boundary layer and increases the mass and heat transfer, hence, the evaporation rate. In order to introduce the effects of the convection and development of a laminar boundary layer around the droplet, Abramzon and Sirignano proposed a correction function, $F$ for $Sh$ and $Nu$ numbers as [1]:

$$F_{M/T} = 1 + {B_{M/T}}^{0.7} \frac{\ln(1 + B_{M/T})}{B_{M/T}} \tag{2.62}$$

$$Sh^* = 2 + \frac{Sh - 2}{F_M} \tag{2.63}$$

$$Nu^* = 2 + \frac{Nu - 2}{F_T} \tag{2.64}$$

### 2.5.3 YALES2 Solver

Computations are performed with the YALES2 solver developed in CNRS CORIA [63]. Direct Numerical Simulation (DNS) and Large Eddy Simulation (LES) of reacting two-phase flows in complex geometries can be solved by the unstructured low-Mach number code, YALES2. Detailed explanations of numerical schemes and the solver can be found in related studies [47, 21].

In this study, variable density solver (VDS) is used to simulate the gaseous phase, while the Spalding and Abramzon-Sirignano models are used to compute the droplet evaporation. Eulerian-Lagrangian coupling is performed with the addition of source terms. For flame simulations, the San Diego mechanism is used to simulate multi-component gaseous phase [115].

# CHAPTER 3

# EXPERIMENTAL METHODS

In this chapter, experimental methods and optical diagnostics are introduced. In the first part, a spherical combustion chamber is described, and experiments performed under microgravity conditions to observe the effects of droplets on flame instabilities are defined. In the second part, stagnation burner experiments to track the evaporation of an isolated droplet through a flame field and morphological changes in flame front due to the passage of the droplet are reported. Several laser and optical diagnostics are used, and the post-treatment methods are performed in order to extract physical information.

## 3.1 Microgravity Experiments: Spherically Expanding Aerosol Flame

### 3.1.1 Parabolic Flights

Microgravity enables a deep understanding of physical and chemical systems by neglecting the effect of various natural physical phenomena. There are many fields of study where microgravity is used via several platforms. In the case of droplet-flame interactions, microgravity ensures the immobility of the droplets inside the combustion chamber since, under Earth's gravity, droplets tend to fall as other massive objects. This causes sedimentation and coalescence of droplets making impossible to observe the effects of the presence of individual droplets on the flame propagation.

Different platforms exist to have zero-g environments such as drop towers (i.e., NASA Glenn 2.2 Second Drop Tower, ZARM drop tower at Bremen), aircraft

(i.e., Japanese LearJet MU-300 aircraft), sounding rockets and orbital stations (International Space Station). The features, such as duration, flexibility, cost, quality, and frequency, change among these platforms. Since the parabolic flights on board an aircraft offer a good compromise between the duration of microgravity and enough quality of reduced g, experiments are conducted during parabolic flights, given in Figure 3.1.

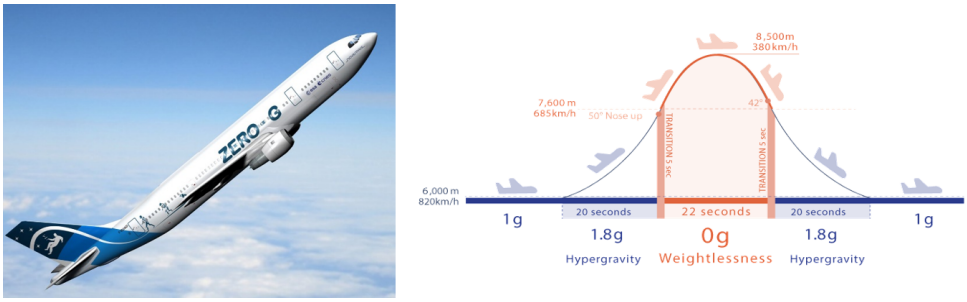


Figure 3.1: Airbus A310 ZERO-G airplane and durations of different gravity levels during the parabolic flights.

The basic idea behind the parabolic flight is to put the aircraft on an elliptical trajectory as it falls. When an aircraft only sees the top of a trajectory, a parabola can be used to approximate that trajectory. The injection speed and sine of the injection angle with respect to the horizontal axis determine how long free fall lasts during a parabola (in this case, 22 seconds). The phrase injection describes the shift to microgravity, that is, the start of the parabola. Therefore, it is imperative to maximize these two quantities to lengthen the period spent in microgravity. In Figure 3.2, acceleration measurements and change in gravity are reported for one parabola. First, the aircraft flies horizontally at nearly maximum speed (up to 10:27:00). Then, the aircraft is gradually pitched up to an angle between 45-50° where the aircraft load reaches to 1.8 g (between 10:27:00 and 10:27:30). Then when the pitch angle reaches to 50°, the thrust of the engines is reduced at the level required to exactly compensate for the drag of the aircraft. In parallel, the aircraft is placed at the zero lift angle. This cancels all forces other than gravity which is referred to as the injection phase. When the transition from 1.8 g to 0 g is completed, the aircraft is maintained at microgravity for nearly 22 seconds by constantly adjusting the trim to remain

at the lift angle. During this period, the plane has a parabolic trajectory (up to nearly 10:27:45). When the aircraft reaches a negative bank angle of 45°, the aircraft exits the parabola phase until reaching a level trajectory while the load is 1.8 g (up to nearly 10:28:15).

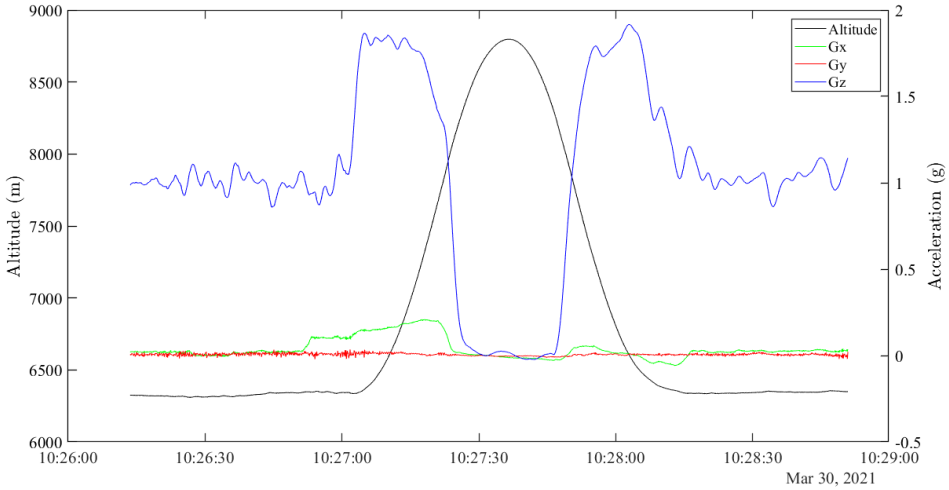


Figure 3.2: Measurement of accelerations on board A310 ZERO-G (VP158, flight 1, parabola 6) – Novespace data.

In the scope of this study, experiments are conducted during the parabolic flights of Centre National d'Etudes Spatiales (CNES) Airbus A310 ZERO-G, given in Figure 3.1. Twenty-two seconds of weightlessness under $10^{-2}$ g are achieved. One flight campaign is carried out with three flights of 31 parabolas.

### 3.1.2 Aerosol Setup

Aerosol setup is used to investigate the onset of instabilities occurring in a spherically expanding flame due to the presence of fuel droplets. The aerosol setup has been previously used in the scope of three theses, and more detailed explanations can also be found in these studies [66, 109, 82]. Strong experimental, safety and operational constraints are imposed to be able to perform high-temperature and high-pressure experiments during a parabolic flight. The complete device should also be portable and prepared for failure scenarios. A photograph of the experimental setup is shown in Figure 3.3. It mainly consists of a combustion

chamber, gas cylinders, light source, high-speed camera, automation/control system, and supplementary flow devices, i.e., liquid feeding pumps and flow controllers, shown in Figure 3.4.

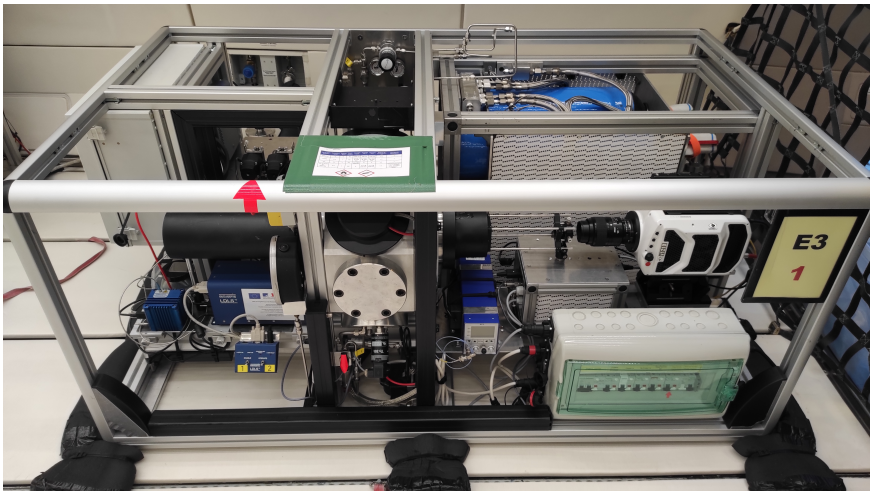


Figure 3.3: Photograph of the experimental device in flight configuration on board A310 ZERO-G with Schlieren configuration.

Due to the time limitation of the preparation phase before zero-g and the experimental stage at zero-g, the system needs to be fully controlled, which is achieved by Siemens ET 200S PLC. During the filling and releasing of the chambers, PID controllers are used. Two types of K thermocouples are used by the temperature controllers of the evaporator and inner chamber heater. A fast AVL pressure sensor is placed into the wall of the inner chamber in order to measure the pressure during both expansion and combustion. A Bourdon-type mechanical pressure sensor is connected to the outer chamber to obtain a visual value of the pressure in the chamber.

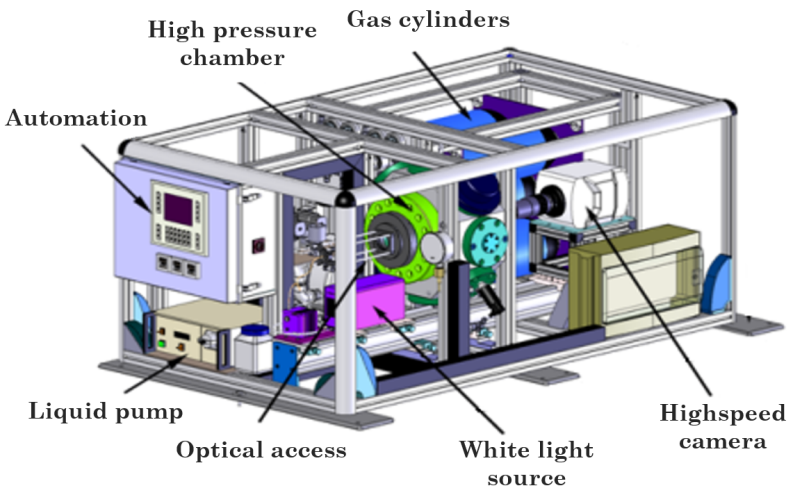


Figure 3.4: Experimental setup with Schlieren configuration.

#### 3.1.2.1 Combustion Chamber

The experimental setup consists of a double confinement chamber; an inner spherical combustion chamber of 1 L stainless steel tank (IHP: Insert Haute Pression), and an outer chamber of 11 L aluminum alloy (CHP: Chambre Haute Pression). Combustion occurs in IHP while CHP is filled with nitrogen ($N_2$). Two chambers are connected by 8 valves whose drains are arranged symmetrically on the IHP. Initially, the valves are kept closed and sealed by springs. In case the pressure difference between IHP and CHP becomes greater than 0.025 MPa, the valves open. Once the mixture inside the combustion is ignited and the flame spreads, the differential pressure between IHP and CHP increases; hence, the valves open, and the flammable gas is evacuated to CHP while mixing with $N_2$ to ensure non-flammability. The high volume of CHP enables to reduce the pressure rise in the combustion chamber.

#### 3.1.2.2 Fuel Injection and Chamber Filling

Combustion chamber, IHP is filled with air as an oxidizer while the outer chamber, CHP is filled with $N_2$. Flow rates are controlled from the automation via two mass flow meters of Brooks Instrument maximum flow rate 100 L/min and

10 L/min for $N_2$ and air, respectively. In order to minimize the pressure difference between chambers, two PID controllers are used. First, the pressure of IHP is set to the final pressure, and then, the controller of CHP is arranged so that the pressure difference between the two chambers, calculated dynamically, becomes zero. The gas flow path is given in the diagram in Figure 3.5.

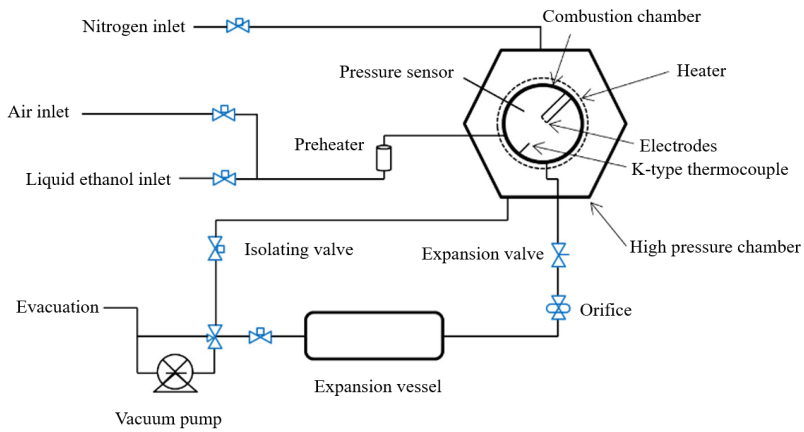


Figure 3.5: Gas flowpath diagram of the experimental setup.

Fuel injection to IHP is achieved via Gilson liquid pump. An 8-port/2-way Velco switching valve is used to transfer the liquid from a reservoir to IHP filling. This valve is equipped with two sampling loops of volume, $V_{sampling} = 20$ $\mu L$. The sampling loops are initially connected to air and fuel reservoirs. When the ethanol is desired to be pumped, both sampling loops are connected to the air reservoir, pushing the liquid to the combustion chamber. Each rotation of the valve induces the injection of a well-defined volume of liquid. However, the dead volume, $V_{dead} = 8.5$ $\mu L$, should be considered. The quantity of the fuel is determined from:

$$n_{fuel} = \frac{N_v(V_{sampling} + V_{dead})\rho_{fuel}}{W_{fuel}} \tag{3.1}$$

with $N_v$ is the number of valve switch, $\rho_{fuel}$ and $W_{fuel}$ are density and molecular weight of fuel, respectively. Liquid fuel is fed to the system at the gaseous phase by passing through a heater before the combustion chamber.

The amount of air inside the chamber is then calculated as follows:

$$n_{air} = n_{total} - n_{fuel} = \frac{P_{init}V_{IHP}}{RT_{init}} - n_{fuel} \tag{3.2}$$

with $V_{IHP}$ is the volume of the inner chamber. Accordingly, equivalence ratio is computed from Equation 2.38.

#### 3.1.2.3 Aerosol Creation

The fuel aerosol is created via Wilson cloud chamber principle [124]. At the beginning of each experiment, the inner chamber, IHP is vacuumed and then filled with dry air and evaporated fuel at the desired equivalence ratio and initial pressure. It is also connected to a 0.5 L expansion tank initially evacuated by opening a valve. Once the mixture is fed to this expansion tank from the combustion chamber, pressure drops inside IHP, leading to a decrease in temperature and lowering to the saturation vapor pressure of fuel by Clausius Clapeyron's law. When the partial pressure of fuel is higher than the saturation vapor pressure, condensation happens, and the liquid phase of fuel is formed. The distance between droplets, number of droplets, and droplet size are controlled by thermodynamic parameters such as initial pressure, $P_i = P_{ignition} + \Delta P$, equivalence ratio, $\phi$, pressure drop, $\Delta P$ and the rate of pressure drop. The rate of pressure drop can be adjusted via the size of an orifice placed between the IHP and the expansion tank. This rapid expansion condensation method enables to produce homogeneous and monodisperse aerosols. More details can be found in other studies on nucleation phenomenon in aerosol [66, 109, 82].

#### 3.1.2.4 Ignition

Aerosol creation is achieved under microgravity conditions to eliminate droplet settling and coalescence. A delay of a few hundred milliseconds is imposed between the end of the expansion and the triggering of the ignition procedure for aerosol stabilization. Then, the heterogeneous mixture is ignited via two 0.35 mm tungsten electrodes at the center of IHP. The deposited energy is minimized while the presence of an electric arc between electrodes is ensured for a lower disturbance on the flame.

### 3.1.3 Experimental Procedure

The experiments are performed under zero-g conditions during the parabolic flights of Airbus A310 ZERO-G. At each parabola during those flights, there are 2 minutes of vacuum to prepare the setup and almost 1 minute to start and complete the one set of experiment. Accordingly, the given procedure is followed for each set of the experiment:

1. The chamber is evacuated to flush the combustion products formed from the previous set of experiments.
2. Simultaneous filling is achieved for IHP and CHP with a combustible mixture (dry air + gaseous fuel) an $N_2$, respectively. The gaseous and homogeneous mixture is preserved at the gaseous phase until the period of microgravity.
3. Pressure drop is achieved to create aerosol under zero-g. The heterogeneous mixture rests for a few hundred milliseconds for stabilization.
4. Ignition is performed, and flame front expansion is tracked.

### 3.1.4 Experimental Configuration and Conditions

Since the experiments are performed under microgravity for a limited time, certain constraints must be considered. First, the equivalence must be decided accordingly such that the liquid pump can fill the system with fuel in time. Secondly, the richness of the mixture must be within the flammability limits due to safety regulations. A high amount of fuel can also lead to fuel condensation inside IHP.

Experimental configuration is presented in Figure 3.4. The combustion chamber is coupled with a laser-driven white light source, Energetiq LDLS 170 nm-2100 nm, and a high-speed camera, Phantom v1210 equipped with Nikon AF Micro-NIKKOR 105 mm lens. For imaging, 10,000 frames/s rates is used. Schlieren technique is used to visualize the flame morphology for microgravity experiments. The two pairs of aligned transparent windows achieve optical access to

the chamber. Two spherical lenses are replaced on the back and the front of the chamber so that the light will penetrate as a sheet. In order to track the cellular structure, the distance between the lenses is adjusted so that the darkness will be at the minimum level. Before the high-speed camera, a pinhole with a diameter of 0.7 mm is placed to focus the light.

Experiments are performed with ethanol, $C_2H_5OH$ as a fuel and dry air (80% $N_2$, 20% $O_2$) as an oxidizer at the conditions presented in Table 3.1. These conditions have been repeated in the previous studies, Renoux et al. [82, 83], and the characterization of the liquid phase has been done via several optical diagnostics. Therefore, the same droplet properties are assumed to be valid for this study.

Table 3.1: Experimental conditions performed in aerosol chamber (AC) for $C_2H_5OH$/air spherically-expanding aerosol flames.

| Condition | $P_{ignition}$ (MPa) | $\phi$ | $\Delta P$ (MPa) | $T_{ignition}$ (K) | $a_{mean}$ (mm) | $SMD$ ($\mu$m) | $Le_{eff}$ |
|---|---|---|---|---|---|---|---|
| AC-1 | 0.25 | 1.2 | 0.15 | 337 | 0.527±0.05 | 9.8±0.9 | 1.12 |
| AC-2 | 0.33 | 1.3 | 0.12 | 341 | 0.596±0.05 | 8.3±0.9 | 1.10 |
| AC-3 | 0.33 | 1.4 | 0.12 | 341 | 0.538±0.05 | 8.7±0.9 | 1.04 |
| AC-4 | 0.30 | 1.1 | 0.20 | 339 | 0.497±0.05 | 9.9±0.9 | 1.19 |
| AC-5 | 0.30 | 1.2 | 0.20 | 339 | 0.502±0.05 | 9.9±0.9 | 1.08 |
| AC-6 | 0.35 | 1.0 | 0.25 | 335 | 0.468±0.05 | 9.6±0.9 | 1.31 |

## 3.2 Ground Experiments: Stagnation Flame

### 3.2.1 Stagnation Burner

The purpose of the stagnation burner is to track the droplet evaporation sequence through a stationary premixed laminar flame and the changes in the morphology of flame due to the passage of droplets. The stagnation burner has been previously used in the scope of three theses for different purposes [10, 4, 82].

The schematic of the stagnation burner is given in Figure 3.6. A $N_2$ co-flow is used to facilitate flame stabilization. A premixed mixture of air and fuel passes through a laminarization grid and then is accelerated by a converging section. The mixture is ignited with an external igniter at the region between the stagnation plate and the burner outlet. With a continuous premixed mixture feeding, a laminar and flat flame is created at the specified conditions, and it is stabilized thanks to the presence of an upper stagnation plate located 25 mm away from the burner outlet.

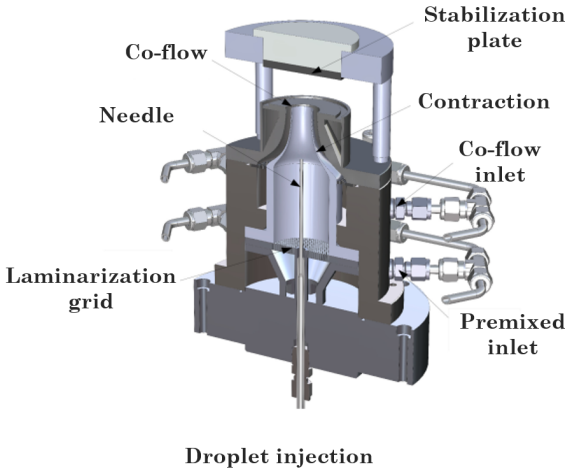


Figure 3.6: Schematic of the stagnation burner.

### 3.2.2 Injector System

Monodispersed liquid droplets with 50 $\mu$m diameter are generated by a piezo-electric injector, Microdrop Technologies MD-K-140. The frequency of the droplet injection is adjusted accordingly to provide enough time between droplet injections and to avoid coagulation and close-distance droplets. The droplets are carried by premixed gas flow in a needle having an internal diameter of 3 mm up to the main flow by drag. The residence time of the droplets in the needle is nearly 500 ms leading to small changes in droplet diameter at the exit of the burner plate. Droplets are then fed to the flame zone perpendicularly from the centerline of the burner. The injection system is reported in Figure 3.7.

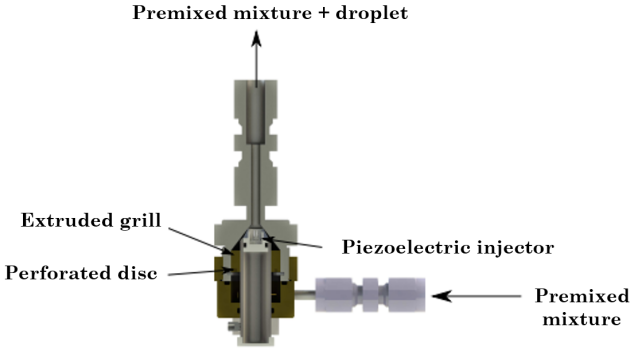


Figure 3.7: Schematic of the injection system.

### 3.2.3 Experimental Configurations and Conditions

#### 3.2.3.1 Studies on Droplet Evaporation

Experimental configuration for droplet evaporation studies is depicted in Figure 3.8. The burner is coupled with a laser device, Coherent Verdi emitting at 532 nm, and a 2D laser sheet is created from a continuous laser beam with the help of one semi-cylindrical divergent lens ($f_2$ = -25 mm) and one plano-convex lens ($f_2$ = 500 mm). Two high-speed cameras, Phantom v1210 and Phantom v1611, equipped with Sigma APO Macro 180 mm lens at the maximum opening, are placed perpendicularly to the flame to observe the scattered light. The first one is dedicated to the velocity measurements of unburnt gases and droplet by Particle Image Velocimetry (PIV) and Particle Tracking Velocimetry (PTV), respectively, while the second one is dedicated to droplet size determination by Interferometric Laser Imaging for Droplet Sizing (ILIDS). The cameras for PIV/PTV and ILIDS have acquisition frequencies of 10,000 and 40,000 frames/s, respectively. In order to have the same time reference, the camera acquisition sequence is triggered by a common trigger signal. They are then synchronized in time to combine different diagnostics. For PIV/PTV camera, 22.9 $\mu$m/pixel resolution is obtained.

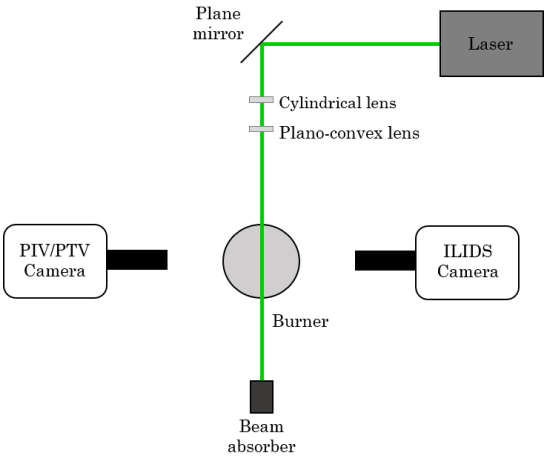


Figure 3.8: Experimental configuration of stagnation burner with PIV/PTV and ILIDS for evaporation studies.

Experiments are performed with an ethanol droplet as the liquid fuel and methane/air premixed flames at reported conditions, given in Table 3.2. For each sequence of experiments, individual droplets are selected over all recordings, and the complete post-processing is performed for each droplet to track its evaporation.

Table 3.2: Experimental conditions performed in stagnation burner (SB) for $CH_4$/air premixed stagnation flames with ethanol droplet for evaporation studies.

| Condition | $\phi$ | $U_0$ (m/s) | $S_L^0$ (m/s) |
|---|---|---|---|
| SBM-1 | 0.8 | 0.560 | 0.279 |
| SBM-2 | 0.9 | 0.743 | 0.336 |
| SBM-3 | 1.0 | 0.824 | 0.364 |
| SBM-4 | 1.1 | 0.699 | 0.357 |

#### 3.2.3.2 Studies on Flame Surface Modifications

Experimental configuration for flame morphology studies is reported in Figure 3.9. Similarly, the burner is coupled with a laser device, and a 2D laser sheet is created. Two high-speed cameras, in addition to an intensifier, are used for visualization. The first camera, Phantom v1210 is equipped with Sigma APO Macro 180 mm lens at the maximum opening to measure the initial droplet size via ILIDS. The second camera, Phantom v1611 equipped with Sigma APO Macro 180 mm lens at the maximum opening, 38 mm extension system, and 1:1 2x magnifier, is coupled with La Vision High-Speed IRO with 90 $\mu$s gate to observe the changes in flame front due to droplet passage via chemiluminescence. The cameras for ILIDS and chemiluminescence have the same frame rate of 10,000 images per second. The camera acquisition sequence is triggered by a common trigger signal to align both cameras and the intensifier in the time frame. 13.7 $\mu$m/px and 27.3 $\mu$m/px resolutions are obtained for chemiluminescence and ILIDS cameras, respectively.

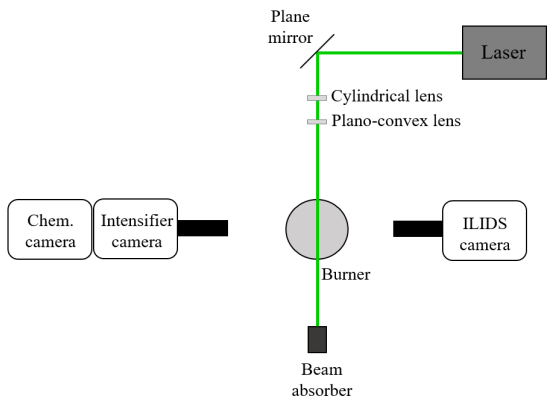


Figure 3.9: Experimental configuration of stagnation burner with chemiluminescence and ILIDS for flame morphology.

Experiments are performed with an ethanol droplet as the liquid fuel and propane/air premixed flames at the conditions, given in Table 3.3. The surface modifications can be captured with a low noise ratio by an intensifier due to propane's high luminosity.

Table 3.3: Experimental conditions performed in stagnation burner (SB) for $C_3H_8$/air premixed stagnation flames with ethanol droplet for flame morphology studies.

| Condition | $\phi$ | $U_0$ (m/s) | $S_L^0$ (m/s) |
|---|---|---|---|
| SBP-1 | 1.0 | 1.101 | 0.415 |
| SBP-2 | 1.1 | 1.115 | 0.412 |
| SBP-3 | 1.2 | 1.100 | 0.373 |
| SBP-4 | 1.3 | 1.095 | 0.297 |
| SBP-5 | 1.4 | 1.109 | 0.200 |

## 3.3 Optical Diagnostics and Post-processing

### 3.3.1 Schlieren Visualization

The Schlieren visualization is based on the idea that light rays are bent whenever the density of fluid changes. The refractive index of the gas, $n$ changes with the density according to the Gladstone-Dale relation;

$$n = K\rho + 1 \tag{3.3}$$

where $K$ is the Gladstone-Dale constant (typically 0.0010-0.0015 $m^3/kg$ for gases) and $\rho$ is the gas density. If the light ray passes orthogonally from the region where the refractive index changes, its phase velocity will change, but it will continue traveling in the same direction. However, when the light ray obliquely crosses the region, it will bend towards the region with greater $n$.

The Schlieren technique is very similar to the shadowgraphy method, which is sensitive to the changes in the second derivative of density, while, in Schlieren, the changes in the first derivative of density are detected. A schematic of a typical Schlieren setup is shown in Figure 3.10. A focusing mirror or lens collimates the light from a source as it travels over a test field with varying refractive index. The parallel light is then refocused by a second lens or mirror, and the light is blocked before collecting from the camera. This blockage is referred to

as a cutoff. A knife edge or pinhole can be used for that purpose.

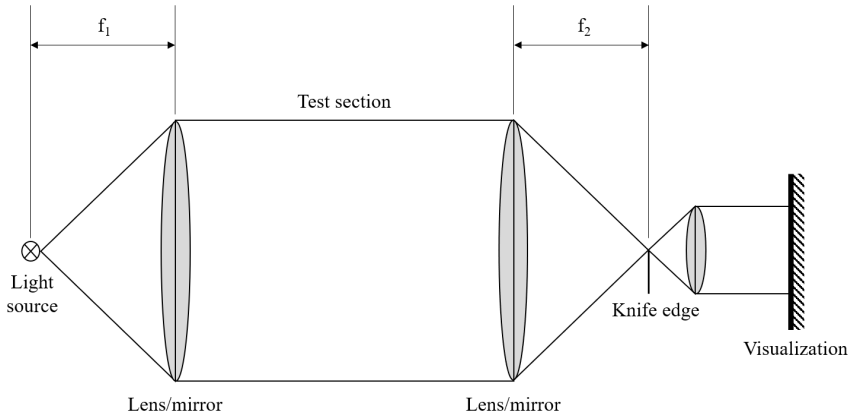


Figure 3.10: Schematic of a Schlieren setup.

For the flow field with a varying density, the lights are deflected. While undeflected light rays are uniformly affected by the cutoff, deflected light rays will be affected depending on the cutoff interaction. Brighter and darker parts will be observed on the image for the cases where the light rays are deflected away from and toward the cutoff, respectively. Hence, in the Schlieren method, the measurement of density change of a field is sensitive to density gradients normal to the cutoff.

In this study, the Schlieren visualization is utilized to capture the instabilities for spherically expanding aerosol flames. During the parabolic flights, the pinhole was too sensitive to the changes in gravitational acceleration, and the opening was moved constantly while $g$ was changing. This situation caused unwanted darkness and resulted in visualization loss at several experimental conditions. Therefore, Schlieren images were only used to obtain qualitative interpretations and understanding of physical phenomena on the formation mechanisms of instabilities for certainty.

### 3.3.2 Chemiluminescence Technique

Chemiluminescence technique is performed by capturing the light emitted from the flame due to the presence of intermediate radicals. For hydrocarbon fuels, the main radical species are $OH^*$, $CH^*$, $C_2{}^*$ and $CO_2{}^*$. These radicals emit photons at a certain frequency while returning their ground state, given in Figure 3.11. As it can be observed, $CO_2{}^*$ emits in the spectral band of 250-700 nm, while for other species, discrete emission lines are observed.

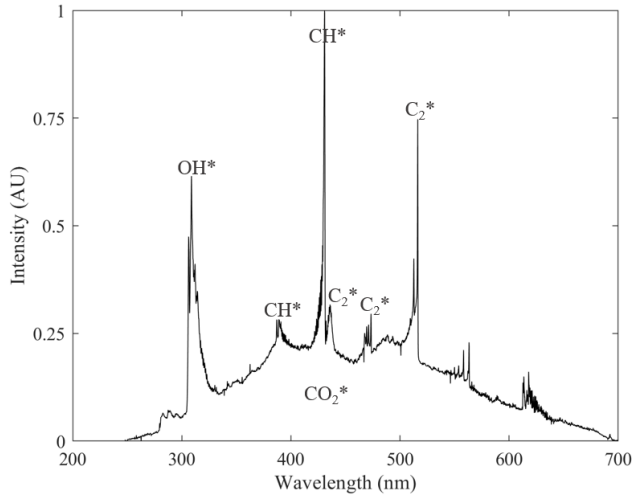


Figure 3.11: Chemiluminescence spectrum of a hydrocarbon flame [4].

In this study, direct measurement of the luminosity, which corresponds to the $CO_2{}^*$ emissions, is performed instead of using special band filters. It is known that with the chemiluminescence measurement, an integral signal along the sight of line is captured, making it hard to observe small changes on the surface. The fuel is selected as propane and the high luminosity of propane can be captured by intensifier with a low noise ratio so that the surface modifications can be observed.

#### 3.3.2.1 Local Extinction Phenomenon

The local extinction phenomenon is investigated from chemiluminescence images by creating a region of interest (ROI) in the droplet passage zone, as seen in Figure 3.12.

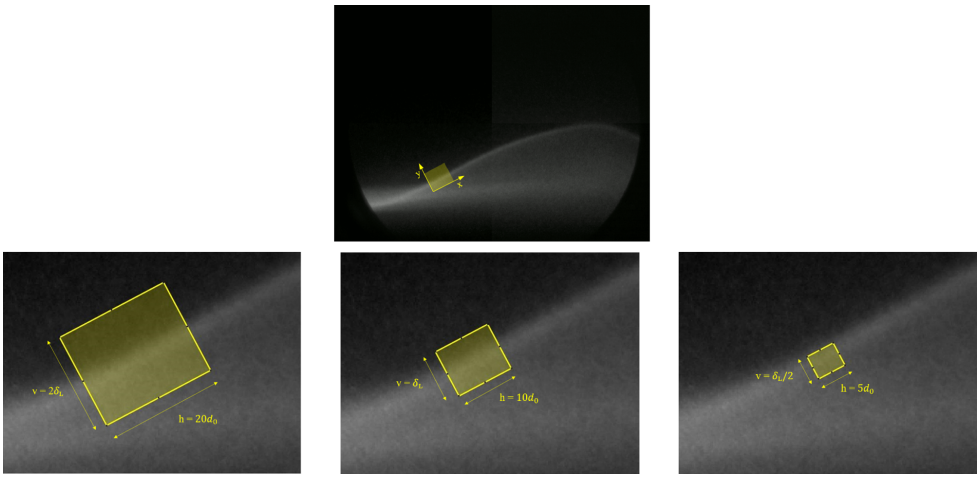


Figure 3.12: Chemiluminescence image of $C_3H_8$/air flame at SBP-4 with the region of interest (yellow) having different sizes depending on the flame thickness and initial droplet size.

The dimensions of ROI are adjusted so that the horizontal distance is 20, 10, and 5 times the initial droplet size, $d_{p,0}$ and the vertical distance is 2, 1, and 0.5 times the flame thickness, $\delta_L$. ROI is also rotated by 28° to capture the signal loss from the perpendicular region to the flame. Two approaches are followed for region selection:

1. The position of the ROI is kept constant at each frame.
2. The position of the ROI is updated at each frame by changing its center according to the flame position. The flame position is updated at each image by calculating the position of the maximum intensity along a perpendicular line to the flame (y-axis), as given in Figure 3.13, due to the fact that the flame is oscillating slightly during the experiments. Then, ROI is moved along the y-axis to align its center with the flame along the x-axis.

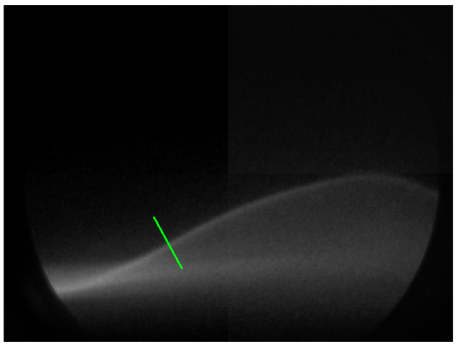

(a)

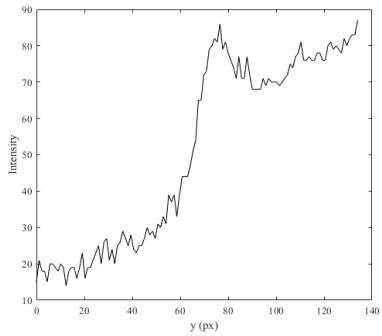


(b)

Figure 3.13: Intensity measurement on the flame to update the ROI according to the flame position (a) Perpendicular line (green) (b) Change in intensity on the line.

After positioning ROI, the signal values are summed for this region at each frame since it is expected to see a decrease in the signal when the droplet passes the flame zone.

#### 3.3.2.2 Wave Propagation

After the droplet passage, a propagating wave is observed on the flame surface via chemiluminescence. The amplitude and wavelength of the propagating wave are measured over time to understand its characteristics. Figure 3.14 shows the detection process of the wave properties.

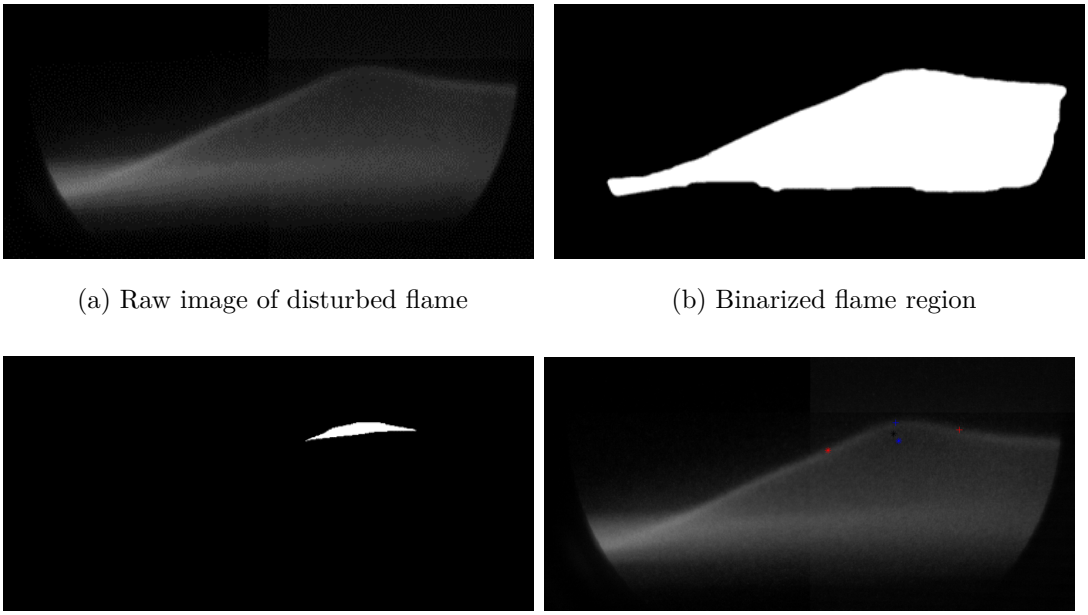

(a) Raw image of disturbed flame

(b) Binarized flame region

(c) Subtraction of undisturbed flame

(d) Disturbance detection

Figure 3.14: Detection of the properties of a propagating wave on the flame surface.

First, the raw image is binarized by applying several thresholds, and the holes are filled via morphological operations to obtain a more accurate selection of the flame region. Gaussian filtering is performed to smooth out the operated region, and after the final binarization, the flame region is masked, as in Figure 3.14b. Then, the undisturbed flame captured in the first image is subtracted from the rest of the images to distinguish the disturbance region on the flame, as in Figure 3.14c. The properties of the region, such as the center of mass and the maximum and minimum lengths, are then computed.

### 3.3.3 Particle Image Velocimetry (PIV)

Particle Image Velocimetry (PIV) is a laser diagnostic method by which the instantaneous 2D velocity field of the cross-sectional slices of 3D flows is measured. This method is based on Mie scattering, which is the elastic scattering of light by particles with a diameter equal to or greater than the incident light's wavelength.

PIV involves passing a laser light pulse through a lens to create a laser sheet. A camera is positioned with its axis of view parallel to the created sheet. The focal point of the lens of the camera is arranged such that the focal plane is at the sheet and the capture area spans the entire field of view. Between two consecutive images, there will be bright pixels caused by particles moving across the laser sheet. After the determination of particle displacement, velocity components in 2D are determined.

In this study, the position of the flame front and the velocity of unburnt gases are determined via PIV. Seeding of the premixed gas is achieved with diethylhexylsebacate (DEHS) droplets having an approximate size of 2-4 $\mu$m in diameter. First, the flame contour is identified using a threshold technique, similar to Chapter 3.3.2.2. The location of the flame front is then determined at $T$=525 K isotherm where DEHS droplets evaporate, given in Figure 3.15a as a green line. The isotherm is resolved from the overlay of 100 images to have more accuracy.

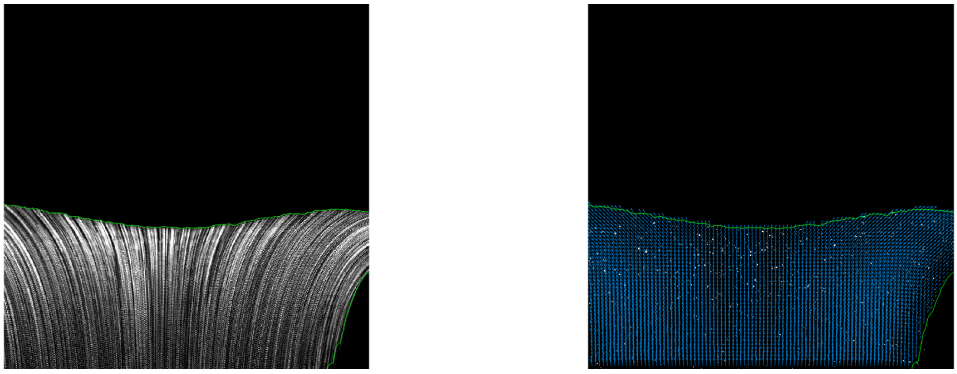

(a) (b)

Figure 3.15: Determination of (a) the flame front and (b) the velocity of unburnt gases based on PIV.

In order to measure the velocity of unburnt gases, an open-source MATLAB library, PIVlab is used [108]. The local displacement of the unburnt gases is determined by comparing two successive images and calculating the displacement of DEHS droplets between two images. The main assumption of this method is that DEHS droplets are small enough to follow the gas flow. Figure 3.15b shows the velocity vectors of unburnt gases.

### 3.3.4 Particle Tracking Velocimetry (PTV)

Particle Tracking Velocimetry (PTV) is a technique also based on Mie scattering to compute the velocity of a particle used when the individual particles can be resolved in two consecutive frames. The displacement of the particles is determined, thus leading to the velocity.

In this study, the motion of the droplet is determined via PTV. The initial position of the droplet is determined from the first image based on the largest connected luminous pixels to initiate the Kanade-Lucas-Tomasi (KLT) algorithm. For each subsequent frame, the location of the droplet is tracked with the KLT feature tracking algorithm in the MATLAB Computer Vision library. Therefore, the droplet's displacement speed in the laboratory reference is calculated. The tracked droplet trajectory is represented in Figure 3.16.

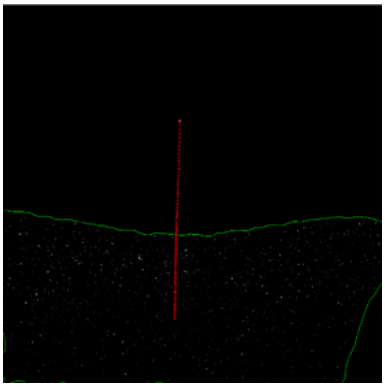

Figure 3.16: Determination of the trajectory of droplet based on PTV ($d_{p,0}$=35 $\mu$m).

### 3.3.5 Interferometric Laser Imaging for Droplet Sizing (ILIDS)

Interferometric Laser Imaging for Droplet Sizing (ILIDS) is a non-invasive optical method in which transparent spherical particles' sizes and spatial distributions can be measured within a defined field of view. ILIDS method is based on interferences between scattered light from a spherical particle that has been coherently illuminated. Two glare points appear in the focus plane at specific scattering angles, depending on the polarization of the incident wave with respect to the observation plane. This is because the reflected and refracted light dominates over the other scattered orders at these angles. The interferences between the reflected and refracted light cause a fringe pattern to appear when the glare points are observed in an out-of-focus plane. The schematic of the ILIDS principle is given in Figure 3.17. Following the geometrical optics approach, an expression can be derived that states that the number of fringes in the far field is directly proportional to the droplet diameter. In order to capture the entire fringe pattern and prevent measurement errors, a sufficient degree of defocus is required.

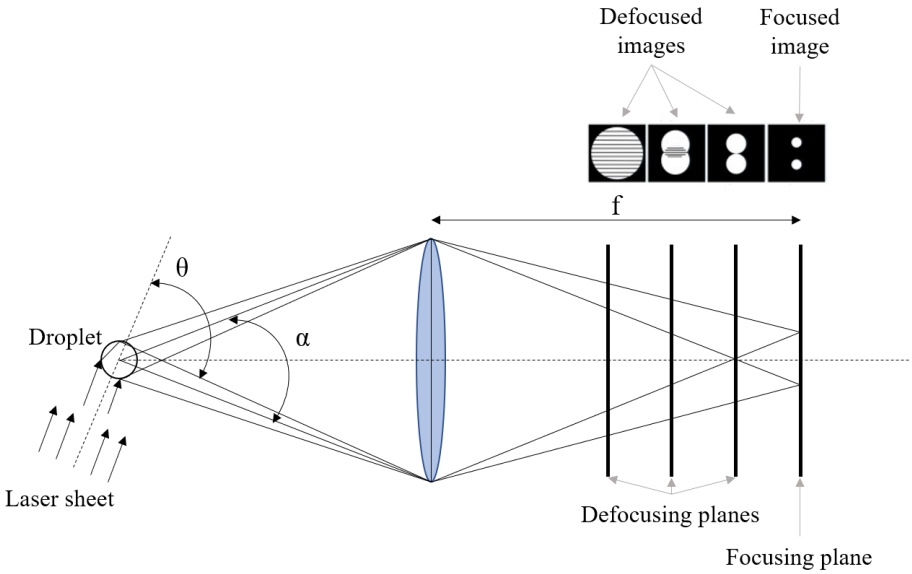


Figure 3.17: The principle of ILIDS.

In this study, ILIDS is coupled with Mie scattering to obtain the droplet size variation during the passage through the flame. The high-speed camera used for ILIDS allows for obtaining a good temporal resolution for the evolution of the droplet size by defocusing and capturing the interference fringe pattern of the droplet at each frame. By providing a high laser power, it is possible to increase the detection of fringes even if the droplet size is very small because the ILIDS method is based on the reflected and the refracted rays visible on the droplet surface. For the evaporation study, 20 Watts laser power is used, which is enough to detect 2-3 fringes at the last image recorded for the ethanol droplet. The number of fringes is computed for an individual droplet at each frame based on the Discrete Fourier Transform (DFT) on the five vertical sections of the fringe pattern. With the help of peak intensities in Fourier space, the fringes are detected and computed. Fringe patterns for a droplet from consecutive frames while passing through the flame is illustrated in Figure 3.18.

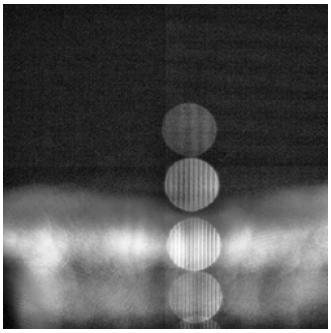

Figure 3.18: Combined sequence of ILIDS images illustrating the evaporation of a droplet while passing through the flame front (droplet diameters from bottom to top; 49 $\mu$m, 49 $\mu$m, 38 $\mu$m and 15 $\mu$m).

The droplet diameter based on the number of fringes is then calculated from the following relation [83]:

$$d_p = N_{fringe}\frac{2\lambda}{\alpha}\left[cos(\theta/2) + \frac{m\,sin(\theta/2)}{\sqrt{m^2 - 2\,m\,cos(\theta/2) + 1}}\right]^{-1} \tag{3.4}$$

where $d_p$ is the particle diameter, $N_{fringe}$ is the number of fringes on the droplet, $\theta$ is the scattering angle (here, 90°), $\lambda$ is the laser wavelength (here, 532 nm), $m$ is the refractive index of the droplet and $\alpha$ is the collecting angle which can be computed from the following relation:

$$\alpha = 2arctan\frac{d_a}{2z_l} \tag{3.5}$$

where $d_a$ is the diameter of the lens and $z_l$ is the distance between the lens and the droplet. In this configuration, 3.52 $\mu$m/fringe resolution is obtained.

# CHAPTER 4

# DROPLET EVAPORATION UNDER FLAME CONDITIONS

This chapter includes experimental and numerical results of the evaporation of an isolated droplet interacting with a stagnation flame field. First, experiments are performed using a stagnation burner with methane/air flames and an ethanol droplet. The motion and diameter change of the droplet are tracked via PTV and ILIDS, respectively, as well as the velocity of unburnt gases via PIV. The numerical part first includes the results of stationary ethanol droplet evaporation surrounded by burnt gases at high temperatures to understand the effect of gas composition on evaporation. The second part of the numerical results covers the injection of an ethanol droplet into the stagnation flame field and evaluation of droplet properties. Lastly, stagnation burner simulations are reported for nonreactive and reactive cases. Simulation results are compared with the experimental data for the evaporation constant of an ethanol droplet at flame conditions.

## 4.1 Introduction

In industrial applications, the fuel stored as liquid, is injected into the combustion chamber via an atomization process in which the liquid jet disintegrates into fragments during a primary break-up and, finally, into droplets during a secondary break-up. Droplet size distribution obtained from the atomization process varies to the application. For the combustion in car engines, gas turbines, industrial furnaces, and rocket engines, effective atomization is required to achieve high evaporation and mixing rates since chemical reactions occur at the gaseous phase. While the evaporation of droplets and mixing of vaporized

fuel and oxidizer directly control the overall energy release rate, in the meantime, the presence of liquid fuels in the flame zone has a critical effect on the flame surface at which the corrugated structures leads to the flame instabilities, hence failure in the application. Therefore, the determination of droplet evaporation characteristics is essential for engine performance.

Atomized droplets may evaporate at different locations relative to the flame zone identifying the level of interaction between the flame and the droplet;

- *Pre-evaporation*: Droplets evaporate completely before the reaction zone. Pure gaseous phase combustion is observed.
- *Homogeneous combustion*: Droplets can reach the reaction zone and continue evaporating by feeding vaporized fuel to the flame. Local extinction phenomenon can be observed due to the excessive vapor build-up and consumption of oxidizer for rich flames.
- *Heterogeneous combustion*: Spray characteristics greatly influence the flame structure. Isolated or group droplet combustion can be observed.

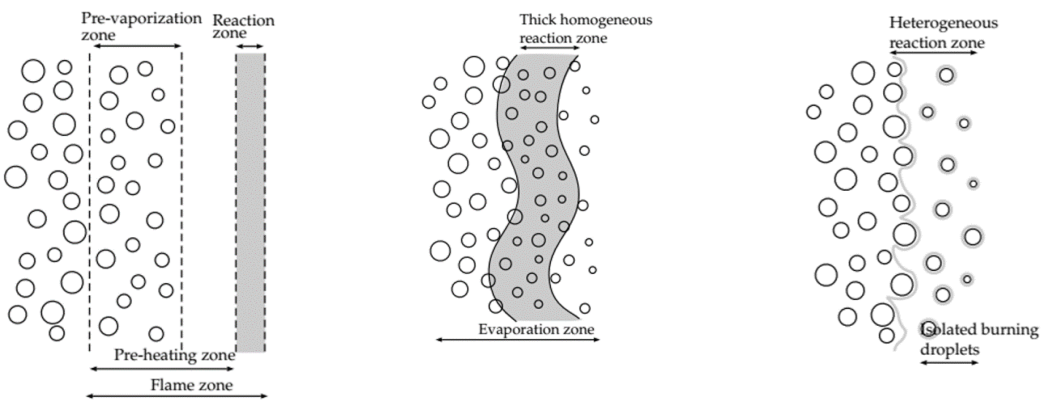


(a) (b) (c)

Figure 4.1: The interaction levels of a flame front and a spray; (a) Pre-evaporation (b) Homogeneous (c) Heterogeneous [86].

Depending on several parameters such as volatility of fuel, initial droplet size, initial position of injection and relative velocity between gas and droplet, etc., flame and droplet interaction level may highly change, as given in Figure 4.1. Since the liquid fuel spray disintegrates into individual and discrete droplets, the isolated droplet assumption is valid and provides extensive details to understand the physics of evaporation. Hence, the evaporation characteristics of the droplet and its interaction with the flame field should be investigated properly.

Today, with the help of advanced experimental techniques and computational capabilities with efficient numerical methods, the understanding of droplet evaporation and its interaction with the flame is enhanced. In the literature, there are numerous studies and reviews are available for experimental, theoretical and numerical aspects of the phenomenon [79, 22, 121, 131, 99, 15, 100].

### 4.1.1 Experimental Studies

Experimental investigations provide a good database for commonly used liquid fuels and validation of evaporation/combustion models. Several techniques are used to track the evaporation sequence of individual droplets, such as suspension, free falling, and levitation. Laser diagnostics are also implemented to detect changes in droplet properties for single and multi-component droplets.

In suspension technique, the droplet is suspended into quartz fibers [62, 54, 120], ceramic fibers [125, 126] or thermocouples [130, 35]. An example of cross quartz fiber technique to track the evaporation of ethanol from Saharin et al. [91] is shown in Figure 4.2.

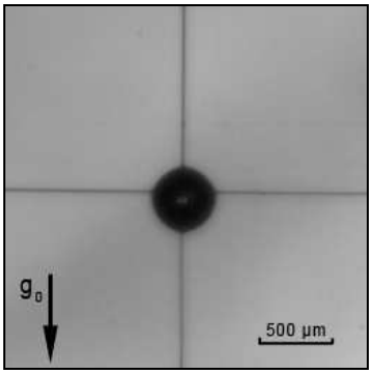


Figure 4.2: Cross quartz fiber supporting technique for droplet evaporation [91].

Nomura et al. studied this technique with silica fiber under microgravity conditions to measure the diameter change of n-heptane droplets in the $N_2$ ambient [69]. For droplets having 0.6-0.8 mm diameter, droplet lifetime was found to decrease as the ambient pressure increased at temperatures above 550 K. Ghassemi and co-workers also studied heptane and hexadecane evaporation using quartz fiber suspension technique for large droplets, $d_{p,0}$=1.1-1.3 mm [26]. They reported that at low ambient temperatures, droplet temperature is not uniform, leading to a deviation of surface temperature values from boiling temperature. In these conditions, evaporation does not follow the $d^2$-law. Saharin et al. studied ethanol, and 1-propanol evaporation at a relatively high-temperature environment (298-973 K) [91]. The effect of water condensation on the evaporation constant was observed at low ambient temperatures, especially for ethanol droplets. Recent studies with this technique focus on the impact of fiber properties on the droplet's evaporation lifetime. Chauveau and co-workers reported that the use of large fibers enhances the droplet evaporation rate due to the increased heat transfer for n-heptane droplets [19]. Rehman et al. also reported the same observations for large droplets, $d_{p,0}$=1565-2775 $\mu$m, while the effect of a metallic thermocouple was observed to be more dominant on evaporation rate [81]. Volkov and co-workers also concluded that the droplet fixation technique directly affects the temperature field by introducing the Laser Induced Florescence (LIF) technique [118]. Although this method provides a simple approach in terms of experimental setup and measurement of diameter change with the coupling of a camera, the effect of thermal conductivity of the support may

have an impact on the evaporation rate depending on the relative size of support to droplet and thermal conductivity of the support. Moreover, this method is more suitable for droplets having initial diameters larger than 1000 $\mu$m since it is difficult to suspend smaller droplets into the support.

In the free-falling method, droplet undergoes a free-falling motion, and the change in droplet size is captured via a camera [51, 105]. An example of a free-falling droplet is given in Figure 4.3.

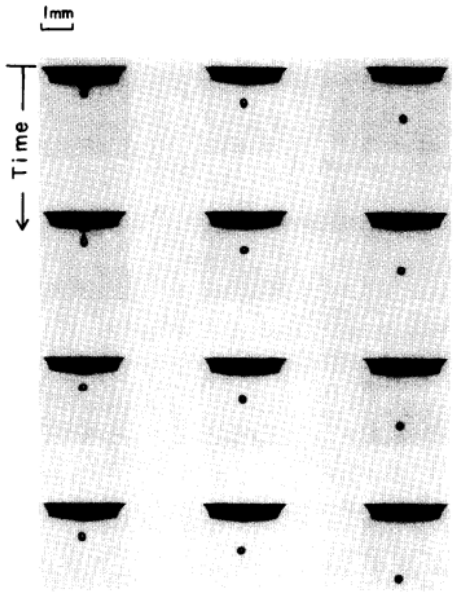


Figure 4.3: Sequence of droplet motion during free-falling [119].

Kumagai and co-workers performed free-falling experiments under microgravity for n-heptane droplets by measuring the burning rate [44]. In their further studies, Schlieren photographs of droplets are taken, and the effect of convection is studied for several alkane droplets [70]. They reported that initial droplet diameter has a little effect on measured evaporation constants. Wang and co-workers also tracked the diameter evolution of n-heptane droplets and managed to capture the micro-explosion phenomenon inside the droplet [119]. For ethanol droplets, Lee and Law performed measurements in dry and humid environments reporting that the condensation heat release and dilution of the droplet significantly modify the vaporization characteristics with a deviation from $d^2$-law [51]. Although this method is suitable for small-size droplets and the effects of fiber

as in the suspension method are no longer available, the free-falling technique requires a more complex experimental methodology. The position of the camera can be fixed with a wide angle, or it may be adapted to the changes in droplet position since the droplet is not stationary. Moreover, the relative speed between the droplet and its surroundings may impact the evaporation rate because the evaporation takes place in a convective environment.

In levitation method, the droplet is levitated and positioned inside a magnetic or acoustic field [128, 12, 33]. Yarin and co-workers developed a theoretical approach and designed experiments to measure droplet evaporation [127]. While they measured vaporization successfully, they also reported that studying the effect of forced convection in a strong acoustic field is impossible. With the help of this method, the shape of droplet is preserved as nearly spherical while its position is steady. However, there are two major drawbacks to this method. First, the acoustic field causes acoustic streaming near the droplet surface, affecting the vaporization characteristics. Secondly, the levitation method is not applicable at high-temperature environments due to increased evaporation rates. It should also be noted that the coupling of magnetic or acoustic fields should be treated carefully to have reasonable results.

Laser diagnostics, including Rayleigh scattering, LIF, and ILIDS, are also used to measure droplet parameters such as diameter, concentration, and temperature. In Diesel engine applications, Rayleigh scattering is coupled with Mie scattering to determine the spray characteristics [24, 2] . However, since Rayleigh scattering is shadowed by Mie scattering, simultaneous measurement is impossible for liquid and gaseous phases. Generally, first, the spray parameters are characterized via Mie scattering. Then, the vapor phase is captured with Rayleigh scattering to investigate the evaporation and burning of droplets.

Laser Induced Florescence (LIF) is a commonly used technique for combustion applications and the determination of droplet evaporation, especially for spray applications [55, 106, 116, 101, 114]. In LIF experiments, the intensity of the fluorescence signal is directly proportional to the molecular density, hence concentration. Zeng et al. and Düwel et al. used the LIF/Mie technique in their

studies to measure the Sauter Mean Diameter of spray and time dependence of diameter variation of the droplets [129, 23]. In their approaches, the spray is illuminated by a laser sheet, and simultaneous measurements are performed from fluorescence and scattering signals. LIF/Mie technique is reported to be efficient for non-evaporating spray systems; however, for evaporating and reacting systems, the local and temporal changes in tracer concentration must be considered. To achieve the measurement, laser dyes are used as fluorescent tracers, and the changes in tracer concentration inside the droplet, as well as the fluorescence signal of a droplet needs to be well-defined.

LIF technique is generally used to determine the temperature change of the liquid phase, as an example is given in Figure 4.4. Melton developed Laser Induced Exciplex Fluorescence (LIEF) technique to obtain the droplet temperature by adding fluorescent tracers in the liquid phase [58]. However, this technique is unsuitable for combustion applications since the measurement is sensitive to oxygen quenching. Lavieille and co-workers introduced a new approach by adding a fluorescent dye to the liquid phase [48]. They reported that temperature measurement accuracy is within 1 °C for single evaporating or combusting droplets. Castanet et al. applied the same technique for a moving combusting ethanol droplet at 200 $\mu$m diameter [17]. Labergue and co-workers introduced Phase Doppler Analysis to LIF measurements for spray applications and reported the effect of droplet size on fluorescence and the depth of field [45]. A similar approach was utilized by Maqua and co-corkers for the temperature detection of binary droplets at hot air ambient [55]. They reported that the accuracy in temperature measurement is 1.3 °C using a small amount of fluorescent organic dye to the fuel.

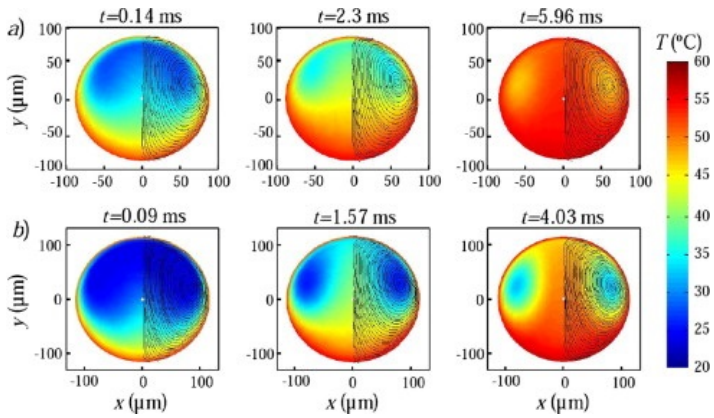


Figure 4.4: Temperature distribution inside an individual droplet captured via LIF technique [16].

Another measurement technique relying on laser diagnostics is Interferometric Laser Imaging Droplet Sizing (ILIDS) [43]. Sahu and co-workers used coupled ILIDS, and planar LIF (PLIF) techniques to study the evaporation of group droplets and changes in the gaseous phase with acetone droplets [92, 93]. In their studies, ILIDS was used to measure the individual droplet size, velocity, and number density in polydisperse sprays, while PLIF data provided vapor concentration distribution to characterize the evaporation. They achieved an effective coupling of ILIDS and PIV for acetone droplets by correcting the droplet center from ILIDS to measure the local vapor concentration with PLIF. Parant et al. also studied coupled PIV/PTV and ILIDS methods on a counter-current burner with dodecane droplets evaporating through methane/air flame [73]. They concluded that it is impossible to detect fringe patterns of the droplets at the zone close to the flame region via ILIDS. To overcome this problem, they introduced a new algorithm to PTV measurement so that the droplets could be followed correctly.

### 4.1.2 Theoretical and Numerical Studies

Comprehensive theoretical and numerical studies are carried out to predict the evaporation of a single droplet under various conditions. Many reviews are published on different methodologies and experimental comparisons by Williams [122], Law [49], Sirignano [102], Dwyer [22], Birouk and Gokalp [8], Sazhin [98] and recently by Zhifu et al. [132], Sazhin [99] and Raghavan [79].

Firstly, the classical model is proposed by Godsave and Spalding for a liquid droplet evaporating in a stationary gas environment at a fixed temperature and properties, leading to $d^2$-law [103, 27]. Convective heat and mass transfer of an evaporating droplet in the presence of a moving gas has been introduced by correlations in the form of Nusselt, $Nu$, and Sherwood, $Sh$ numbers. The liquid droplet can be treated as a hard sphere for low mass transfer rates, and the Ranz-Marshall classical convective heat and mass transfer relations are widely used [80]. It should also be noted that because the correlations of $Nu$ and $Sh$ numbers account for the effect of relative flow between the droplet and gas, the classical model is applicable when the gas is not stationary but moving with a velocity relative to the droplet with $Nu = Sh = 2$.

Analytical solutions for the gas phase variables are obtained in quasi-steady evaporation models, and the evaporation rate is calculated. Abramzon and Sirignano improved the classical model by incorporating the Stefan flow effect on the thicknesses of thermal and diffusional films based on film theory by introducing correction factors to $Nu$ and $Sh$ calculations [1]. The main assumptions of this model include variable thermo-physical properties, infinite thermal conductivity, non-unity Lewis number in the gas film, Stefan flow around the droplet, internal circulation, and transient heating in the liquid phase. Sazhin et al. observed the impact of the temperature gradient inside the fuel droplets on the evaporation process by comparing the effective and infinite thermal conductivities [97]. They reported that the temperature gradient within the droplets could significantly reduce evaporation time by increasing the surface temperature at the preheating phase. Haywood et al. conducted a study for a moving droplet by solving both gas and liquid flow within the droplet [40]. They reported that the quasi-

steady assumption used in a simplified droplet evaporation model is valid for low Reynolds numbers. The blowing effect due to surface evaporation significantly impacts the mass transfer, especially in high evaporation rate cases. Thermodynamic non-equilibrium effects are also considered for the classical model by Miller et al. by introducing Langmuir-Knudsen law and Clausius-Clapeyron law for surface vapor molar fraction calculation [60].

In the literature, alcohols and their blends are commonly used to validate proposed models due to the availability of well-established experimental results. Narasu and co-workers studied the evaporation of a single, bi-component ethanol/water droplet via the Abramzon-Sirignano model by taking the non-ideality of the mixture into account [65]. They performed calculations under 400 and 1200 K humid and wet convective air for bi-component droplets, and the lifetime of the droplet is reported to be increased in humid air due to the condensation of water on the droplet. Similarly, Santos et al. studied the non-ideality effects on high pressures for ethanol/water and ethanol/octane droplets under 300 K ambient [96]. Starinskaya and co-workers also modified the Abramzon-Sirignano model to estimate the recirculation effects based on the thermal conductivity/effective diffusivity model for ethanol/water droplets [104]. They concluded that the impact of heat supplied to the droplet via the support in the experiments is analogous to the thermal radiation energy absorbed within the droplet. Sacomano et al. studied the effect of thermodynamic equilibrium at the interface on the evaporation of ethanol and water droplets under low-temperature ambient [90].

### 4.1.3 Droplet Evaporation Under Flame Conditions

The interaction between droplets and flame is widely studied to determine the critical design parameters. Most of the studies include the spray formation with different burner configurations [117, 74, 9], especially to study the effect of droplets on flame speed [25, 87].

The injection of monodispersed droplets is studied to understand the effect of droplet spacing on evaporation. Sangiovanni and Labowsky studied the

injection of monodispersed fuel droplets having nearly 100-300 $\mu$m diameter into flat flame and recorded the change in droplet surface area [94]. They pointed out that while the lifetime of the droplet is consistent with the theoretical computations for large droplet spacing, isolated droplets evaporate more than the neighboring droplets. Russo and Gomez studied the effects of droplet and flame parameters on the extinction position of the droplet relative to the flame [88, 89]. They defined the Damköhler number of vaporization for ethanol droplets, $Da_v = (\bar{K}s/d_0^2\bar{v})^{0.75}$ where $\bar{K}$ is the average evaporation constant, $s$ is the radial distance of vaporizing region and $\bar{v}$ is the average radial velocity, as an indication of droplet passage criteria such that for $Da_v$<1, the droplet completely evaporates before the flame region. They also concluded that inter-droplet distance significantly affects the evaporation constant due to the change in vapor properties. Monodispersed ethanol evaporation was also reported by Castanet and co-workers using LIF and PDA for the size, temperature, and velocity of linearly streaming and combusting droplets [18].

## 4.2 Results and Discussions

Evaporation of an ethanol droplet is previously reported under flame conditions experimentally [82]. In this part of the study, single ethanol droplet experiments are reproduced by coupling PIV/PTV and ILIDS methods for methane/air flames, and the post-processing of the experiments is enhanced by introducing stagnation flame field computations. Simulations are also performed under similar conditions via the Spalding and Abramzon-Sirignano models to investigate the evaporation phenomenon under stationary burnt gases and stagnation flame fields, respectively. The droplet passage criterion is defined under methane/air flame for ethanol droplets and the evaporation constant is reported through a temperature gradient. Empirical correlations are proposed for evaporation constant as a function of gas temperature and flame parameters. Spalding numbers, heat, and mass evaporation rates are computed at different conditions and discussed.

### 4.2.1 Computation of Flame Characteristics

Laminar flame computations are performed with Cantera [28] in order to determine the flame characteristics of the experimental conditions, given in Table 3.2. Two flame configurations are used in the computations. The first one is 1D freely propagating adiabatic flame in which unstretched flame speed and adiabatic flame temperature can be computed. The second approach is a 1D detached flat flame stabilized at a stagnation point. In this configuration, the flame is stabilized in a strained flow field at an axisymmetric stagnation point with the presence of a wall. The location at which the flame is stabilized is dependent on the unburnt gas velocity, $U_0$.

Since the ethanol evaporation and changes in the gas phase due to ethanol vapor build-up are computed, the kinetic mechanism needs to include ethanol as a species participating in the reaction steps. Accordingly, the San Diego mechanism with 57 species and 268 reactions is used in computations [115].

1D freely propagating adiabatic flame field is computed using multi-species transport, which determines the rate of diffusion of each species, for $CH_4$/air (21% $O_2$ + 79% $N_2$ by volume) mixtures at 1 atm and 300 K. The domain length is set to 25 mm being the distance between the burner outlet and stagnation plate. The grid parameters (slope from 1 to 0.008, curve from 1 to 0.02 and prune as 0.003) are adjusted gradually to obtain a converged solution by increasing the number of grid points up to nearly 1500 in the computational domain.

Laminar flamespeed change with equivalence ratio is reported in Figure 4.5. The results are compared with the experimental results of Halter et al. [34] measured in a spherical combustion chamber and with the computed results using the well-known GriMech 3.0 mechanism. It is seen that for rich mixtures, the flamespeed is slightly underestimated with the San Diego mechanism compared to GriMech 3.0, while it is in a good agreement with the experimental measurements. The flame temperature and flame thickness is also reported in Table 4.1 for the experimental conditions.

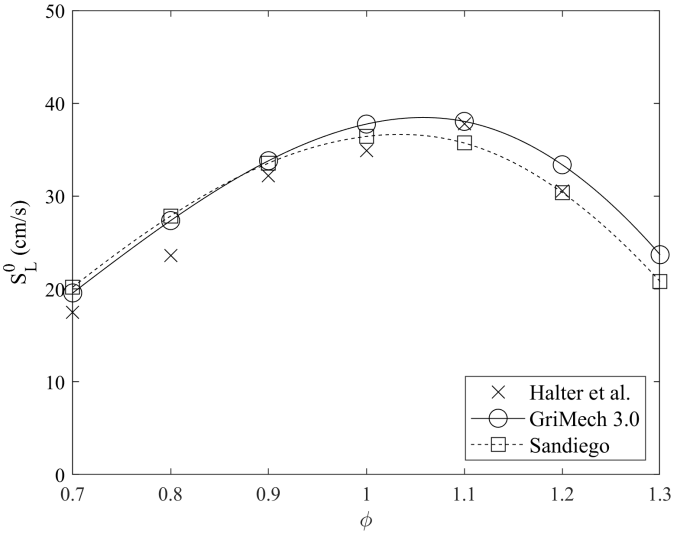


Figure 4.5: Comparison of unstretched $CH_4$/air flamespeeds measured by Halter et al. [34] and computed with GriMech 3.0 and San Diego [115] mechanisms at 300 K, 1 atm.

Table 4.1: Parameters of 1D freely propagating adiabatic $CH_4$/air flame computed with the San Diego mechanism [115] at 300 K, 1 atm.

| Condition | $\phi$ | $S_L^0$ (m/s) | $T_{adb.}$ (m/s) | $\delta_L^0$ ($\mu$m) |
|---|---|---|---|---|
| SBM-1 | 0.8 | 0.279 | 2001.4 | 517 |
| SBM-2 | 0.9 | 0.336 | 2137.1 | 469 |
| SBM-3 | 1.0 | 0.364 | 2227.1 | 455 |
| SBM-4 | 1.1 | 0.357 | 2212.7 | 458 |

1D stagnation flame field is also computed using multi-species transport at the same flame conditions to obtain more realistic results. The inlet velocity of the unburnt gases, $U_0$ is calculated based on the mass flow rates fed to the system in the experimental configuration. Since the stagnation plate temperature is not measured experimentally, first, the sensitivity of the flame temperature to the plate temperature is studied. As it is reported in Table 4.2 that for the plate temperature ranging between 300-1500 K, the flame temperature is changing

nearly by ±2 K. Since the injected droplets are evaporating in the burnt gases and cannot reach the plate, the plate temperature is assumed to be constant at 500 K for all computed cases.

Table 4.2: Change in flame parameters with stagnation wall temperature, $T_{plate}$ for SBM-1.

| $T_{plate}$ (K) | $S_L$ (m/s) | $T_f$ (K) |
|---|---|---|
| 300 | 0.3006 | 1991.35 |
| 400 | 0.3008 | 1991.39 |
| 450 | 0.3003 | 1991.58 |
| 500 | 0.3003 | 1991.59 |
| 550 | 0.3008 | 1991.60 |
| 600 | 0.3007 | 1991.62 |
| 750 | 0.3007 | 1991.59 |
| 1000 | 0.3008 | 1991.88 |
| 1250 | 0.3009 | 1992.09 |
| 1500 | 0.3013 | 1992.35 |

Velocity and temperature profiles of adiabatic and stagnation flames are reported for a stoichiometric case in Figure 4.6. For the adiabatic case, the flamespeed is equal to the unburnt gas velocity, whereas, for the stagnation case, there are different approaches in the literature [10]. In the majority of the studies, the flamespeed is reported as the minimum velocity before the flame zone. As seen from Figure 4.6a, stagnation flamespeed is slightly higher than the adiabatic one depending on the inlet velocity of the unburnt gases, $U_0$. It also depends on the domain length at which the flame needs to be stabilized, while the no-slip condition should be satisfied at the end of the domain due to the presence of a stagnation wall. As can be seen in Figure 4.6b, the burnt gases temperature is slightly lower in the stagnant flame configuration due to heat loss through the stagnation plate.

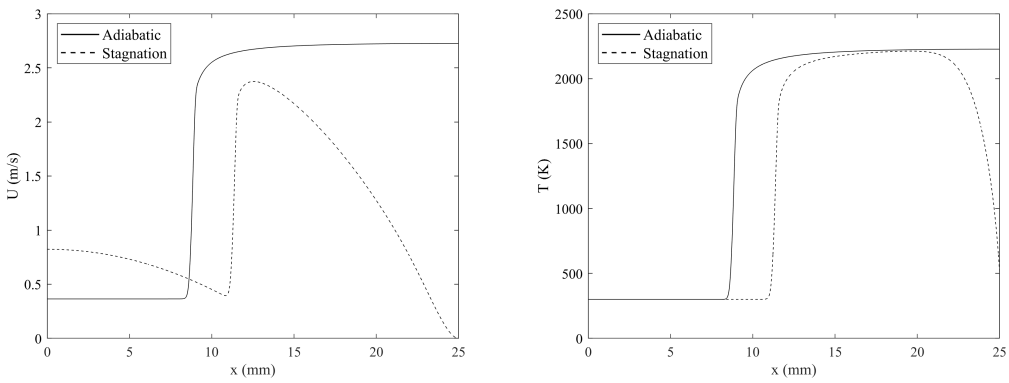


(a) (b)

Figure 4.6: Comparison of 1D freely propagating adiabatic flame and 1D stagnation flame at SBM-3 (a) Velocity profile (b) Temperature profile.

Computed flame speeds, $S_L$ and flame temperatures, $T_f$ are given in Table 4.3 for all the experimental conditions.

Table 4.3: Parameters of 1D stagnation $CH_4$/air flame computed with the San Diego mechanism [115] at 300 K, 1 atm ($T_{plate}$=500 K).

| Condition | $\phi$ | $U_0$ (m/s) | $S_L$ (m/s) | $T_f$ (m/s) | $\delta_L$ ($\mu$m) |
|---|---|---|---|---|---|
| SBM-1 | 0.8 | 0.560 | 0.303 | 1991.6 | 527 |
| SBM-2 | 0.9 | 0.743 | 0.364 | 2123.2 | 481 |
| SBM-3 | 1.0 | 0.824 | 0.394 | 2212.2 | 469 |
| SBM-4 | 1.1 | 0.699 | 0.379 | 2202.4 | 474 |

#### 4.2.1.1 Stagnation Flame Field Determination

Temperature field can be measured experimentally with Rayleigh scattering [4]. However, the Rayleigh scattering signal is completely shadowed by the Mie scattering signal, which is used in this study for velocity measurements. Therefore, the temperature field of the gas cannot be obtained experimentally during PIV/PTV measurements. Instead, 1D temperature profiles of computed stagnation flames are fitted to the corresponding experimental field for each case, as in Figure 4.7 for $\phi$=0.8.

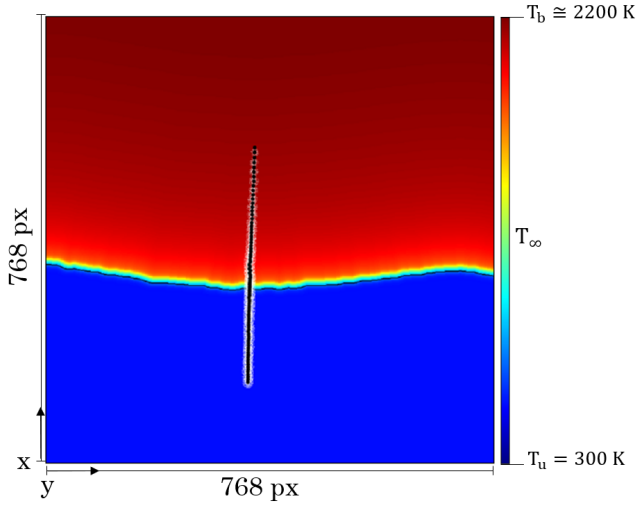


Figure 4.7: Fitted stagnation temperature profile and droplet trajectory for SBM-1 with an ethanol droplet trajectory ($d_{p,0}$=47 $\mu$m).

From PIV results, the position of the flame front is determined based on the presence of DEHS droplets. By taking the isotherm, $T$=525 K being the evaporation temperature of DEHS droplets, calculated temperature profiles, thermodynamic, and transport properties are fitted to the experimental flame field to track the droplet evaporation through the flame field experimentally.

### 4.2.2 Stationary Droplet Evaporation

#### 4.2.2.1 Numerical Setup

For evaporation computations, an isolated ethanol droplet having 50 $\mu$m initial diameter is injected at $T$=300 K and $P$=1 atm at the center of a large Cartesian cube with dimensions $10 \times 10 \times 10$ cm$^3$ to avoid edge effects. Computational domain is shown in Figure 4.8. Evaporation of the droplet is tracked until complete evaporation at a constant temperature and stagnant ambient with pure $N_2$ (373-2250 K) and burnt gases (1800-2200 K) via the Spalding model. Burnt gas compositions are computed in Cantera for $CH_4$/air flames at equivalence ratios between 0.8-1.1. Droplet diameter and temperature, and Spalding numbers are computed during evaporation.

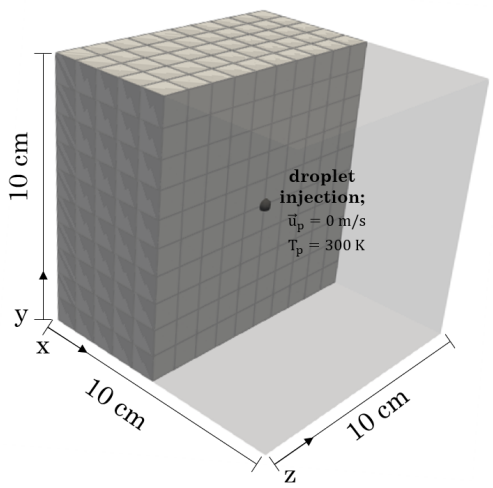


Figure 4.8: Computational domain of a stationary droplet evaporation.

#### 4.2.2.2 Evaporation Under Pure $N_2$ Ambient

The first comparison between the experimental and numerical ethanol droplet evaporation rates is performed under stagnant $N_2$ ambient conditions. Saharin et al. studied the evaporation of isolated, anhydrous ethanol droplets using cross fiber technique [91]. The experiments were performed under $N_2$ ambient at varying temperatures between 373-673 K, and the temporal evolution of the droplet

diameter was recorded using a high-speed camera. The results are presented in Figure 4.9, with the numerical results of the corresponding cases.

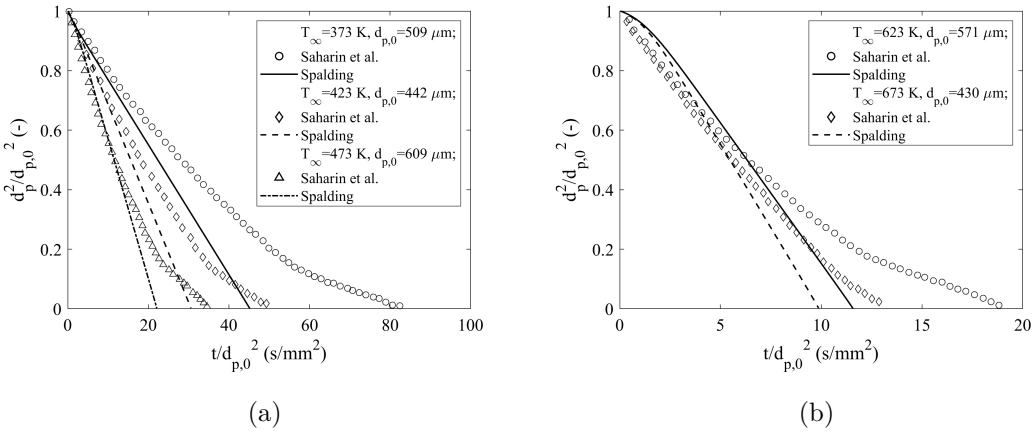


(a) (b)

Figure 4.9: Comparison of ethanol droplet evaporation from the experiments of Saharin et al. [91] and simulations via Spalding model under pure $N_2$ ambient at $P$=1 atm and at (a) low temperatures (b) high temperatures.

Saharin et al. observed a deviation from the linear evaporation profile due to the condensation of water vapor on the droplet surface and the simultaneous evaporation of ethanol and water. The condensation effect is observed to be more critical at lower ambient temperatures because of the high miscibility of ethanol to water. However, for high-temperature cases, an almost linear behavior is observed for ethanol evaporation with a higher droplet lifetime than the one computed with the Spalding model. Due to the experimental technique used in the measurements, it is expected to observe lower evaporation constant since the effects of heat conduction in the quartz fiber are limited [19]. Moreover, low-temperature ambient results deviate more than those computed with the Spalding model since the presence of water delays evaporation as a low-volatility substance. The comparability of the Spalding model results with the experiments can be discussed for the initial phase at which the evaporation of ethanol is observed. It is seen that the slope until the second linear part agrees well with the numerical results, especially at higher ambient temperatures.

#### 4.2.2.3 Evaporation in the Presence of Burnt Gases

The temporal evolution of the droplet diameter having an initial value of 47 $\mu$m and evaporating under stoichiometric conditions is reported in Figure 4.10. Raw ILIDS measurements are denoted by diamond markers, as well as the fitted profile with least square regression to observe the linearity during evaporation.

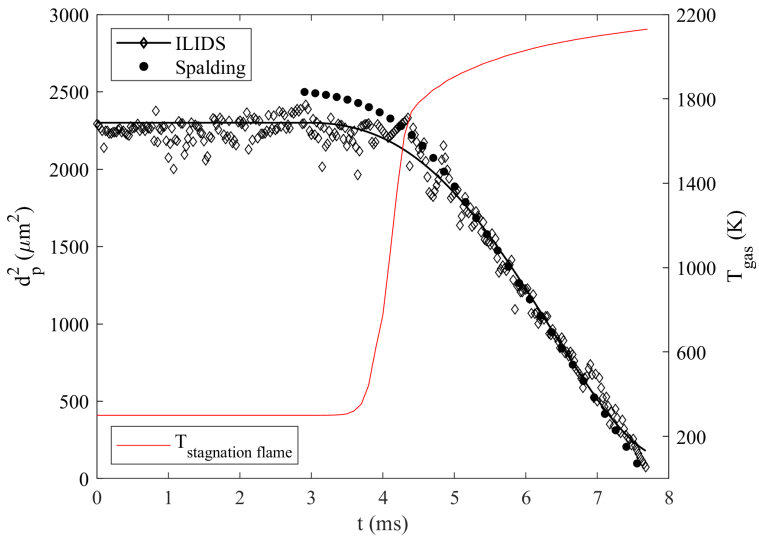


Figure 4.10: Temporal evolution of droplet diameter with ILIDS ($d_{p,0}$=47 $\mu$m, $T_{evap,average}$=2020.5±2.5 K) and Spalding model ($d_{p,0}$=50 $\mu$m, $T_\infty$=2000 K) in stagnant ambient conditions (SBM-3).

For the simulations, the droplet diameter is kept constant at 50 $\mu$m, which causes minor differences with the experimental measurements because the latter contains a high sampling of droplets between 20-70 $\mu$m. For the experimental measurements, it should be noted that there might be slight changes in droplet measurement for different cases due to the difference in the initial position of the captured droplet and the droplet diameter measurement quality at specific frames. Since individual droplets are selected over all recorded experimental data, some droplets are initially tracked closer to the flame front. Therefore, the measured droplet trajectory is shorter for these droplets, making them difficult to follow. Also, for the post-processing of ILIDS data, Power Spectral Density (PSD) is estimated in two different orders at each frame to calculate

the number of fringes. It is observed that for larger droplets, both methods give comparable results, while higher order PSD captures the number of fringes in a more reliable way for smaller droplets. This approach is generalized for all computations. Therefore, there may be some local deviations with a small error on the droplet diameter captured at certain positions, especially close to the flame region where the change in diameter is expected to be higher in a shorter distance due to the steep temperature profile. Nevertheless, the accuracy of the diameter measurement can be assumed to be quite good at the flame zone, as reported in Figure 4.10.

The ambient temperature is defined as average for the experiments calculated from the beginning to the end of the evaporation curve. There is almost a 3 K difference between stagnation and adiabatic profiles for the average value. In contrast, the difference becomes 8 K and 1 K when the droplet starts to evaporate and its lifetime ends, respectively. In other words, it is slightly harder to define an exact ambient temperature for sufficiently small droplets that completely evaporate inside the reaction zone. However, for the droplets spending most of their time in the burnt gases, evaporation temperature can be assumed to be equal to the burnt gas temperature, regardless of the exact position of the droplet with respect to the flame. Nevertheless, it should also be noted that the estimation of the temperature profile is directly linked to the stagnation plate temperature causing $\pm 2$ K temperature difference at the evaluated conditions.

At the initial stages of preheating, slightly different behavior is observed between the data from experiments and simulations. This can be explained by the fact that the droplet meets immediately with the hot surroundings in the simulations. However, experimentally, the droplet spends enough time to adjust its velocity in the unburnt gases and gradually enters the reaction zone. In order to make a good comparison of droplet lifetime, the evaporation rate, being the slope of $d^2$ vs. t, is computed over the diameter change interval. At the given condition in Figure 4.10, evaporation constant, $K$ is reported as 0.67 and 0.55 $mm^2/s$ from ILIDS measurements and Spalding computations, respectively. Two reasons can explain the difference between these values. First, both the droplet and the surroundings are not stationary in the experimental measurements, which

can cause convection and circulation effects. Secondly, the droplet is actually evaporating through a temperature field, and the time spent at each isotherm is minimal due to the steep variation of the profile.

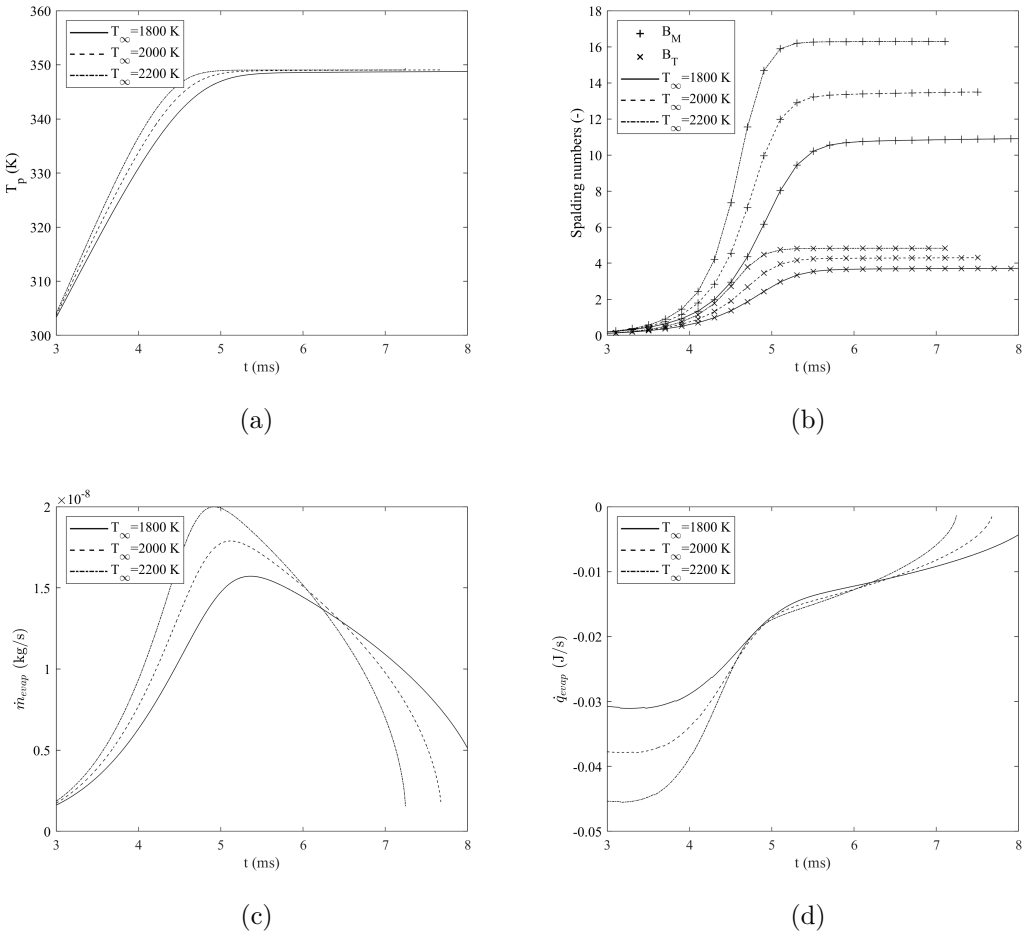


Figure 4.11: Temporal evolution of droplet parameters in the stoichiometric conditions (SBM-3) (a) Droplet temperature (b) Spalding numbers (c) Mass evaporation rate (d) Heat evaporation rate.

Figure 4.11a shows the temporal evolution of the droplet temperature at different ambient temperatures. Narasu et al. reported that the ambient composition has an influence on the droplet surface temperature, causing water condensation at lower ambient temperatures [65]. Considering the fact that one of the main products of the combustion is water, it is observed that the droplet temperature evolution trend is nearly the same under flame conditions and pure $N_2$ ambient. Therefore, it can be concluded that the condensation effect of water is negligible

at high-temperature conditions for ethanol droplets.

It can also be concluded that at higher ambient temperatures, droplet temperature reaches slightly higher values with a higher slope, which can also be observed from the trend of mass (Figure 4.11c) and heat (Figure 4.11d) evaporation rates. Also, the Spalding mass number almost doubled with a 400 K ambient temperature difference, leading to higher mass and thermal energy transfer between the droplet and surroundings.

### 4.2.3 Droplet Injection Through Stagnation Flame Field

#### 4.2.3.1 Numerical Setup

In order to investigate the droplet behavior interacting with a flame, a droplet is injected through a 2D stagnation flame field. The computational setup is represented in Figure 4.12. The domain size is determined based on the burner configuration, at which 25 mm is the distance from the burner exit to the stagnation plate and 15 mm is the diameter of the premixed inlet chamber at the burner exit. 200 $\mu$m mesh resolution is obtained at a Cartesian grid.

Flame initialization is performed from previously computed 1D freely propagating adiabatic flame field in YALES2, and the initial position of the flame is determined based on Cantera simulations. Premixed gases are injected from the bottom boundary at the corresponding conditions. For the top boundary, the wall boundary condition is set at 500 K constant temperature. Outlet boundary conditions are set for right and left boundaries. Depending on the case, 2D flame field computations are performed until a steady state solution is obtained at CFL=0.4 for 4000-7000 iterations. The flame position is determined from the maximum value of $CH_3$ species profile.

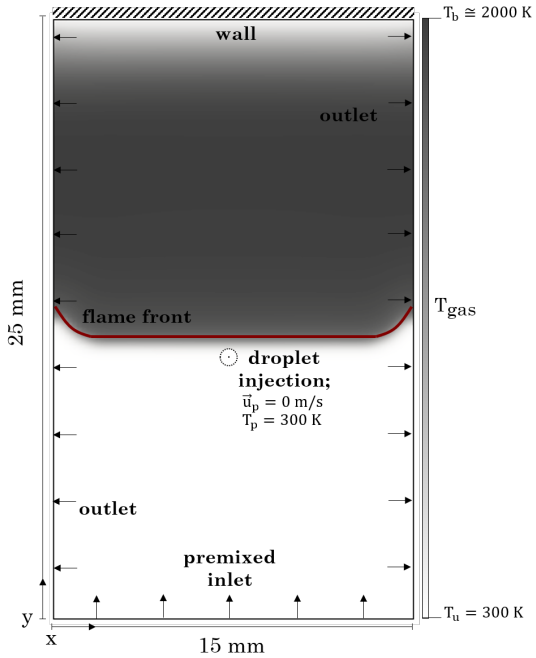


Figure 4.12: Sketch of the computational domain for 2D $CH_4$/air stagnation flame (SBM-1, $T_{plate}$=500 K).

An isolated ethanol droplet is injected into the steady 2D flame field at $T$=300 K without an initial velocity for evaporation computations. In order to preserve the sphericity of the droplet, 3$^{rd}$ dimensional distance is set to 15 mm along the z-direction. The initial position of the droplet is selected such that the droplet is injected from unburnt gases having enough time to be carried by the gas flow. In order to eliminate the effect of the initial droplet position, all droplets are injected at a point 1.5 mm below the flame position for all computed cases. The initial droplet diameter is set to 35, 50, and 65 $\mu$m for each case to compare well with the experimental cases. The evaporation of the droplet is tracked until complete evaporation via the Abramzon-Sirignano model. Changes in droplet parameters, as well as the gas properties, are computed during the evaporation process.

#### 4.2.3.2 Evaporation Through Laminar $CH_4$/Air Flame

Velocity measurements are performed for the droplet and unburnt gas via PTV and PIV, respectively. In Figure 4.13, velocity profiles of the unburnt gases of a stoichiometric flame measured up to the $T$=525 K isotherm and the ethanol droplet with an initial diameter of 50 $\mu$m, as well as the computed profiles, are reported. The alignment of experimental and numerical data is achieved with $T$=525 K isotherm.

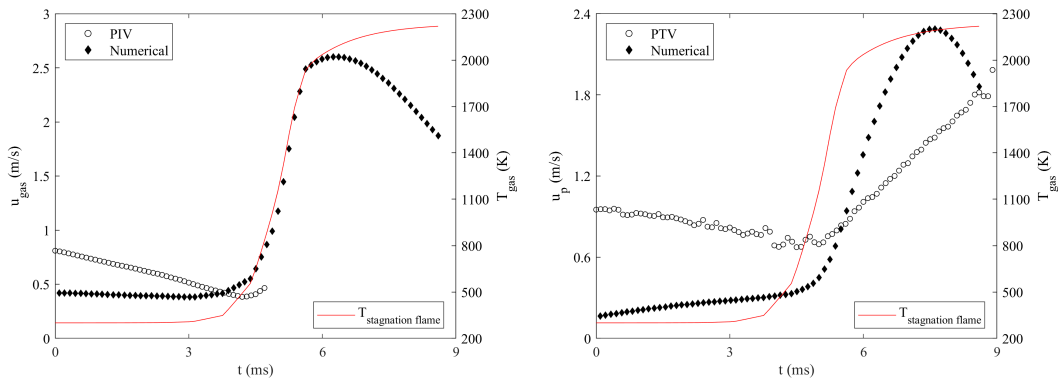


(a) (b)

Figure 4.13: Temporal evolution of computed and measured (a) gas and (b) droplet velocities at SBM-3 ($d_{p,0}$=50 $\mu$m).

Gas velocity computations show that for the stagnation flame configuration, the velocity profile has a decreasing trend after the reaction zone due to the presence of a stagnation plate at which no-slip boundary condition is assumed to comply. It is observed for unburnt gas velocity comparison that there is a slight difference in the initial velocities of unburnt gases between PIV measurements and stagnation flame computations because of the fact that reported PIV data is calculated along the droplet path, and the first detection of the droplet is achieved after a certain distance from the burner outlet, as can be seen in Figure 4.7. Since the precision of the temperature profile is based on one isotherm ($T$=525 K), it may not be accurate to report the exact location of the first droplet detection relative to the flame zone. It can still be concluded that PIV measurements provide reliable data, especially near the flame zone. The lowest

velocity value before the flame zone, which is accepted as the flamespeed for stagnation flames, is measured as 0.383 m/s via PIV, while numerically, it is computed as 0.389 m/s. Considering the other flame conditions, flamespeed can be reported with an average difference of 2±0.5 % between experiments and computations. It should also be noted that the presence of DEHS droplets (≈ 2-3 $\mu$m) does not have an effect on the gas velocity measurements [83].

Figure 4.13b shows the temporal change of the droplet velocity while traveling through the flame field. It is seen that as soon as the droplet enters the flame region, it accelerates due to the loss of mass; hence, it is subject to less drag force. It also is known that the relative velocity between gas and liquid phases directly affects the motion of the droplet, in addition to the evaporation rate. The convection and its effects around a droplet and the Marangoni effect at the interface are critical to correctly predict local and global evaporation rates. Stokes number, $St$ characterizes this effect as being the ratio of characteristic time of the droplet to characteristic time of the gas:

$$St = \frac{\tau_p}{\tau_g} = \frac{\frac{\rho_p {d_p}^2}{18\mu_g}}{\frac{\delta_L}{u_g}} \tag{4.1}$$

For droplets having an initial size in the range of 20-70 $\mu$m under reported flame conditions, the characteristic time of the droplet is much lower than that of the gas; hence $St$ number is below one. Therefore, it can be concluded that the droplets are small enough to be carried by gas flow with a slight slip velocity. However, for $St < 0.1$, which corresponds to the droplets having an initial diameter greater than 5 $\mu$m, the accuracy of the assumption is questionable. Hence, particle Reynolds number, $Re_p$ is computed and plotted in Figure 4.14 for the stoichiometric flame and 50 $\mu$m initial droplet diameter.

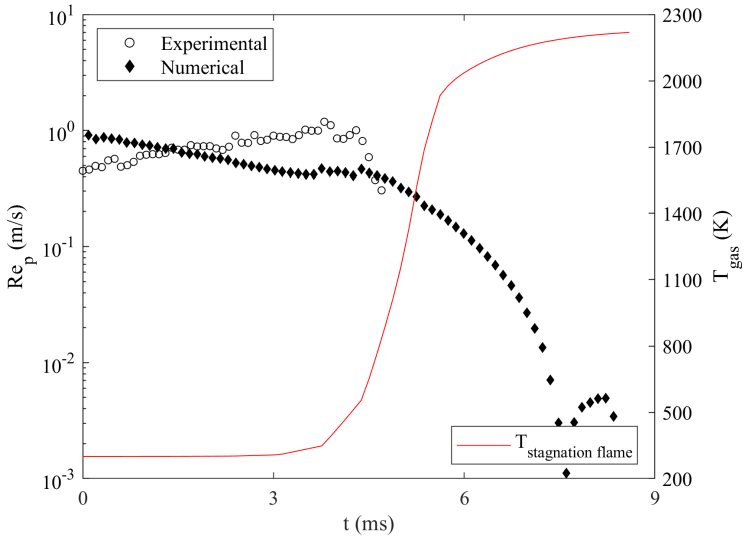


Figure 4.14: Temporal evolution of particle Reynolds number at SBM-3 ($d_{p,0}$=50 $\mu$m).

It is seen that in the entire domain, the value is below 0.1 for all droplets demonstrating that convective effects from the surroundings are inconsequential for the droplet. Although the relative velocity is higher at the burnt gases, $Re_p$ decreases due to the increase in gas density and viscosity.

Figure 4.15 shows the spatial and temporal evolution of an ethanol droplet at stoichiometric conditions for 50 $\mu$m initial diameter. It is seen that during the initial 8 ms, the droplet moves towards the flame front at a constant size since the ambient temperature is 300 K. Initial heating period is observed for the following 1 ms in the region where the diameter evolution profile starts to create a slope smoothly. The last phase, between 9-13 ms, is the evaporation of the droplet, obeying the $d^2$-law.

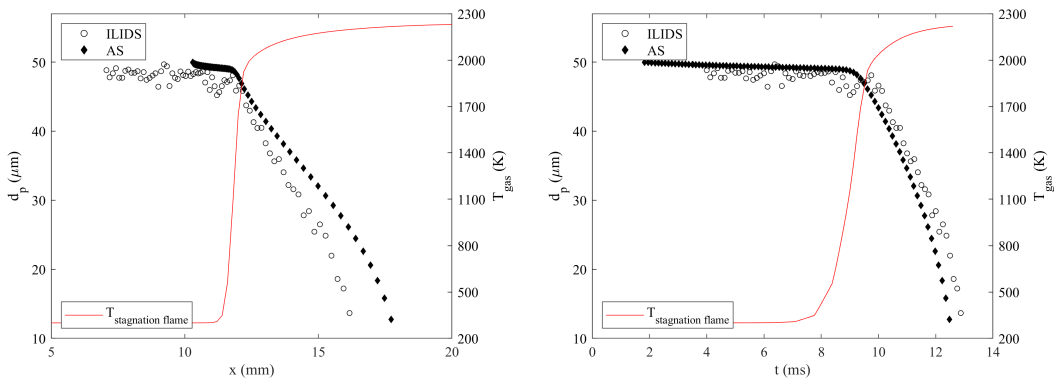


(a) (b)

Figure 4.15: (a) Spatial and (b) temporal evolution of droplet diameter with ILIDS and Abramzon-Sirignano model at SBM-3 ($d_{p,0}$=50 $\mu$m).

The dynamics of the droplet are solved with the Lagrangian approach (Equations 2.41-2.43) and as it is seen from Figure 4.15a, the final location of the droplet is slightly overestimated by 10 % error compared with the experimental results, although almost identical trend is observed. First of all, experimentally, the initial position of the droplet is detected via PTV, and the exact distance between the droplet and the flame may slightly differ for each droplet depending on the initial size and detection time. However, for the simulations, the droplet is injected without an initial velocity from 15 mm below the flame zone. This situation will cause differences in the drag force acting on the droplet due to the variations of droplet and gas velocity. At the initial phases, the gas velocity will be higher than the velocity of the droplet up to almost 5 m/s, as seen from Figure 4.13. After this time, the velocity of the droplet will always be lower than that of the gaseous phase. Furthermore, the effect of a non-gravity simulation environment may cause the acceleration of the droplet, unlike to the experiments which are conducted under terrestrial gravity conditions. Temporal evolution of the droplet, given in Figure 4.15b is well captured numerically.

Figure 4.16 shows the change in droplet temperature and Spalding numbers, as well as the mass and heat evaporation rates at stoichiometric conditions for three different particle sizes. Evaporative properties are linearly increasing with

the initial droplet diameter, as expected. However, the largest droplet spends more time in the reaction zone which slightly increases its evaporation rate by 0.01 $mm^2/s$ as it can be seen in Figure 4.18.

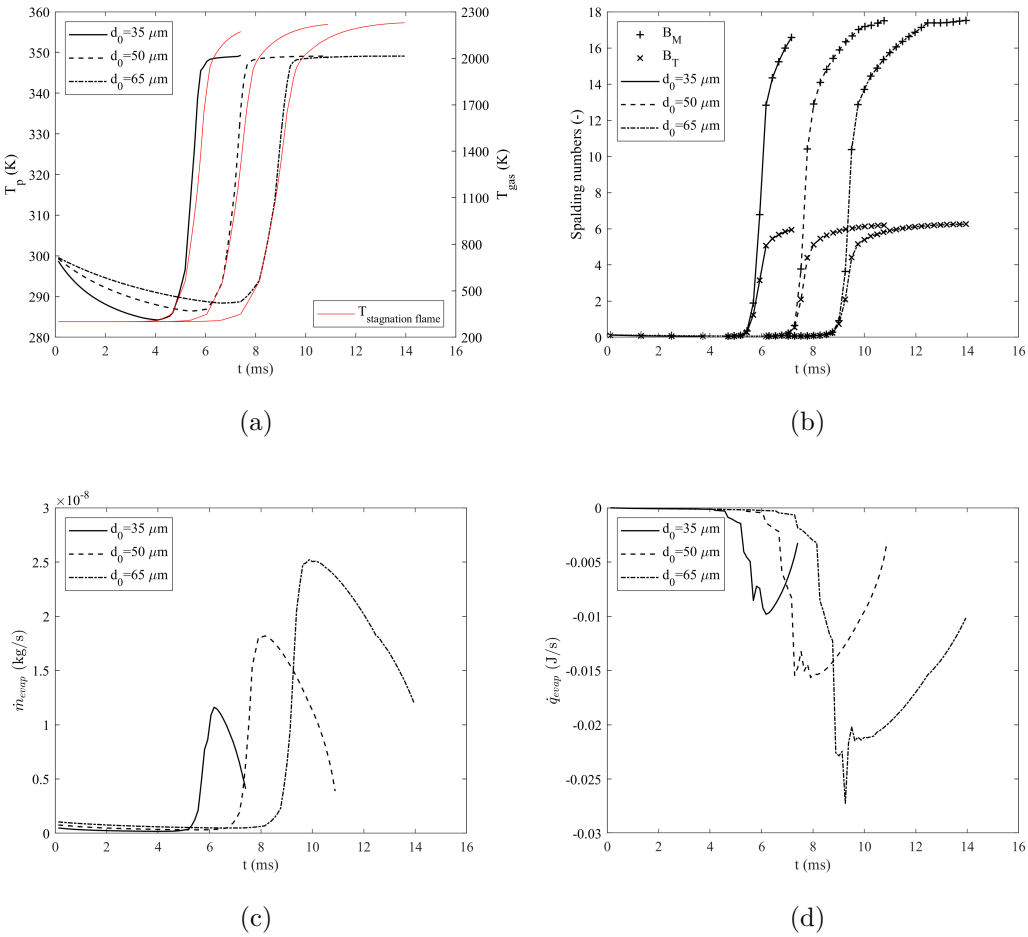


Figure 4.16: Temporal evolution of droplet parameters at stoichiometric conditions for an ethanol droplets having $d_{p,0}$=35, 50 and 65 $\mu$m (a) Droplet temperature (b) Spalding numbers (c) Mass evaporation rate (d) Heat evaporation rate.

The effect of flame condition on the evaporative properties of the ethanol droplet is reported in Figure 4.17. Droplet temperature increases until the boiling temperature of ethanol, nearly 351 K, and the droplet spends most of its time inside the preheating zone while being heated. Lower gas velocity leads to lower droplet velocity at $\phi$=0.8, hence the heating of the droplet delays.

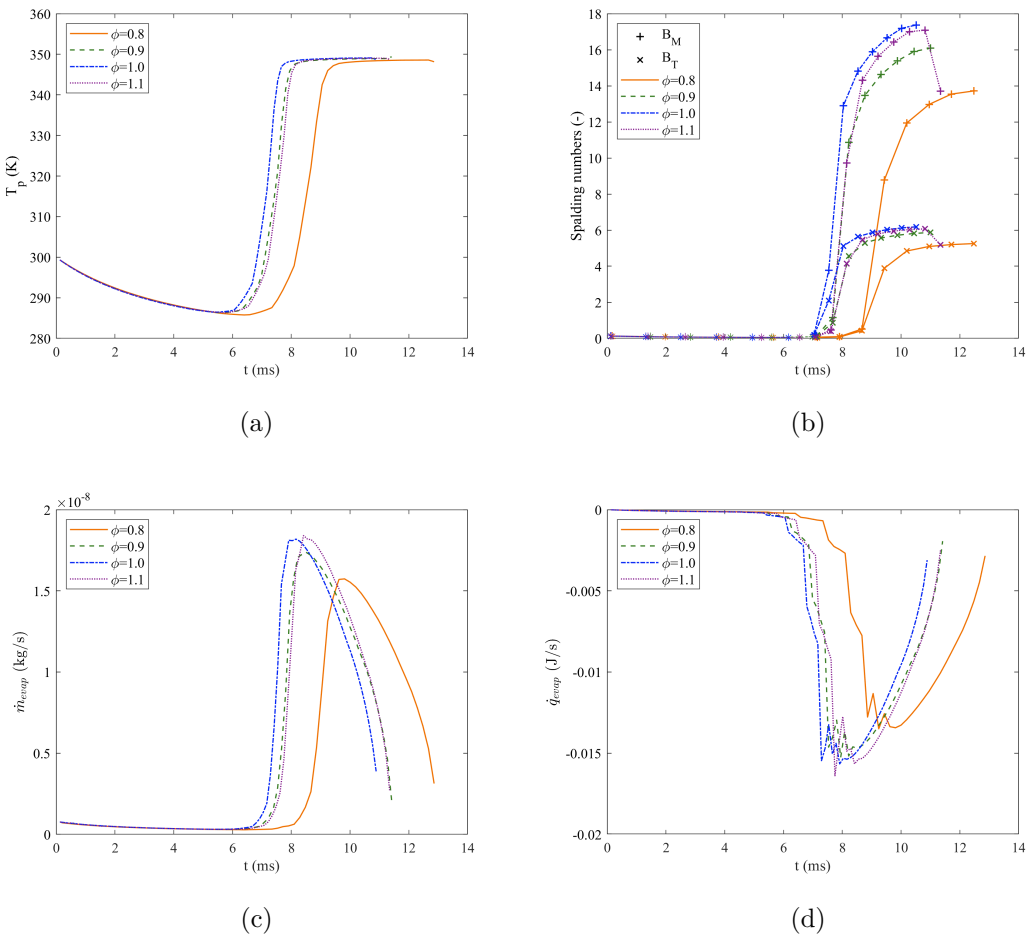


Figure 4.17: Temporal evolution of droplet parameters at different flame conditions for an ethanol droplet having $d_{p,0}$=50 $\mu$m (a) Droplet temperature (b) Spalding numbers (c) Mass evaporation rate (d) Heat evaporation rate.

#### 4.2.3.3 Rate of Evaporation

In order to obtain droplet evaporation rate from d$^2$-law given in Equation 2.57, slope of $d^2$ vs. $t$ is computed over the diameter change interval. Figure 4.18 shows the dependency of the evaporation constant on the initial droplet size. The variability of the initial diameter provides a good database for the evaporation constant computed under the same conditions. However, to clarify the effect of flame condition on evaporation, mean $K$ values are computed and reported over all samples at each equivalence ratio with the error bars.

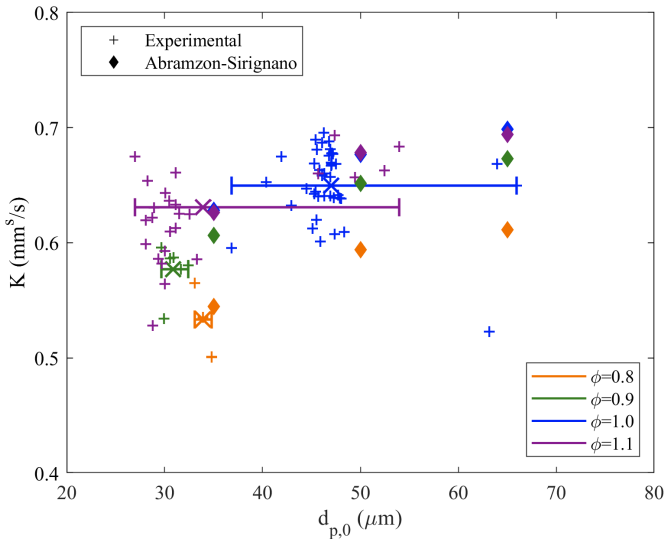


Figure 4.18: Changes in ethanol evaporation constant with respect to the initial droplet diameter at different equivalence ratios.

For stoichiometric and rich flame conditions, large error bars are observed. It can be clearly seen that the majority of $K$ values are located around 0.62 and 0.65 mm$^2$/s for $\phi$=1.1 and 1.0, respectively. Therefore, it can be concluded that there is no major dependency of the evaporation constant to the initial size of the droplet at elevated conditions, as it is expected from d$^2$-law. Nevertheless, slight deviations can be observed due to different experimental conditions and the initial condition of the droplet affecting the time spent at a specific temperature interval. It should be noted that this is mostly due to the high sampling at these equivalence ratios and the differences in the initial conditions of droplets. As it is explained previously, the droplets are tracked initially at different locations since isolated droplets are selected from the whole experimental recording. Although the initial location of each droplet is almost the same, its velocity may vary, which directly affects the temperature exposure time at the flame zone, consequently, the evaporation constant. It is also known that the vaporization rate of large droplets may be affected by drag forces, although the computed $Re_p$ numbers are quite small in order of magnitude sense.

Instead of selecting some droplets, the mean values of K, mean interval temperature, minima, and maxima to report the evaporation temperature range are

computed and given in Figure 4.19 over all samples at each equivalence ratio, indicated as ILIDS. Experimental results are compared with the literature (Saharin et al. [91]) and numerical simulations for a stationary droplet (Spalding) and a moving droplet through the stagnation flame field (AS).

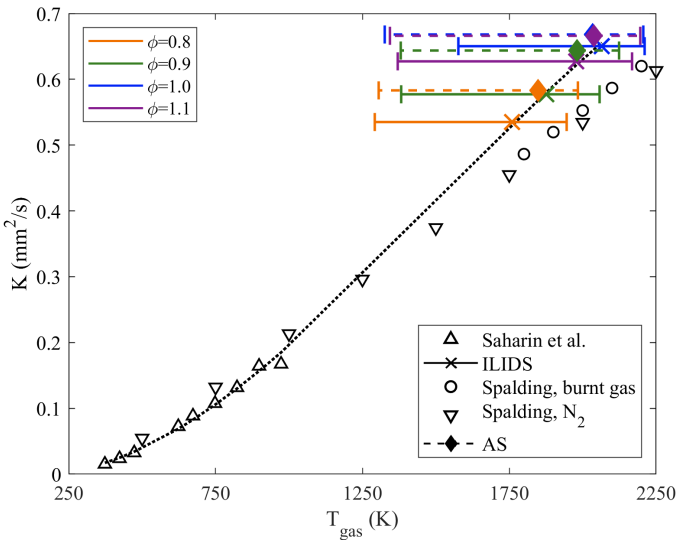


Figure 4.19: Comparison of ethanol evaporation constant with respect to ambient gas temperature.

For stationary droplets, evaporation computations are performed via the Spalding model for each equivalence ratio at the ambient temperature varying between 1800-2200 K and at the burnt gas compositions, as well as at the flame compositions. The evaporation constant is observed to be almost the same for all flame conditions due to the fact that the compositions of major species, such as $CH_4$, $CO_2$, $H_2O$, are practically similar, and the composition of ethanol at the ambient is nearly negligible. For stoichiometric flame condition, the difference between the evaporation constants at lower ambient temperatures (1800-1900 K) is $\approx$0.02 mm$^2$/s, which decreases as temperature increases. However, it is clearly seen that the ambient gas composition has no significant effect on evaporation under evaluated conditions. Therefore, for clarity, only one case is included since the computed evaporation constant is almost the same at different equivalence ratios for the case of a stagnant burnt gas ambient. The Spalding model overestimates the evaporation rate for low temperatures when it is compared with

the experimental results of Saharin et al. [91].

For moving droplet cases, the evaporation temperature is selected as the mean temperature in an interval where the droplet starts evaporating and its lifetime ends since there is no way to measure the exact evaporation temperature of a moving droplet in a flame field. Still, the maxima of the measured evaporation constants are very close to the numerical results obtained from both the Abramzon-Sirignano and Spalding models. It is seen that the Abramzon-Sirignano model slightly overestimates the vaporization constant for lean cases while the values are still in the trend of experimental measurements.

In order to investigate the dependence of evaporation constant to ambient temperature, an exponential type of relationship can be used since rapid growth at low temperatures with the asymptotic behavior in Figure 4.19:

$$K(T_{gas}) = AT_{gas}^{\beta} exp\left(\frac{-E_a}{RT_{gas}}\right) \tag{4.2}$$

Table 4.4 reports the values obtained by fitting Equation 4.2 to the experimental results. However, it can be clearly seen from Figure 4.19 that $K$ is not only a function of ambient gas but also changes depending on the flame properties. Moreover, it is hard to determine the exact gas temperature for a moving droplet in a varying ambient temperature. Hence, it would be beneficial to estimate the vaporization rate depending on the flame characteristics. Accordingly, a new exponential type of relation is proposed by introducing flame thickness, flame speed, and flame temperature, as in Equation 4.3.

Table 4.4: Coefficients of an exponential relation for evaporation constant, $K$ depending on $T_{gas,average}$.

| $A$ | $\beta$ | $E_a$ |
|---|---|---|
| 7.9x10$^{-4}$ | 0.947 | 8429 J/mol |

$$K(T_f, S_L, \delta_L) = A' \left(\frac{\delta_L}{S_L}\right)^{\gamma} T_f^{\beta} exp\left(\frac{-E_a}{RT_f}\right) \tag{4.3}$$

While activation energy, $E_a$ and the power dependence of temperature, $\beta$ are kept constant, it is seen that the fitted parameters provide very close com-

putations of evaporation constant for an ethanol droplet evaporating through methane/air flame field at $\phi$=0.8-1.1. Additionally, the small value of $\gamma$ indicates that the evaporation constant slightly depends on the characteristic flame time. The main governing parameter on evaporation can be interpreted as the flame temperature, $T_f$.

Table 4.5: Coefficients of an exponential relation for evaporation constant, $K$ depending on flame parameters.

| $A'$ | $\gamma$ | $\beta$ | $E_a$ |
|---|---|---|---|
| 8.9x10$^{-4}$ | 0.030 | 0.947 | 8429 J/mol |

#### 4.2.3.4 Droplet Passage Criteria

Determination of whether the droplet can cross the flame or not is essential in terms of the prediction of instabilities. If droplets evaporate before entering the reaction zone, purely gaseous phase combustion will occur. However, the presence of droplets in the reaction zone causes different modes of combustion depending on the physical properties of the droplet and gaseous flame, leading to local extinctions on the flame surface and hydrodynamic instabilities. In this scope, passage criterion for the droplet is defined depending on the initial droplet size.

Damköhler number for vaporization, $Da_v$ is defined as the ratio between evaporation characteristic time, $\tau_{ev}$ and preheating time of the flame, $\tau_f$ as [84]:

$$Da_v = \frac{\tau_{ev}}{\tau_f} = \frac{\frac{d_0^2}{K}}{\frac{\delta_L}{S_L}} \tag{4.4}$$

For $Da_v$<1, droplets will completely evaporate inside the flame, while for $Da_v$>1, longer evaporation time will be observed so that the droplets will cross the flame region. In Figure 4.20, computed $Da_v$ for all droplets are shown. It is seen that in the cases considered here, all droplets evaporate in the burnt gas region.

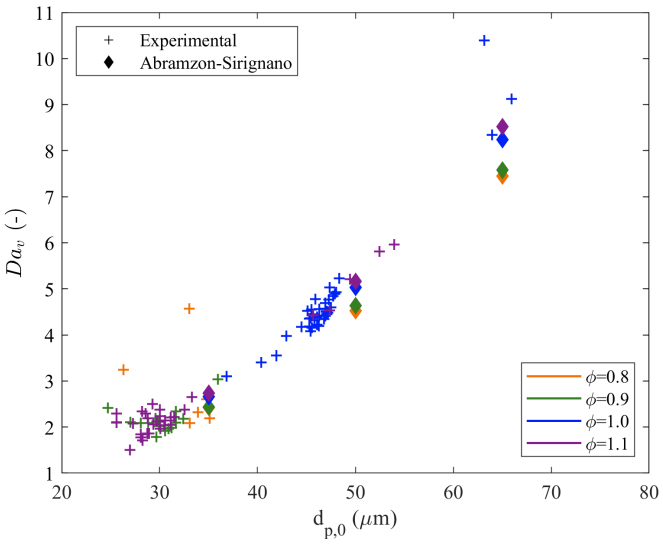


Figure 4.20: Computed $Da_v$ numbers for all droplets.

Accordingly, the critical diameter, $d_{critical}$ to cross the flame region is defined with two approaches. First of all, with the assumption that all the droplets reaching the flame have equal average vaporization constant, $d_{critical}$ can be computed as a function of residence time in the flame [89]:

$$d_{critical,Da_v} = \sqrt{\frac{\bar{K} S_L}{\delta_L}} \tag{4.5}$$

where $\bar{K}$ is the average evaporation constant at the flame condition, $S_L$ is the flamespeed and $\delta_L$ is the thermal flame thickness.

The second approach includes the direct relation of the distance traveled by the droplet from $T$=525 K isotherm to its last position depending on the initial droplet size in all flame conditions, given in Figure 4.21. Since the initial position and velocity may differ for each droplet, a criterion is defined after the droplet enters the flame zone. Extrapolation is performed to determine the critical diameter, $d_{critical,exp.}$ and $d_{critical,num.}$ reported in Table 4.6 such that $\Delta x_{\text{flame cross}}$ equals to zero. Hence, if $d_{p,0} < d_{critical}$, the droplet evaporates before reaching to the reaction zone while for $d_{p,0} > d_{critical}$, the droplet can cross the flame front.

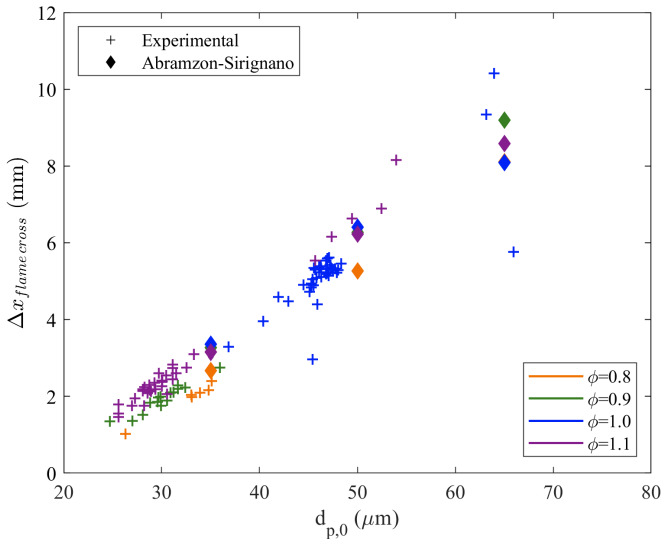


Figure 4.21: The distance that the droplet travels after entering the flame zone ($T$=525 K) for all the droplets.

Table 4.6: Critical diameter values of ethanol droplets to cross the flame zone.

| Condition | $\phi$ | $d_{critical,exp.}$ ($\mu$m) | $d_{critical,num.}$ ($\mu$m) | $d_{critical,Da_v}$ ($\mu$m) |
|---|---|---|---|---|
| SBM-1 | 0.8 | 19.39 | 20.50 | 22.27 |
| SBM-2 | 0.9 | 16.05 | 18.37 | 21.87 |
| SBM-3 | 1.0 | 18.16 | 12.03 | 21.85 |
| SBM-4 | 1.1 | 18.71 | 16.91 | 21.17 |

As it is seen from Table 4.6, the average critical diameter is experimentally found to be 18±1.3 $\mu$m for an ethanol droplet from the direct measurement of distance travelled by the droplet. However, the critical diameter computed from the Abramzon-Sirignano model slightly differs from the experiments. At stoichiometric conditions, it is underestimated by an error of 33 %. This can be explained by the fact that the highest temperature is observed at this condition, leading to a lower lifetime of the droplets. However, it should also be noted that this parameter is not only dependent on the initial diameter but also dependent on the velocity of the droplet and flame thickness which determines the time spent on each isotherm. In order to include the flame parameters, the critical

diameter is also computed from $Da_v$ relation. The calculation with average K, $d_{critical,Da_v}$ overestimates the critical diameter by nearly 2.5 $\mu$m due to the minor differences of $K$ for each droplet, as can be seen from Figure 4.18.

### 4.2.4 Simulations with the Stagnation Burner

#### 4.2.4.1 Numerical Setup of the Stagnation Burner

In order to obtain a more realistic flame structure and its effects on droplet evaporation, simulations are performed with a stagnation burner geometry. The flow domain is shown in Figure 4.22, covering the complete geometry of the burner, the droplet injection tube, and the outlet at the flame zone. As it is discussed in Chapter 3.2.1, an upper stagnation plate is located 25 mm away from the burner outlet to stabilize the flame while $N_2$ co-flow is used to facilitate it. The premixed mixture of air and fuel is fed continuously from the injection tube to carry the ethanol droplet and from the bottom of the chamber. The burner is open to the atmosphere, and gases are released from both sides of the burner.

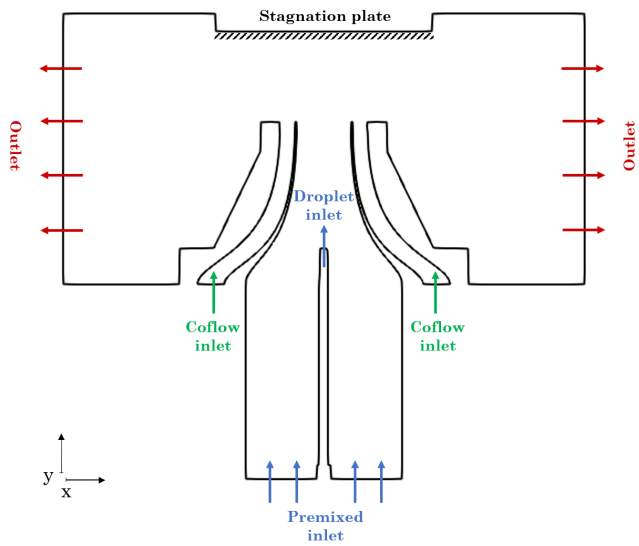


Figure 4.22: Sketch of the computational domain for the 2D stagnation burner.

Four cases are performed in 2D simulations, and the boundary conditions of the corresponding cases are reported in Table 4.7. Two nonreactive cases are performed with different inlet velocities in order to obtain flames at different locations in reactive simulations. Simulations performed with $CH_4$/air mixtures contain $Y_{CH_4}$:0.045, $Y_{O_2}$:0.223, $Y_{N_2}$:0.732 yielding $\phi$=0.8. All cases are performed at ambient conditions, $T$=300 K and $P$=1 atm. The stagnation plate temperature is kept constant at 300 and 500 K for nonreactive and reactive cases, respectively. San Diego mechanism is used for multi-component mixture representation [115].

Table 4.7: Boundary conditions of the 2D stagnation burner simulations at $T$=300 K and $P$=1 atm.

| | MNR-1 | MR-1 | MNR-2 | MR-2 |
|---|---|---|---|---|
| Mixture | $CH_4$/air | $CH_4$/air | $CH_4$/air | $CH_4$/air |
| Reactive | - | ✓ | - | ✓ |
| Equivalence ratio | 0.8 | 0.8 | 0.8 | 0.8 |
| Premixed gas flowrate x$10^3$, $m^3$/s | 7.11 | 7.11 | 8.30 | 8.30 |
| Droplet gas flowrate x$10^4$, $m^3$/s | 4.60 | 4.60 | 5.20 | 5.20 |
| Co-flow gas flowrate x$10^3$, $m^3$/s | 3.13 | 3.13 | 3.58 | 3.58 |
| $T_{plate}$, K | 300 | 500 | 300 | 500 |

Evaporation computations are performed by injecting an isolated ethanol droplet at $T$=300 K without an initial velocity. Similar to previous calculations, 3$^{rd}$ dimensional distance is set to 15 mm along z-direction. The initial droplet diameter is set to 50 $\mu$m diameter first, and the evaporation of the droplet is tracked until complete evaporation via the Abramzon-Sirignano model at MR-1 and MR-2 conditions. Additionally, a larger droplet having 250 $\mu$m initial diameter is injected at MR-1 condition to observe the local temperature change during the evaporation. Changes in droplet parameters, as well as the gas properties, are computed during the evaporation process.

#### 4.2.4.2 Nonreactive Simulations

Isothermal and nonreactive simulations are performed with three different mesh resolutions to observe the effect of the mesh on the computations. 2D triangular meshes M1, M2, and M3 consist of 110k, 200k, and 510k elements, respectively. The flame zone is refined with the largest element size of 500, 200, and 100 $\mu$m for these meshes. The wall mesh resolution is evaluated with dimensionless wall distance, y+, and it is calculated to be less than 2 for all cases in the entire calculation domain. Therefore, the wall is assumed to be resolved. Computations are performed until a steady state solution is obtained at CFL=0.9 corresponding to a time-step of nearly 75 $\mu$s.

The finest computational domain, M3 is represented in Figure 4.23a. The domain contains 510k elements with 100 $\mu$m mesh size at the flame zone. Additionally, burner exit velocity profiles for MNR-1 case computed with different mesh resolutions are given in Figure 4.23b.

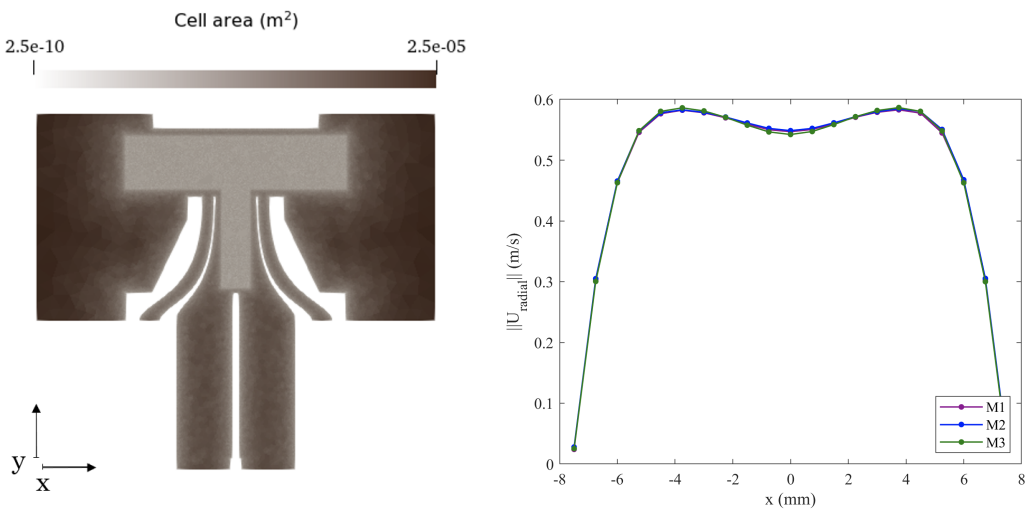


(a) (b)

Figure 4.23: (a) 2D computational domain with M3 (510K elements and 100 $\mu$m grid size at the flame zone) (b) Axial velocity profiles at the burner exit with M1, M2 and M3 meshes for MNR-1.

It is seen that all meshes are refined enough to capture the velocity profile at the burner exit due to the fact that the flow is laminar and thus, steep velocity gradients and fluctuations are not expected. However, at the centerline, the axial velocity is slightly overestimated with coarser meshes. Therefore, M3 will be used in all simulations presented here to resolve the flame field better. Velocity fields of the nonreactive simulations are reported in Figure 4.24. A small recirculation zone attached to the burner wall is observed for higher velocity case at the outer region of $N_2$ co-flow due to flow separation at higher velocities. While larger recirculation zones can be distinguished in both cases, which will provide stabilization of the flame once the mixture is ignited.

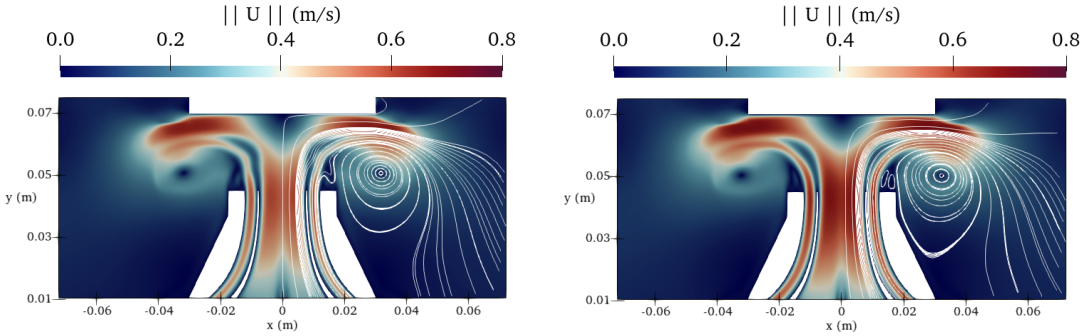


(a) (b)

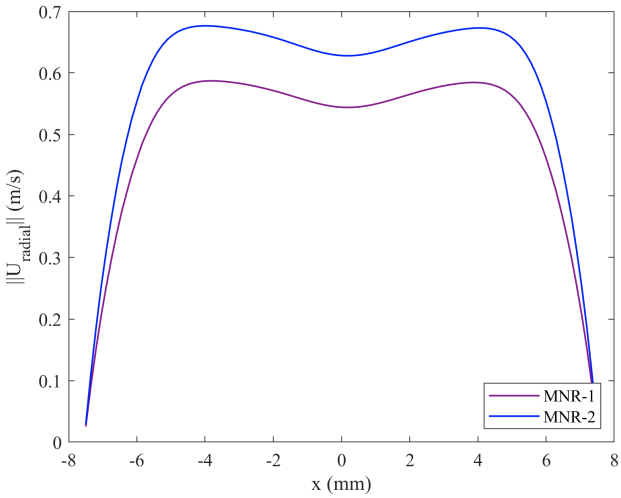


(c)

Figure 4.24: Velocity fields of (a) MNR-1 and (b) MNR-2 (c) Radial velocity profiles at the burner exit.

Burner exit velocity profiles in Figure 4.24 indicate that at the centerline, the velocity of the premixed gases is 0.544 and 0.628 m/s for MNR-1 and MNR-2, respectively.

#### 4.2.4.3 Reactive Simulations

Reactive simulations are performed by introducing an ignition kernel to steady nonreactive cases for 1 s at 2500 K with 50 $\mu$s ramping time. Computations are performed until a stable flame is obtained at CFL=0.7, time-step of nearly 9 $\mu$s. Flame stabilization takes a cumulative physical time of 174 h on 128 processors for MR-1 condition. For MR-2, simulation is initiated from the previously computed flame region at MR-1 condition.

In Figure 4.25, the streamlines and main regions of the flame are reported for stabilized lean methane/air flame at MR-1. The flame zone can be considered as a discontinuity separating the unburnt and burnt stagnation flow fields. The length of these regions depends on burner exit-to-stagnation plate distance and premixed gas velocity. At the unburnt zone, a transition region is observed where the streamlines are diffracted due to the jump in the normal velocity component. For the flame stabilized near the stagnation plate, a free jet region is observed before the transition region with no significant gradient in the velocity, similar to the premixed chamber velocity profile.

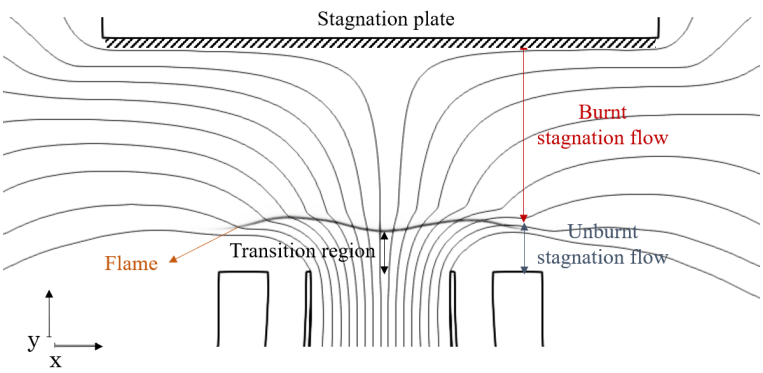


Figure 4.25: Streamlines and regions of stabilized stagnation flame at MR-1.

In Figure 4.26a and Figure 4.26b, steady velocity fields are reported for MR-1 and MR-2 cases, respectively. It is observed that the recirculation zone dissipated towards the bottom of the outer zone due to increased temperature and viscosity at the burnt gas region. Additionally, the velocity of the co-flow affects the position of the recirculation zone and the tail of the flame. Since the flame is near the burner exit ad the velocity profile directly changes to the transition region, the separation zone is not observed.

Figure 4.26c reports the radial velocity profile at the burner exit. The velocities at the center are calculated as 0.41 and 0.48 m/s for MR-1 and MR-2 cases, respectively. This velocity and the curvature of the flame are highly dependent on the gas velocity at the droplet injection tube. In these cases, the difference between premixed gas inlet velocity and droplet injection tube velocity is kept constant at 3 m/s for both cases to eliminate its effect on the flame curvature.

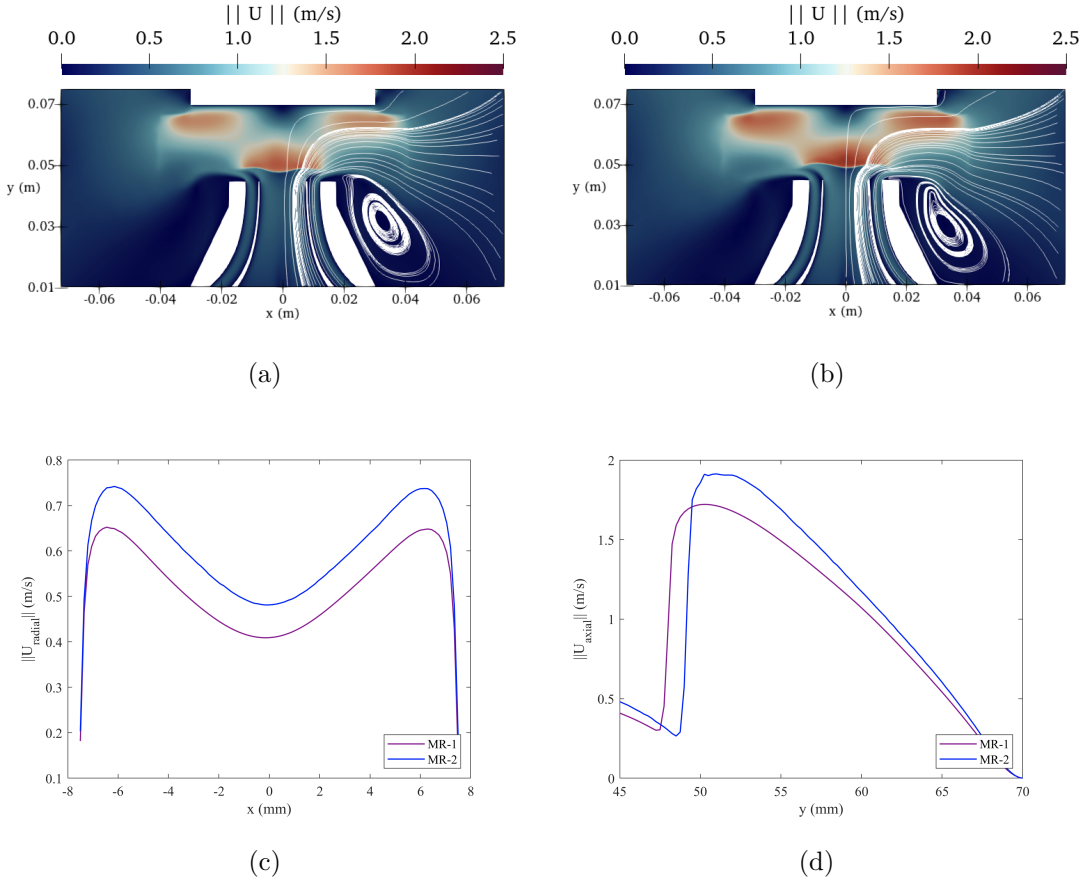


Figure 4.26: Velocity fields of (a) MR-1 and (b) MR-2 (c) Radial velocity profiles at the burner exit and (d) Axial velocity profiles between burner exit and the stagnation plate.

In Figure 4.26d, the axial velocity profiles from the burner exit to the stagnation plate is given. The local minimum of the axial velocity can be considered as the flame speed, $S_L$ as 0.298 and 0.260 m/s for MR-1 and MR-2, respectively. Strain rate, $K_{axial}$ is also calculated from axial velocity profile; $K_{axial} = -dU/dy$ and somputed as 48 and 63 $s^{-1}$.

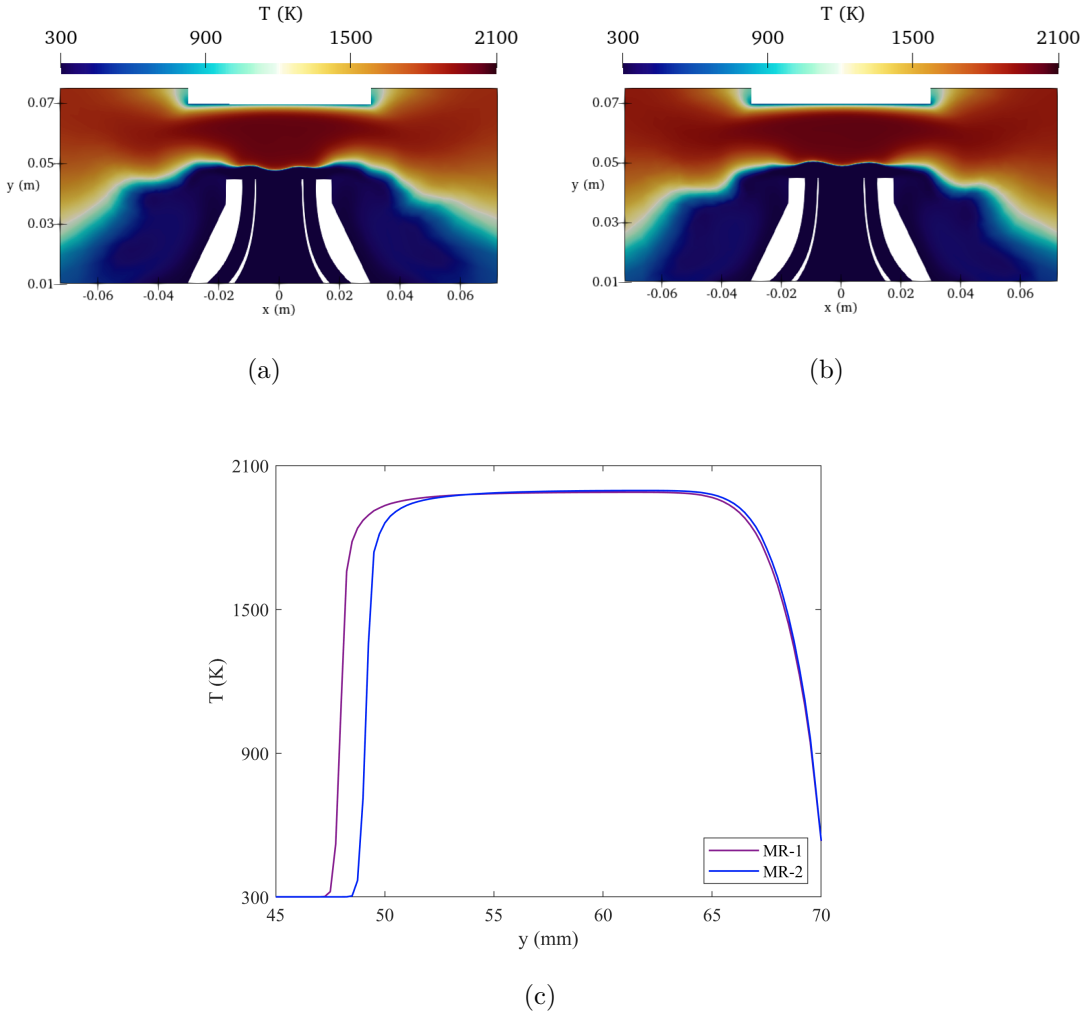


Figure 4.27: Temperature fields of (a) MR-1 and (b) MR-2 (d) Axial temperature profiles between burner exit and the stagnation plate.

Similar temperature fields are observed for MR-1 and MR-2, as can be seen in Figure 4.27. The flame temperatures are calculated as 1988.3 and 1995.5 K for MR-1 and MR-2, respectively. However, as the flame temperature increases with the increase in premixed inlet velocity, the flame thickness decreases from 594.4 $\mu$m to 448.1 $\mu$m.

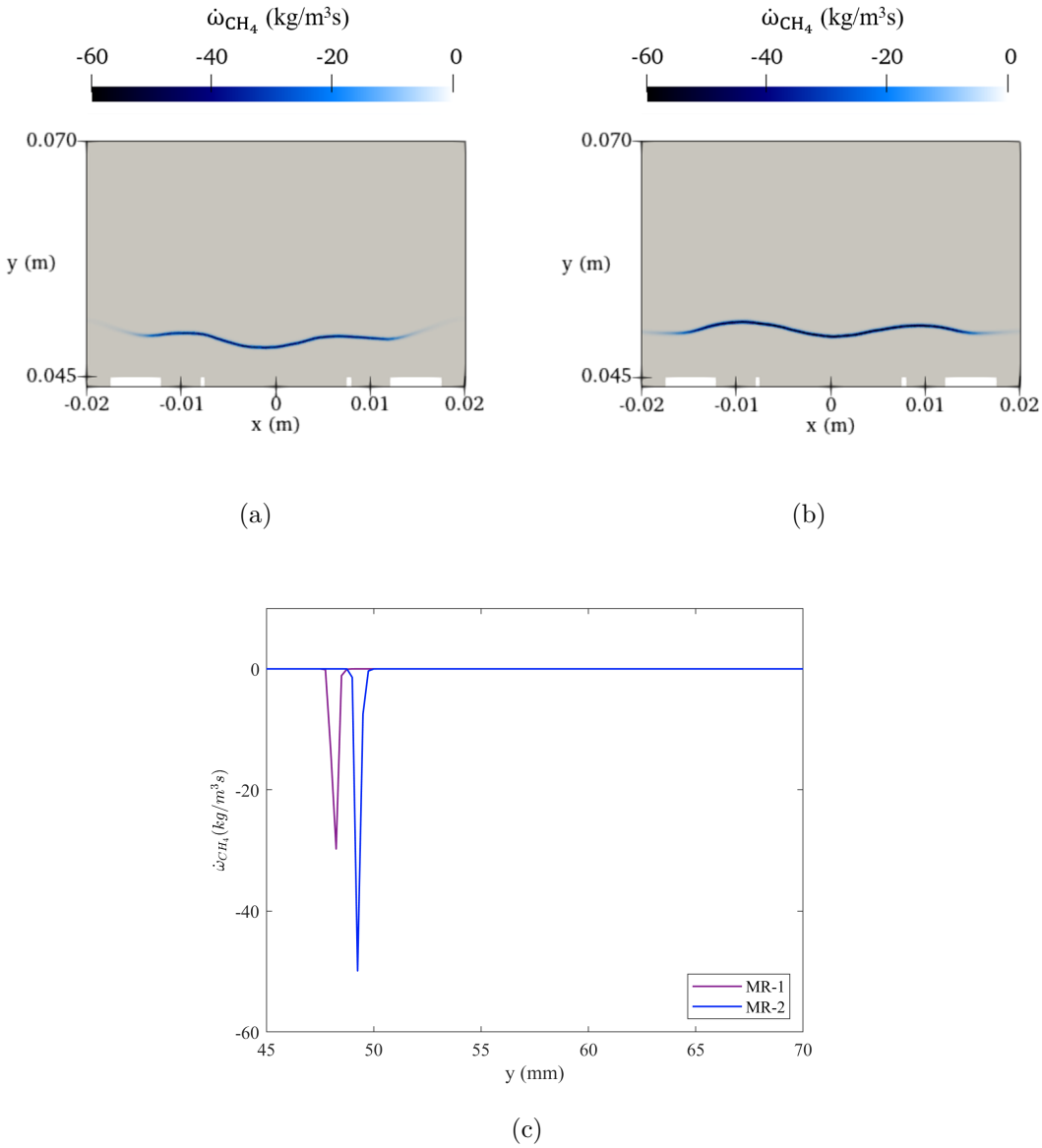


Figure 4.28: Reaction rate fields of (a) MR-1 and (b) MR-2 (c) Axial profiles of $\dot{\omega}_{CH_4}$ between the burner exit and stagnation plate.

Reaction rate profiles in Figure 4.28a and Figure 4.28b show the shape and structure of the flame field, and it is seen that nearly axisymmetrical profiles are achieved. The curvature in the middle part of the flame can be adjusted by the velocity of premixed gases coming from the droplet injection tube. It is then possible to locally alter the stretch, hence the thickness of the flame. As it is seen from reaction rate profiles, as well as the radial burner exit velocity in Figure 4.26d, a similar curvature is obtained for two flame conditions. Nevertheless,

strain rates differ for the performed cases due to the differences in axial velocity profile directly affecting the flame stabilization location. Figure 4.28 shows the axial methane reaction rate profile. Accordingly, $CH_4$/air flame with $U_0$=0.41 m/s at $\phi$=0.8 is stabilized after 3.25 mm from the burner exit under atmospheric conditions within a 25 mm distance, while with $U_0$=0.48 m/s, the stabilization can be achieved after 4.25 mm. Since the flame temperature and the flame thickness will be directly affected, it is foreseen that the vaporization rate will also be affected indirectly by the changes in strain rate and the flame location.

**Evaporation of a Single Droplet**

A single ethanol droplet with an initial diameter of 50 $\mu$m is injected from the droplet injection boundary through the flame field obtained in MR-1 and MR-2 conditions. The change in droplet diameter is tracked via the Abramzon-Sirignano model. Previous calculations indicated that the particle would follow the gas phase, and the slip velocity between the gas and the liquid phases would be insignificant under the present conditions due to the low Stokes number. Therefore, the same conditions will comply with the current calculations. In the light of this, the only effect of flame position and strain rate on the droplet evaporation will be investigated.

Figure 4.29a indicates the spatial variations of diameters of identical droplets under the similar flame conditions. Although a resembling trend is observed for pre-heating and evaporation zones, it is seen that for MR-2, the droplet starts to evaporate later near to a hotter isotherm, around 1700 K. Since the velocity of the gas is higher at MR-2, the velocity of the droplet will also be higher, and the droplet can quickly reach to the flame zone without having enough time for the heat diffusion at lower temperatures. However, the evaporation rate calculated from the slope of Figure 4.29b as in $d^2$-law, is almost identical for MR-1 and MR-2 droplets.

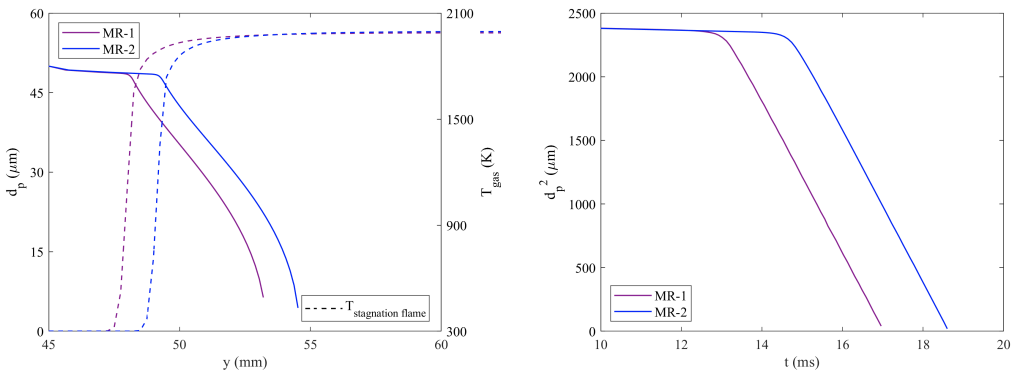


(a) (b)

Figure 4.29: (a) Spatial and (b) temporal evolution of droplet diameter with the Abramzon-Sirignano model at MR-1 and MR-2 ($d_{p,0}$=50 $\mu$m).

Flame characteristics and vaporization properties of the droplet is reported in Table 4.8. Even though the vaporization constant, $K$ is not directly affected by the strain rate, the temperature profile of the flame will be affected. Therefore, the average evaporation temperature is affected nearly by 8 K with a change of flame position. It is also seen that the droplet cannot reach the burnt gases and evaporates inside the reaction zone.

Table 4.8: Comparison of evaporation behavior under different flame characteristics at MR-1 and MR-2 for an isolated ethanol droplet with $d_{p,0}$=50 $\mu$m.

| | MR-1 | MR-2 |
|---|---|---|
| $U_0$, m/s | 0.41 | 0.48 |
| $S_L$, m/s | 0.298 | 0.260 |
| $K_{axial}$, 1/s | 48 | 63 |
| $T_f$, K | 1988.3 | 1995.5 |
| $K$, mm$^2$/s | 0.592 | 0.594 |
| $T_{evap,min}$, K | 1603.9 | 1675.1 |
| $T_{evap,max}$, K | 1975.1 | 1983.6 |
| $T_{evap,average}$, K | 1920.5 | 1934.4 |

In spray applications, there will be structural modifications of the flame zone due to different physical interactions, causing local changes in the curvature, temperature, thickness, and velocity of the flame, etc. The local modifications will have an insignificant effect on the vaporization rate of the droplet, except for the flame temperature. Under the conditions at which $Re_p$ and Stokes number are low, the dominant parameter on the droplet evaporation is always the ambient temperature at laminar conditions.

## 4.3 Conclusions

This chapter focused on the evaporation of an isolated droplet interacting with a laminar and flat flame. Experiments are performed with stagnation burner with $CH_4$/air gaseous flame at $\phi$=0.8-1.1 and the injection of an isolated $C_2H_5OH$ droplet. The diameter change of the droplet is captured via ILIDS, and simultaneously, Mie scattering is utilized to compute the velocity of unburnt gases and droplet via PIV and PTV, respectively. Simulations are performed in the YALES2 solver for stationary droplet evaporation under burnt gases and a moving droplet through 2D stagnation flame fields. The droplet evaporation is computed using Spalding and Abramzon-Sirignano models, respectively.

The main conclusions are:

i. At elevated conditions, the flame temperature is found to have a more dominant effect on the evaporation rate rather than the burnt gas composition.

ii. There is no significant dependency of the evaporation constant to the initial size of the droplet at elevated conditions, as it is expected from the $d^2$-law.

iii. The Abramzon-Sirignano model slightly overestimates the evaporation rate for lean flame conditions while agreeing on the experimental results for stoichiometric and rich conditions.

iv. Evaporation rate can be expressed empirically as an exponential function of flame temperature, flame speed, and flame thickness. Characteristic flame time, $\delta_T/S_L$ has an insignificant effect on the evaporation constant under the performed conditions.

v. The lifetime of the ethanol droplets having $d_{p,0} > 20$ $\mu$m ends after the reaction zone. Therefore, these droplets can cross the flame and possibly cause local modifications by changing the local properties of the flame.

vi. Flame strain rate has a minor effect on the evaporation constant; however, the average evaporation temperature will directly be affected by the flame profile.

# CHAPTER 5

# FLAME SURFACE MODIFICATIONS AND INSTABILITIES

The objective of this chapter is to investigate the structural changes on the flame front due to the passage of a droplet. For this purpose, first, microgravity experiments are performed during the parabolic flights of CNES for aerosol ethanol/air flames via the Schlieren method, and the onset of the instabilities is investigated qualitatively. Secondly, ground experiments are performed in a stagnation burner with propane/air flames and ethanol droplets via chemiluminescence and ILIDS methods. Local extinction phenomenon and propagating wave properties are explored and computed.

## 5.1 Introduction

### 5.1.1 Flame Front Instabilities

Instabilities can be observed in the propagation of a laminar flame front since the gases are subject to strong temperature and concentration gradients. These instabilities can mainly be divided into three categories:

1. *Instabilities due to gravitational forces:* due to the variation in the density of unburnt and burnt gases,
2. *Hydrodynamic instabilities:* due to the expansion of gases when crossing the flame front,
3. *Thermodiffusive instabilities:* due to the thermal and diffusive effects.

While some of the perturbations are resulted in a stabilization, some can create

an imbalance on the flame surface, causing in surface modifications, deformations, or extinctions of the flame front.

#### 5.1.1.1 Instabilities Due to Gravitational Forces

In premixed flames, the flame itself can be considered a thin interface separating two fluids having different densities; unburnt gases with a higher density and burnt gases with a lower density. In the case where the fluid with higher density in the upper part, instabilities may be observed due to the downward gravitational field, represented in Figure 5.1. Especially for very low flamespeed and low combustion rate, these instabilities can appear in the flame zone.

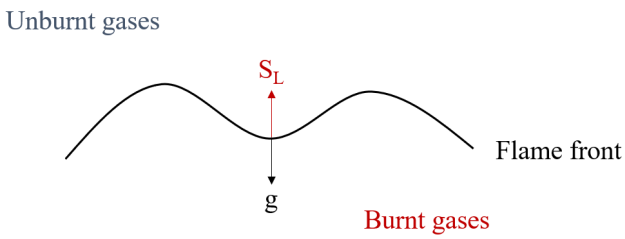


Figure 5.1: A schematic illustration of instabilities due to gravitational forces.

#### 5.1.1.2 Hydrodynamic Instabilities

Hydrodynamic instabilities are first introduced by Darrieus [20], and Landau [46] for an infinitely thin, initially plane flame front. They pointed out that the flame front is inherently unstable due to the different expansion rates of unburnt and burnt gases. This expansion causes a strong acceleration of the gases when crossing the flame front and induces a deviation on the streamlines, as sketched in Figure 5.2. At the convex zone with respect to fresh gases, which are characterized by a positive curvature, streamlines diverge to ensure mass conservation and the fresh gas velocity decreases locally. The opposite case happens at the concave zone, resulting in an increase in the fresh gas velocity. A disturbance thus forms the crease structure, and the flame front is deformed and hence, by nature, becomes unstable.

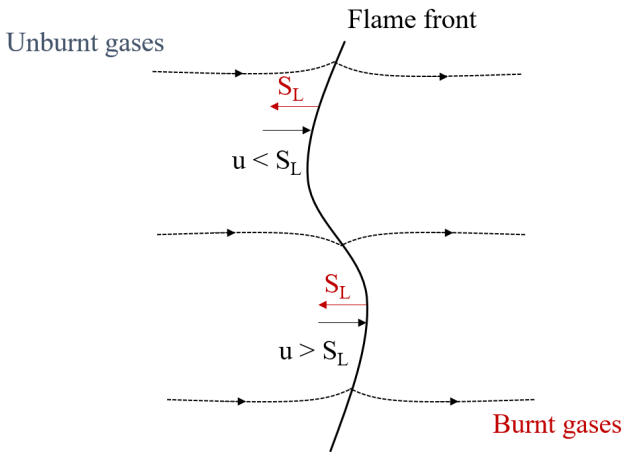


Figure 5.2: A schematic illustration of hydrodynamic instabilities.

When a planar flame is subjected to a weak perturbation, it will react to this disturbance leading to an increase or decrease in the initial amplitude of the perturbation. In order to investigate the flame response to such perturbations, the hydrodynamic model was first introduced by Darriues [20] and Landau [46]. In this approach, the flame is considered as an infinitesimally thin interface, propagating at a constant speed, $S_L$ and separating the unburnt and burnt gases. Accordingly, the linear stability of a planar flame can be computed from the following relation [56]:

$$\omega = S_L k \omega_{DL}, \quad \text{with} \quad \omega_{DL} = \frac{-\sigma + \sqrt{\sigma^3 + \sigma^2 - \sigma}}{\sigma + 1} \tag{5.1}$$

where $\omega$ is the growth rate, $k$ is the wave number and $\sigma = \rho_u/\rho_b$ is the thermal expansion parameter. The given relation between the growth rate and wave number is called the dispersion relation. Since $\sigma > 1$ at combustion applications, $\omega$ will always be higher than 0, implying that the premixed flames being unconditionally unstable due to the hydrodynamic effects. However, this conclusion is not valid for the wavelengths which are comparable to the flame thickness due to the fact that the fluctuations on the flame surface will be equalized by the diffusion inside the preheating zone, leading to no observation of instability. Additionally, since $\omega$ is proportional to $k$, the perturbations with a shorter wavelength will grow faster than the ones with a long wavelength. However, Darrieus and Landau model neglects the transport properties, curvature, and diffusion

effects. Dispersion relation can be extended to include the gravitational effects as [56]:

$$\omega = \frac{-\sigma + \sqrt{(\sigma^3 + \sigma^2 - \sigma) - (\sigma^2 - 1)\,(g/S_L^2 k)}}{\sigma + 1} S_L k \tag{5.2}$$

where $g$ is the gravitational acceleration and $S_L$ is the flame speed. If the wavelength is larger than $\lambda = 2\pi\sigma S_L^2/g$, the perturbation will be damped out by gravitational forces for a planar flame. Perturbations with a short wavelength, however, will remain hydrodynamically unstable.

#### 5.1.1.3 Thermodiffusive Instabilities

Thermodiffusive instabilities occur due to the imbalance of heat diffusion towards the fresh gases and molecular diffusion towards the reaction zone. They are, moreover, co-linear with the local gradients of temperature and concentration, therefore perpendicular to the flame front. Lewis number, $Le$ characterizes the relation between these phenomena:

$$Le = \frac{D_{th}}{D_m} \tag{5.3}$$

where $D_m$ is the molecular diffusivity and $D_{th}$ is the thermal diffusivity:

$$D_{th} = \frac{\lambda_u}{\rho_u C_{p,u}} \tag{5.4}$$

where $\lambda_u$, $\rho_u$ and $C_{p,u}$ are the thermal conductivity, density and heat capacity of unburnt gases, respectively.

Effective Lewis number, $Le_{eff}$ can also be defined to eliminate the discontinuity at the stoichiometry. Bechtold and Matalon proposes $Le_{eff}$ as [5]:

$$Le_{eff} = 1 + \frac{(Le_E - 1) + (Le_D - 1)A}{1 + A}, \quad \text{with} \quad A = 1 + Ze(\Phi - 1) \tag{5.5}$$

where $\Phi$=$\phi$ for fuel-rich flames and $\Phi$=$1/\phi$ for fuel-lean flames. $Le_E$ and $Le_D$ are the Lewis number for excess and deficient reactants, respectively. $Ze$ is the Zeldovich number defined as:

$$Ze = \frac{E_a(T_b - T_u)}{R{T_b}^2} \tag{5.6}$$

where $T_b$ and $T_u$ are the burnt and unburnt gas temperature, respectively. Activation energy, $E_a$ can be computed by diluting the mixture with a small amount of inert gas [6, 113], in this case replacing $N_2$ in the air with Ar up to 0.3 % in terms of mass fraction, from the relation [77]:

$$E_a = -2R \left( \frac{d[ln(\rho_u S_L^0)]}{d({T_b}^{-1})} \right)_{P,T,\phi} \tag{5.7}$$

Three cases can be defined based on the Lewis number, represented in Figure 5.3:

1. For $Le$>1, molecular diffusivity is less than thermal diffusivity, resulting in stabilizing effects due to the local decrease in flame speed, thus, decreasing the amplitude of the disturbance for the convex zone. For the concave zone, the flame accelerates locally, and the heat flux is predominant in the mass dispersion, reducing the amplitude of the disturbance.

2. For $Le$<1, molecular diffusivity is higher than thermal diffusivity, resulting in destabilizing effects by locally accelerating the flame and thus increasing the amplitude of the disturbance for a convex zone. For a concave zone, the flame is decelerated due to the diffusion of reactants over a wide area while amplifying the disturbance.

3. For $Le$=1, the structure of the flame front is not affected by the thermodiffusive properties.

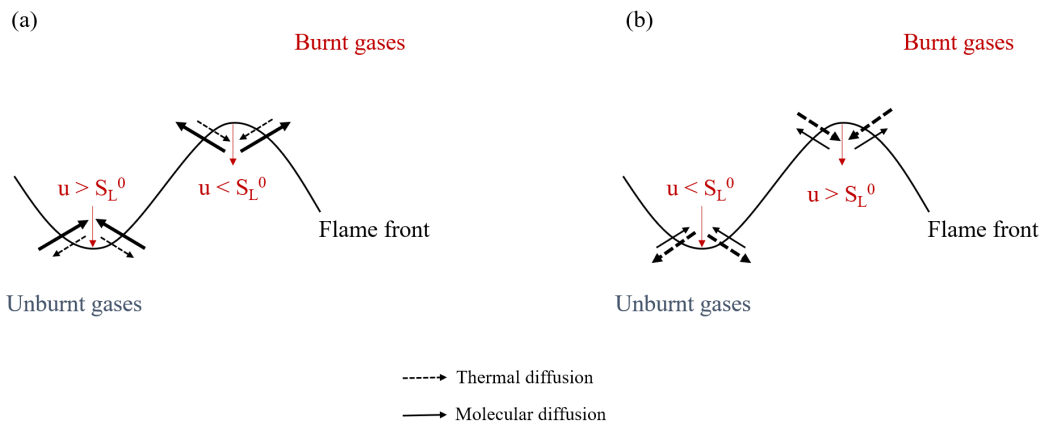


Figure 5.3: A schematic illustration of thermodiffusive instabilities (a) $Le$<1, destabilizing effect (b) $Le$>1, stabilizing effect.

The effect of diffusion on the Darrius-Landau model for planar flames is introduced by Pelce et al. and Matalon et al. [75, 57]:

$$\omega = S_L k \omega_{DL} - S_L l_f \left[B_1 + Ze(Le_{eff} - 1)B_2 + PrB_3\right] k^2 \tag{5.8}$$

where $Pr$ is Prandtl number, $Ze$ is Zeldovich number, $l_f = D_{th}/S_L$ is the diffusion length, $B_1$,$B_2$ and $B_3$ are positive coefficients depending on $\sigma$:

$$B_1 = \frac{1}{4}\frac{\sigma^3 - \sigma + 2\sigma^2(2\omega_{DL} + \sigma + 1)}{\sigma + (\sigma + 1)\omega_{DL}} \tag{5.9}$$

$$B_2 = \frac{1}{2}\frac{\sigma(\sigma - 1)(\omega_{DL} + 1)(\omega_{DL} - \sigma)}{\sigma + (\sigma + 1)\omega_{DL}} \tag{5.10}$$

$$B_3 = \frac{1}{2}\frac{\sigma(\sigma - 1)^2}{\sigma + (\sigma + 1)\omega_{DL}} \tag{5.11}$$

The terms on the right-hand side in Equation 5.8 with $B$ coefficients correspond to thermal, molecular, and viscous diffusion, respectively. Thermal diffusion always has a stabilizing effect by smoothing out the temperature difference, as well as the viscous diffusion due to the large difference in viscosity at the flame. The molecular diffusion effect, however, depends on the mixture composition or effective Lewis number. $Le_{eff}$ must exceed a critical value to ensure the stabilization of short wavelengths. For high $Le_{eff}$ values, the hydrodynamic instability is enhanced by the diffusive effects.

### 5.1.2 Structural Changes on Flame Front

Many experimental, theoretical, and numerical studies have been conducted to characterize the effects of droplets on a gaseous flame structure at different configurations. One of these configurations includes the presence of mono-dispersed droplet clouds. Burgoyne and Cohen conducted the first study on mono-dispersed liquid aerosol flame with tetralin having 7-55 $\mu$m droplet size [14]. They concluded that for the droplets larger than 10 $\mu$m, brush-like flame structure was observed. Mizutani and Nakjima reported that the presence of small kerosene droplets increased the burning velocity of propane more for lean flames than rich flames [61]. Hayashi and Kumagai used Wilson cloud chamber method [123] to generate mono-sized droplets in a stagnant mixture [38, 39]. They created ethanol droplets with nearly 7 and 20 $\mu$m mean droplet sizes and reported that under microgravity, cellular flames were observed at rich conditions for sufficiently large diameters. At the same time, the burning velocity increased under lean conditions. Atzler and co-workers also studied possible mechanisms of flame instabilities for iso-octane aerosol flames [3]. Their findings resulted in the observation of cellular instabilities with an increase in flame surface area and burning rate due to the change in local equivalence ratio. Lawes et al. reported similar observations under microgravity conditions for iso-octane droplets [50]. Bradley et al. also observed flame surface wrinkling resulted in Darrieus–Landau and thermodiffusive instabilities due to the presence of large alcohol droplets, which may enter the reaction zone and significantly increase the fuel mass flux [11]. Thimothée et al. demonstrated that the gaseous ethanol-air flame is totally stable and smooth, as well as the aerosol flame with ethanol droplets fully vaporized in pre-heating zone [110]. They also suggested possible mechanisms leading to the instabilities, including the heat sink phenomena due to the heat taken by the droplet for vaporization from flame field using water droplets as an inert medium [111] while correlating the topology of instabilities with the evaporation characteristics at different conditions under microgravity [112]. Renoux and co-workers extended the investigation under similar conditions by reporting a stability envelope for rich ethanol aerosol flames [83]. Spray-induced instabilities were reported resulting from the perturbations on flame front via surface

area increase due to droplet passage.

Orain and Hardalupas also studied the monodispersed ethanol injected into premixed natural gas stagnation flame [71]. The change in local equivalence ratio is found to depend on the initial droplet size. Mercier and co-workers conducted another study on an isolated acetone droplet and its interaction with methane flame via PLIF [59]. In Figure 5.4, the passage of non-reacting and reacting acetone droplet through methane/air flame is shown. It is reported in their study that the velocity of the droplet has a major impact on the reactivity of the droplet and local flame extinction. They reported that the reactivity of the flame front is reduced, as observed in Figure 5.4a, by the droplet, most likely due to the low vapor temperature generated from the evaporation of the droplet.

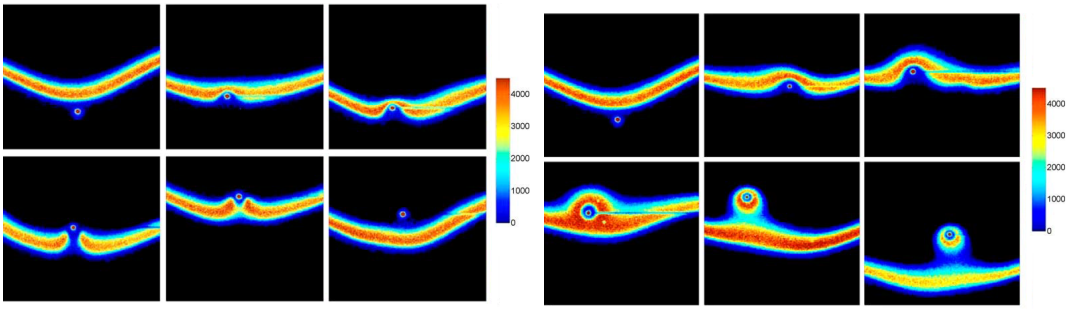


(a) (b)

Figure 5.4: OH PLIF of the passage of an acetone droplet (200 $\mu$m) through methane/air diffusion flame (a) Droplet with higher $u_p$ (without ignition) (b) Droplet with lower $u_p$ (ignition) [59].

#### 5.1.2.1 Local Extinction Phenomenon

Many studies mentioned earlier focused on the effect of liquid droplets on flame propagation speed and morphology experimentally. In order to foresee the initiation of the change in flame parameters and structure, heat sink and local extinction phenomena are studied by many researchers for the interaction of a droplet and flame. Greenberg and co-workers theoretically predicted the onset of instabilities due to the heat loss from the flame zone for the evaporation of

droplets via linear stability analysis [29, 30]. They reported that for richer conditions, droplets cause an increase in surface area and burning velocity while creating a heat sink, resulting in cellular structures [32]. They also developed an approach to understanding how the amount of liquid fuel and the latent heat of vaporization affect the onset of instabilities causing flame extinction [31]. Han and co-workers also theoretically studied the sensitivity of spherical flame propagation and ignition to the finite rate of evaporation [36, 37]. They concluded that for rich conditions, the flame structure is affected by droplet evaporation only by the heat absorbed, while for lean conditions, local equivalence ratio change also has an impact. Recently, Li et al. reported the effects of heat loss from the flame to droplet for evaporation and Lewis number on laminar planar flame propagation under droplet mists [52]. It was observed that for highly evaporative droplets, the flame propagation speed is decreased due to the heat sink on the flame zone [53]. Finally, numerical studies are performed by Nicoli and co-workers by performing DNS simulations of flame propagation in the presence of water droplets [68] and compared with microgravity experiments [113]. For larger droplet inter-distance, they reported the quenching in the flame zone due to the presence of water droplets leading to the observation of Darrieus-Landau instabilities.

## 5.2 Results and Discussions

In the previous studies, evidences on cellular instabilities caused by the presence of droplets are reported under microgravity conditions for aerosol ethanol flames via several optical diagnostics [66, 110, 111, 112, 109, 113, 83, 82]. However, there are very few experimental studies examining the effects of the single droplet on the flame instabilities. In this part of the study, the similarities between the aerosol flame and gaseous flame with a single droplet is investigated to understand the local extinction phenomenon resulting in flame instabilities. First, a qualitative analysis is performed for Schlieren images obtained in a zero-g environment at previously performed conditions, reported by Renoux and co-workers [83], for spherically-expanding rich aerosol ethanol/air flames. Then, from the

observation of the formation of local sinks and holes at the beginning of the cellular structures, the evidence of the local extinction phenomena is investigated for rich propane/air gaseous stagnation flames at ground conditions with an isolated ethanol droplet injection via chemiluminescence and ILIDS methods. Finally, the behavior of a propagating wave on the flame surface due to the passage of a droplet is investigated under rich flame conditions.

### 5.2.1 Interactions of a Spherically Expanding Flame With Aerosol

In order to observe the effect of droplets on the propagation of a spherically expanding flame, pure gaseous and aerosol rich ethanol/air flames are created at the same condition. In Figure 5.5, instantaneous captures for different flames at $\phi$=1.2 are given.

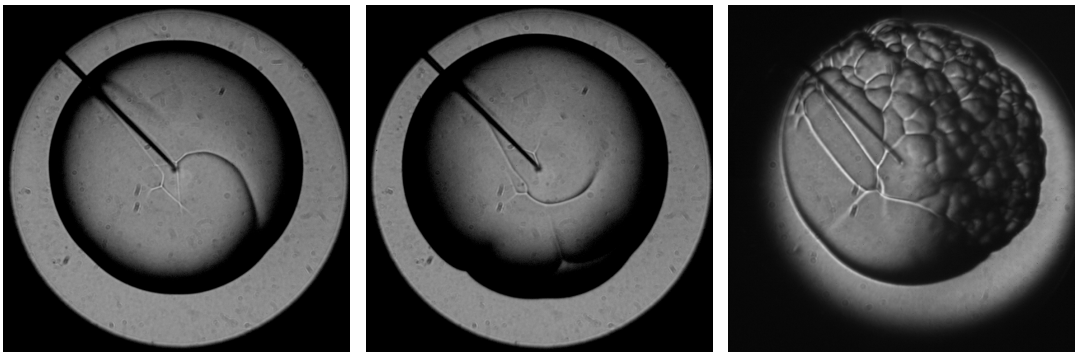

(a) (b) (c)

Figure 5.5: Schlieren images of equivalent flames at AC-1 (a) Gaseous flame at ground conditions (6.2 ms after ignition) (b) Two-phase flame at ground conditions (6.4 ms after ignition) (c) Aerosol flame under microgravity (10.8 ms after ignition).

The first image, Figure 5.5a, shows purely gaseous ethanol/air flame under terrestrial conditions where a smooth and noncorrugated flame structure is observed. It should be noted that a large crack is formed due to the instantaneous electric load from the electrodes. The flame condition having the same equivalence ratio and initial pressure is created with aerosol, given in Figure 5.5b, by decreasing the chamber pressure and creating liquid fuels inside the chamber.

Large cellularities are observed at the lower part of the flame due to the presence of liquid fuel. However, although the droplets are created everywhere inside the chamber via the Wilson technique, they are coalesced and sedimented to the bottom of the chamber thanks to gravity, making it impossible to observe the interaction of the droplets and propagating flame. Therefore, the experiments are performed under microgravity conditions to prevent the droplets from sedimentation, given in Figure 5.5c. The presence of cellularities proves the formation of ethanol droplets that are expecting to be mono-dispersed and homogeneously distributed at zero-g. For all experimental conditions performed in this study, the same behavior is observed under terrestrial and microgravity conditions; hence, ethanol/air aerosol flame is observed to be intrinsically unstable.

Renoux et al. performed the same experimental conditions, given in Table 3.1, with Mie scattering to determine the droplet position and inter-distance, with ILIDS to compute the droplet size and with shadowgraphy and chemiluminescence to observe the flame morphology [83]. In the current study, the morphology of the flame is determined via the Schlieren method. In Figure 5.6, the comparison between shadowgraphy, chemiluminescence, and Schlieren images at $\phi$=1.2 is given. From these images, it can be interpreted that aerosol creation is successfully achieved, and droplets are observed inside the combustion chamber without settling under the zero-g environment. While during the experiments of Renoux and co-workers (Figure 5.6a, 5.6b), homogeneous distribution of the droplets is observed, Schlieren image indicates that most of the droplets are near the top right corner of the chamber. This can be explained due to the movement of the plane, hence the movement of the droplets towards this side. Still, cellular structures can easily be observed under the reported conditions for qualitative interpretations.

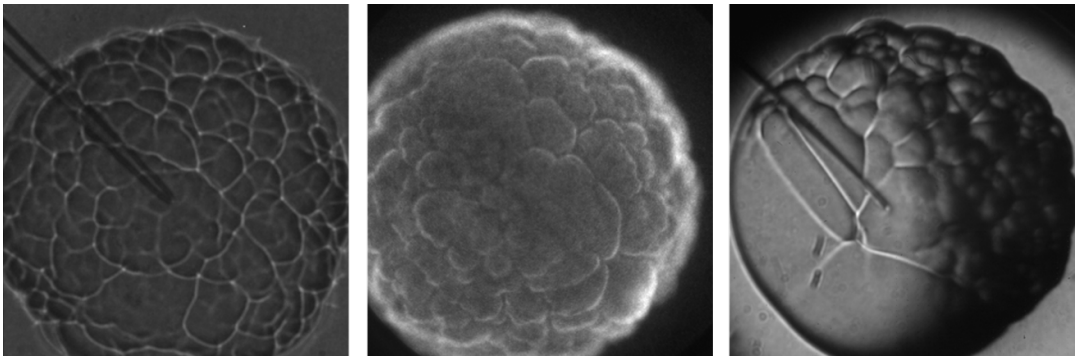

(a) (b) (c)

Figure 5.6: Comparison of (a) shadowgraphy [83], (b) CH* chemiluminescence [83] and (c) Schlieren images of equivalent flames and at a radius of 13.5 mm (aerosol ethanol/air flame at AC-1).

It is clearly seen that shadowgraphy provides the clearest images for cell size detection. Renoux and co-workers reported the cell size distribution and stability envelope based on these images [83]. However, as it is seen in Figure 5.6c, cell sizes are hard to detect with Schlieren methods due to the sensitivity of pinhole to the changes in gravitational acceleration during parabolic flight, resulting in shadows and darkness with a fixed position at the certain zones of the combustion chamber. Nevertheless, the Schlieren method provides additional information for the initiation of these cells, as it is the measurement of the first derivative of the flame field. In Figure 5.7, snapshots of the propagating flame can be seen in time for the condition of AC-1.

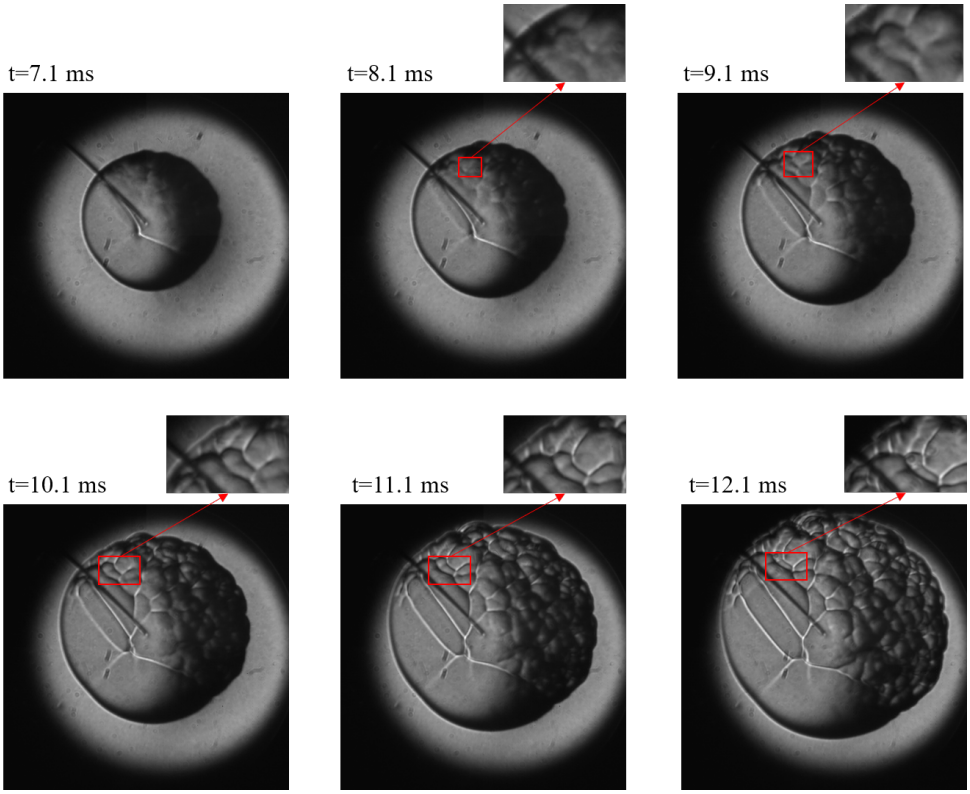


Figure 5.7: Formation of instabilities on the flame surface due to the presence of droplets (aerosol ethanol/air flame at AC-1).

By focusing the wrinkles, first, the dark spots are observed, as in $t$=8.1 ms, indicating the loss of signal in the density gradient of the flame. Then, the extension of the flame surface can be seen as a lighter zone corresponding to cellular cell formation. The dark spots and signal loss at the initiation of instabilities can be interpreted as the local hole structures due to the passage of liquid droplets and quenching in the flame zone, leading to the formation of the edges of cells. The same mechanism is observed for all performed conditions.

As it is pointed out in Renoux and co-worker's results [83], the droplets only act as a trigger on the development of the instabilities due to the fact that the wavenumbers related to droplet inter-distance are higher than the mode wavenumbers. These instabilities then, may lead to intrinsic instabilities on gaseous flame, which is observed for ethanol/air aerosol flames under the performed conditions. Therefore, it can be interpreted that the droplets act as obstacles that absorb heat from the flame zone for evaporation and cause ex-

tinction on the flame surface by changing the flame properties locally.

### 5.2.2 Interactions of Stagnation Flame with an Isolated Droplet

In the light of microgravity experiments, ground experiments are designed to analyze the effect of a single droplet on the flame morphology. To simplify the physics and understand the local extinction phenomenon deeply, the stagnation flame configuration with a single isolated droplet injection is found to be very suitable. Due to its high luminosity, these experiments are performed with propane/air gaseous mixture. Moreover, the Lewis number is slightly higher than the unity for rich propane/air flames, which tend to be prone to cellularities induced both by hydrodynamic and thermodiffusive instabilities. This can also be explained that rich propane flames are not stabilized thermodiffusively, as it is observed with cellular structure formation at similar conditions [111]. Therefore, these flames are chosen to be good candidates in terms of sensitivity to droplet passage.

#### 5.2.2.1 Computation of Flame Characteristics

Similar to the previous methane/air flames, laminar flame computations are performed with Cantera [28] in order to determine the flame characteristics at the performed experimental conditions, given in Table 3.3. Accordingly, the 1D stagnation flame field is computed using the San Diego mechanism with multi-species transport [115]. While the plate temperature is kept constant at 500 K for all flame conditions, the inlet velocity of the unburnt gases, $U_0$ is computed based on the mass flow rates fed to the system.

Computed flame speeds, $S_L$ and flame temperatures, $T_f$ are given in Table 5.1 for all experimental conditions.

Table 5.1: Parameters of 1D stagnation $C_3H_8$/air flame computed with the San Diego mechanism [115] ($T_{plate}$=500 K).

| Condition | $\phi$ | $U_0$ (m/s) | $S_L$ (m/s) | $T_f$ (m/s) | $\delta_L$ ($\mu$m) | $Le_{eff}$ |
|---|---|---|---|---|---|---|
| SBP-1 | 1.0 | 1.101 | 0.449 | 2246.1 | 391 | 1.44 |
| SBP-2 | 1.1 | 1.115 | 0.448 | 2253.6 | 389 | 1.31 |
| SBP-3 | 1.2 | 1.100 | 0.412 | 2190.8 | 404 | 1.24 |
| SBP-4 | 1.3 | 1.095 | 0.341 | 2115.6 | 461 | 1.18 |
| SBP-5 | 1.4 | 1.109 | 0.261 | 2030.0 | 604 | 1.14 |

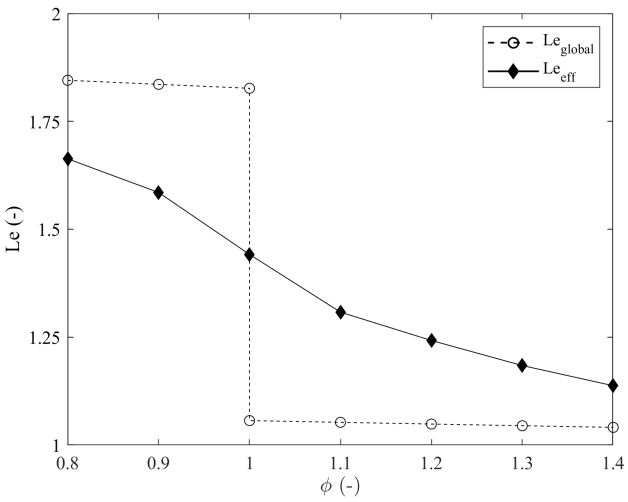


Figure 5.8: Variation in global and effective Lewis numbers for propane/air flame at 300 K and 1 atm.

When propane and methane flames are compared, it is seen that the flame temperature is higher by nearly 30 K for propane/air flames while the flame is thinner. Also, the effective Lewis number of propane deviates from 1 for leaner flames as it is given in Figure 5.8; however, Le number for methane/air flames is very close to unity. Additionally, the higher luminosity of propane/air flame provides good performance on chemiluminescence with a less noisy signal.

#### 5.2.2.2 Variation in Gaseous Phase Properties

Firstly, investigation for the local changes in the gaseous phase is conducted with previously reported $CH_4$/air flame simulations. From 2D stagnation flame field simulations, variations in gas phase properties are investigated while the droplet is evaporating through the flame field. The focus is made here on the stoichiometric case and initial droplet diameter of 50 $\mu$m. All plots for other cases are reported in Appendix A.

Figure 5.9b shows the variation in ethanol mass fraction, $Y_{C_2H_5OH}$ and reaction source term, $\dot{\omega}_{C_2H_5OH}$ within 1.2 mm distance along the x-axis which is parallel to the flame, while it is moving perpendicular to flame in the y direction. Y coordinates are normalized by the flame thickness so that the comparison can be performed for all conditions. It should also be mentioned that $y$=0 indicates the flame position, while $x$=0 denotes the centerline of the domain where the ethanol droplet is injected.

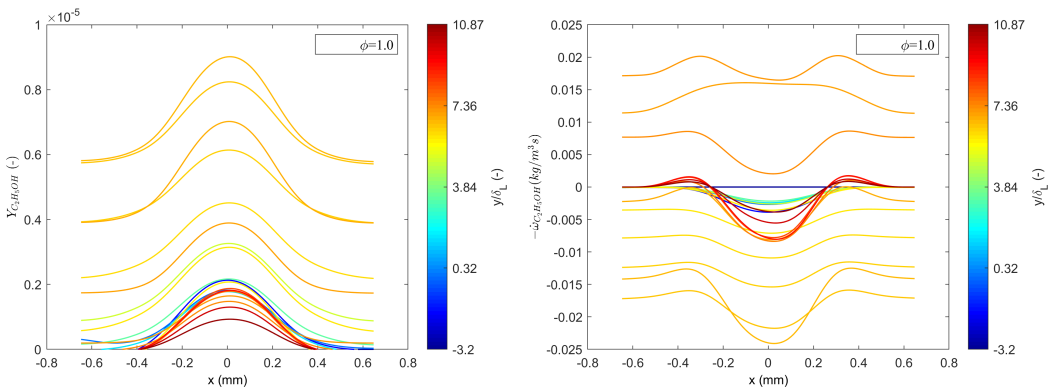


(a) (b)

Figure 5.9: Variation in (a) $C_2H_5OH$ mass fraction and (b) $C_2H_5OH$ reaction source term on the isoline of droplet along $x$-axis through the flame at SBM-3.

The mass evolution of ethanol in the gas phase can be interpreted from Figure 5.9a. It is seen that the rate of ethanol build-up in the gas phase increases up to almost 2.8 mm away from the flame, and then, it decreases, although the lifetime of the droplet continues to decline. This trend can also be observed

from the mass evaporation rate in Figure 4.17c. As the droplet closes to the maximum temperature isoline in the gas phase, the surface temperature of the droplet continues to increase. Once the temperature of the droplet becomes constant, the evaporation rate decreases after almost 8 ms at the same distance away from the flame for $\phi$=0.9, 1.0, and 1.1. However, for $\phi$=0.8, a nearly 2 ms delay is observed at 2.1 mm away from the flame due to the fact that more time is needed for the droplet to reach its boiling temperature at the lowest flame temperature, which is 1991.4 K. Although the velocity of gases differ at each flame condition, the major effect on gas build-up comes from the flame temperature due to low Stokes number at the performed conditions.

In order to observe the local changes in the reaction zone, the variation of $Y_{C_2H_5OH}$ and $\dot{\omega}_{C_2H_5OH}$ in time on the isoline of the maximum $\dot{\omega}_{CH_4}$ indicating the flame position, is given in Figure 5.10.

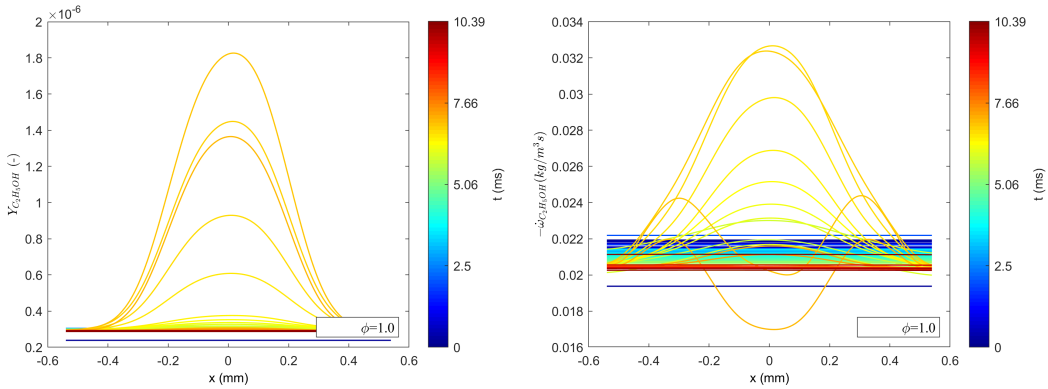


(a) (b)

Figure 5.10: Variation in (a) $C_2H_5OH$ mass fraction and (b) $C_2H_5OH$ reaction source term at the flame over time at SBM-3.

The prominent increase of ethanol amount in the gas phase is observed between 6-7.5 ms at the flame zone, and then ethanol is consumed. The highest amount of ethanol build-up at the flame is observed for the leanest and richest cases, as is seen from Figure A.2. It can be related to the residence time of the droplet by compensating the velocity of the droplet and the flame thickness. Moreover, evaporated ethanol diffuses nearly to 800 $\mu$m region on the flame surface, and it

increases with the equivalence ratio. Additionally, the droplet takes heat from the flame by decreasing the local temperature nearly by 5 K, as can be seen in Figure A.1, expecting to observe a local sink on the flame zone.

When the ethanol droplet is vaporized, total fuel concentration increases locally in the flame region. For order of magnitude fuel amount comparison, mass fractions of $C_2H_5OH$ and $CH_4$ are plotted at the centerline of the domain along the droplet path on $y$ direction, given in Figure 5.11. The mass fraction of ethanol is multiplied by $10^4$ to be able to make a comparison with methane.

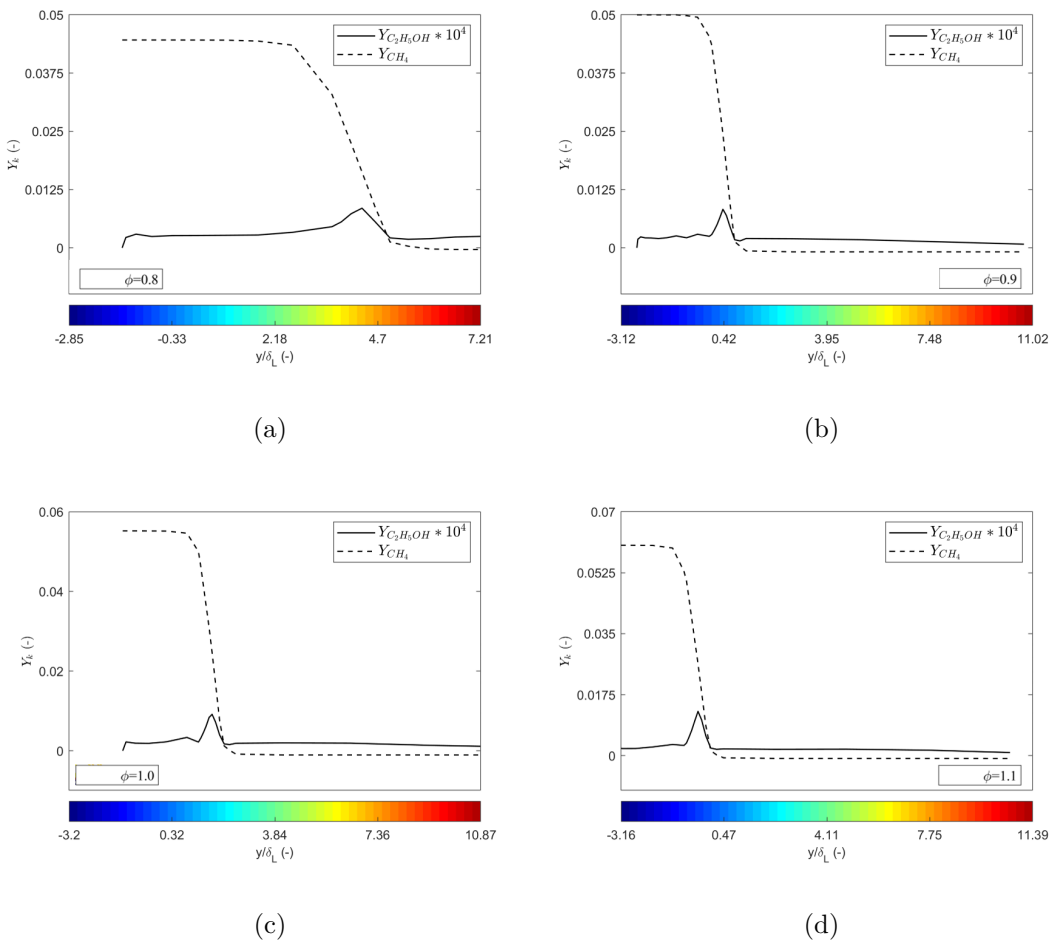


Figure 5.11: Variation in $C_2H_5OH$ and $CH_4$ mass fractions at the centerline of the domain through the flame.

For equal size droplets at different flame conditions, the evaporation rate slightly differs due to the variation of flame temperature, given in Figure 4.19, which leads to a hardly noticeable difference in gaseous ethanol amount, especially when it is compared with the amount of methane. However, individual comparison gives rise to the reactivity of ethanol in the flame zone. In order to investigate the reactivity of the droplet, reaction source terms of $C_2H_5OH$ and $CH_4$ are plotted through the droplet path and given in Figure 5.12.

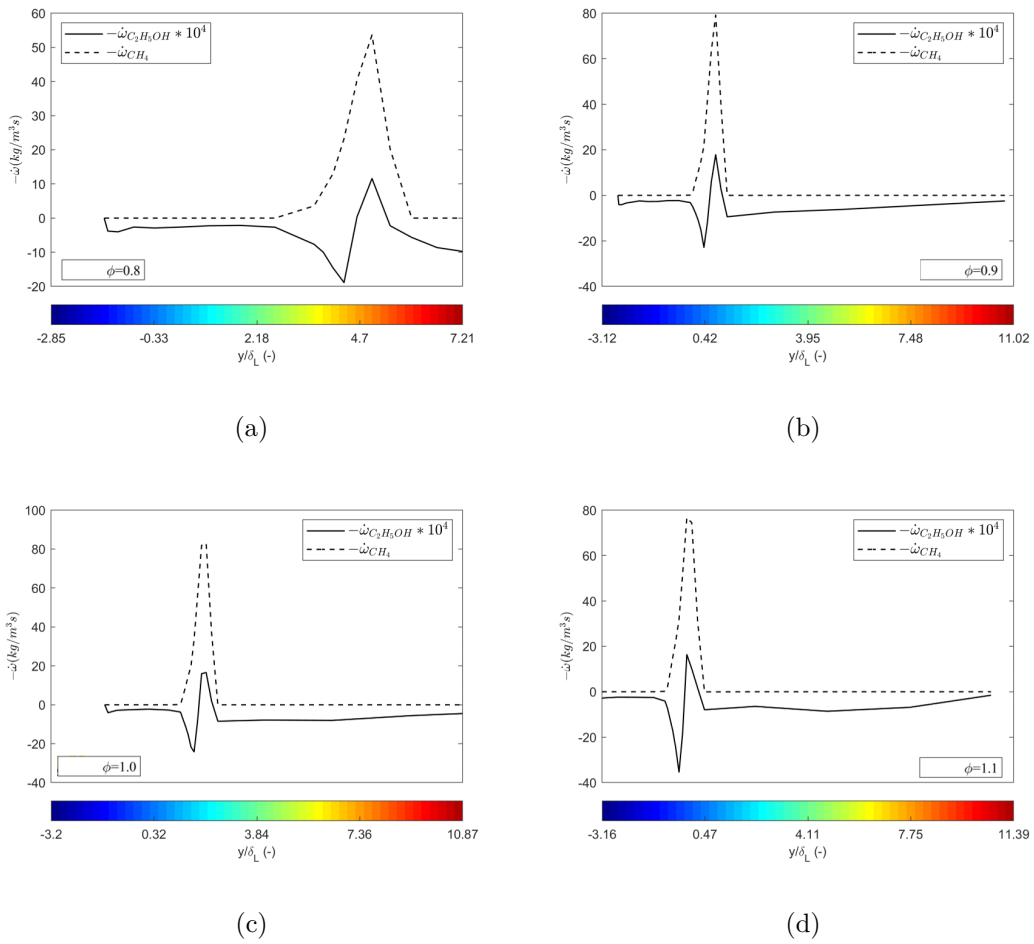


Figure 5.12: Variation in $C_2H_5OH$ and $CH_4$ reaction source terms at the centerline of the domain through the flame.

From the area under positive and negative peaks of ethanol, it can be concluded from Figure 5.12 that all gaseous ethanol is consumed in the reaction zone, except for the richest case due to the deficiency of excess oxygen at the ambient. Since the gaseous ethanol build-up is high in this case, the expansion of gases is

expected to create an extinction on the flame. It should also be mentioned that the mass fractions and source terms of methane and oxygen are not affected noticeably due to the passage of the ethanol droplet since the mass provided to the gaseous phase is nearly negligible when it is compared to gaseous fuel, methane.

Figure 5.13 reports the variations in the axial temperature profile from the burner simulations in the presence of an ethanol droplet having an initial size of 50 and 250 $\mu$m. It is seen that the effect of a small-sized droplet cannot be captured at the performed conditions, while 250 $\mu$m droplet decreases the local temperature by nearly 30 K and shifts the temperature profile. Evidently, large droplets cause the local loss of reactivity by taking heat from the flame. Additionally, vapor build-up inside the flame region may cause local sink on the flame surface.

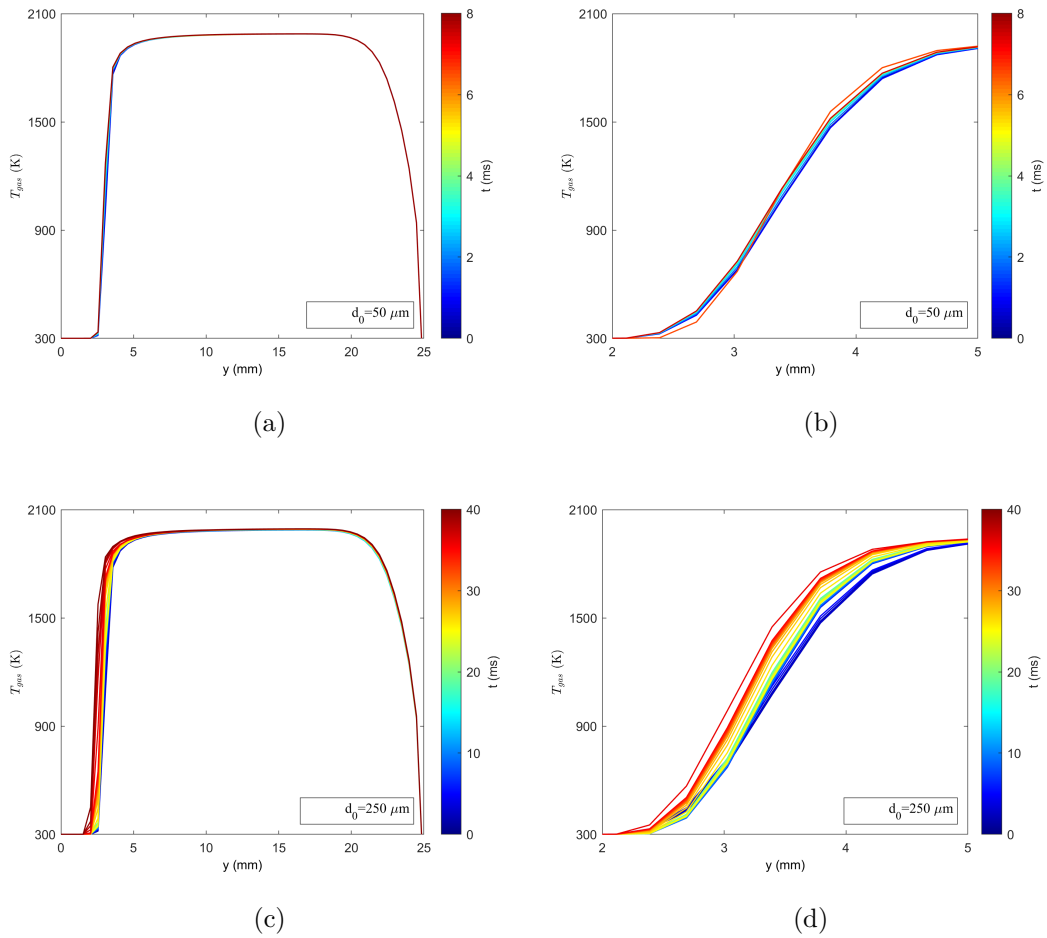


Figure 5.13: Variation in temperature profile from the burner exit to the stagnation plate while the ethanol droplet having (a,b) $d_{p,0}$=50 $\mu$m and (c,d) $d_{p,0}$=250 $\mu$m is passing through the flame at MR-1.

#### 5.2.2.3 Flame Surface Extinction

The evaporation of an isolated ethanol droplet is investigated previously under premixed methane/air flame conditions, and it is found that a single droplet having a diameter less than 20 $\mu$m evaporates inside the flame region, leading to a nearly gaseous flame structure. In order to understand the onset and initiation of instabilities, an isolated droplet having about 50 $\mu$m diameter is injected through the stagnation flame so that the droplet can pass through the flame field, and its effects on the flame structure can properly be observed under the determined conditions, reported in Table 3.3. It is worth mentioning that

the amount of premixed gas fed from the droplet injection tube is increased to create a flame surface with a little bump in order to increase the possibility of capturing the decrease in signal at the droplet injection point. It is done due to the fact that the camera captures the signal from the flame as a line integral of signals. Hence, if the signal is distributed over a wider area, it will be easier to distinguish any change in a specific region. Since the curvature is negligible, the flame surface will still be treated as flat.

First, the decrease in collected signal from the flame surface when the droplet passes is computed. In order to achieve this, the summation of pixel values inside a specified region is calculated with two different approaches; with a constant position region of interest, given in Figure 5.14 and with an adaptive region of interest along with the flame position, shown in Figure 5.15 for $\phi$=1.4 with $d_{p,0}$=48.5 $\mu$m. The vertical distance of ROI is selected as a function of flame thickness with the multiplication of 2, 1, and 0.5, while the horizontal distance is selected as a function of initial droplet diameter depending on previously reported diffused gas distance on the flame as almost 16 times of $d_{p,0}$. Although the decrease in the signal can be detected with both approaches, it is hard to distinguish from the former one due to the fact the flame is oscillating during the experiment. Therefore, the adaptive approach is more suitable for capturing the percentage signal loss during the droplet passage since the baseline can be drawn to the flame position. For the adaptive ROI calculations, the total signal amount is normalized so that the comparison can be performed for all cases.

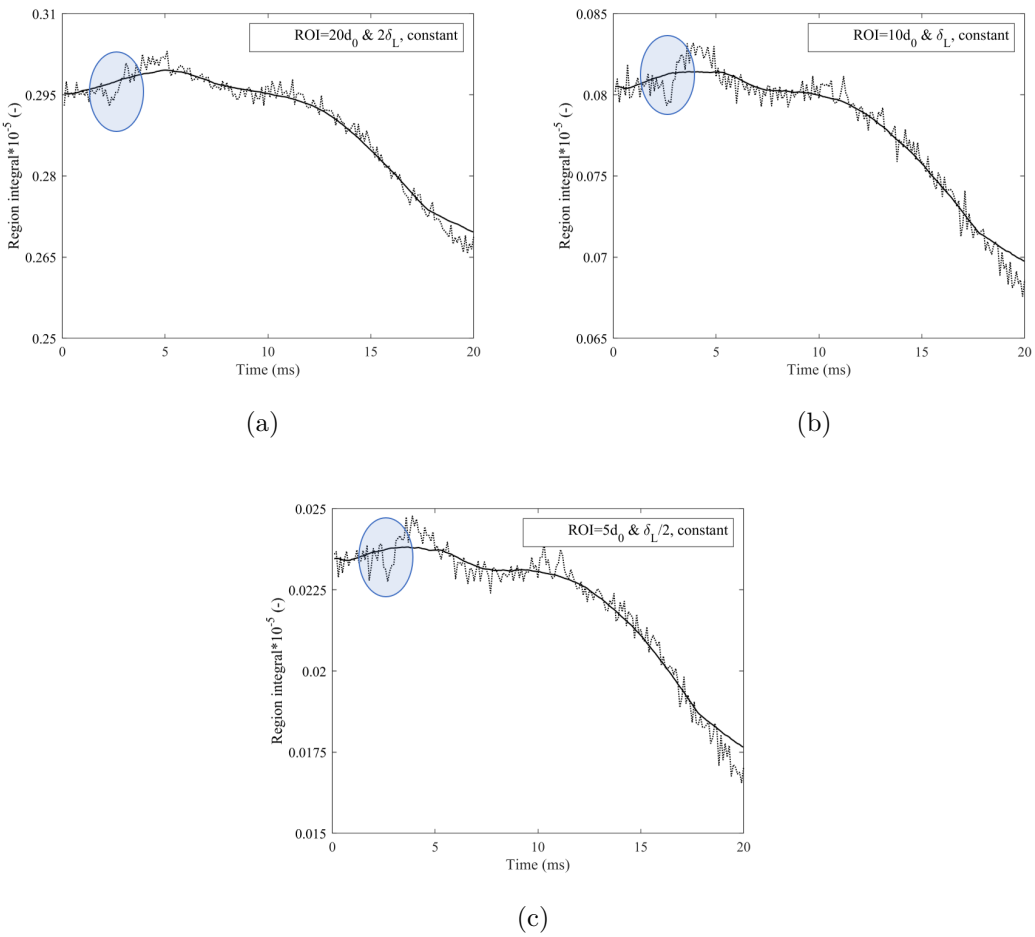


Figure 5.14: Variation in integral of signal on time due to droplet passage ($d_{p,0}$=48.5 $\mu$m) at SBP-5 with constant position ROI.

As it can be seen from Figure 5.15, the decrease in signal is observed between 2 to 6.6 ms, and the flame is recovered after the droplet passage. The decrease in the signal can directly be related to the droplet-flame interaction, where the droplet losses its mass due to evaporation. Since the fuel-rich cases do not contain excess oxygen in the flame zone, the droplet will not be oxidized. Hence, as the droplet takes heat from the flame, the luminosity and reactivity of the flame will decrease. For the droplet having 48.5 $\mu$m initial diameter, this time takes 1.7 ms. The recovery time takes almost 4.9 ms, which also depends on flame properties, as well as the droplet's initial diameter and evaporation constant. The normalized signal values indicate 12 %, 13.2 %, and 15 % signal loss during the droplet passage for the corresponding region of interest dimensions. For the

smallest ROI, postprocessing needs to be more accurate on the first detection of droplet passage so that the interaction point needs to be in the middle of the rectangle. Since the signal loss is very high compared to leaner cases, it can easily be determined for $\phi$=1.4, which has the highest luminosity among the reported cases.

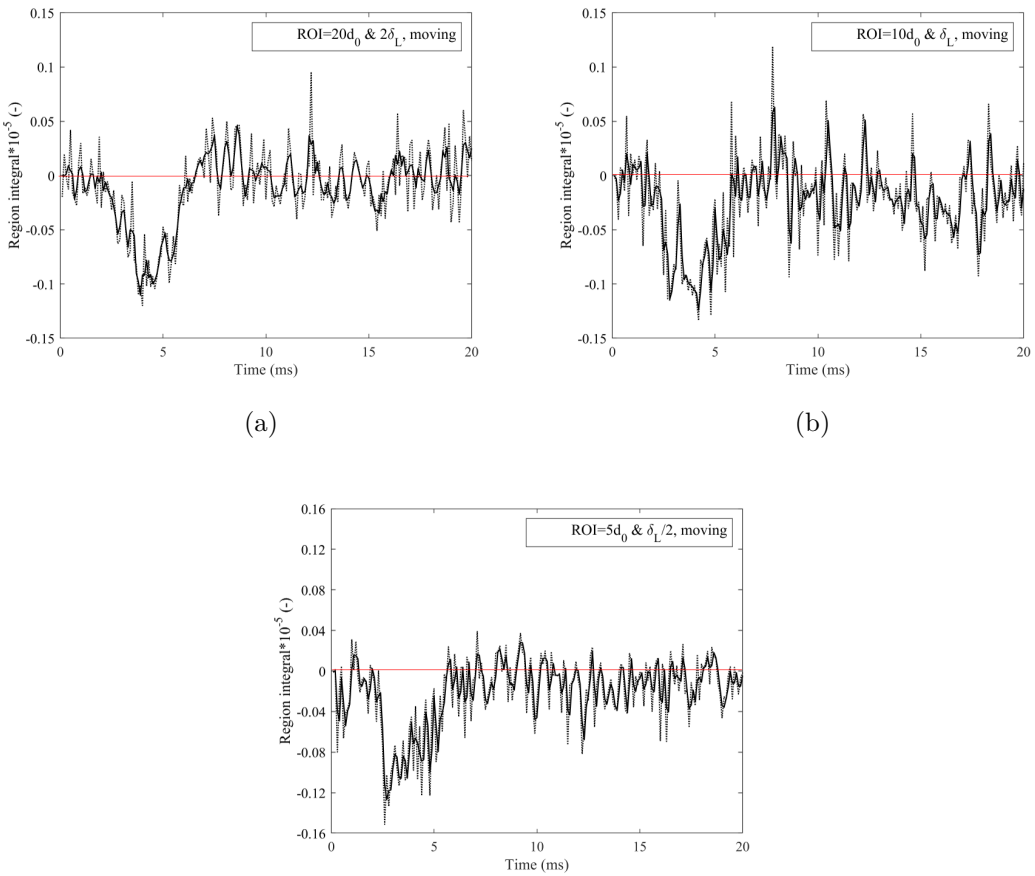


Figure 5.15: Variation in integral of signal on time due to droplet passage ($d_{p,0}$=48.5 $\mu$m) at SBP-5 with moving ROI.

Similar conclusions can be drawn for $\phi$=1.3, as seen in Figure 5.16 and Figure 5.17, where the average 10.71 % signal loss is detected between 2.2-5.5 ms. The recovery time for the flame, nearly 1.9 ms, is less than the richest case because when the flame condition is closer to stoichiometry, the flame is less prone to disturbances. Although the initial droplet diameter is slightly higher in SBP-4 than SBP-5, heat loss duration differs by 0.3 ms due to the increase in flame

temperature, hence, quicker evaporation.

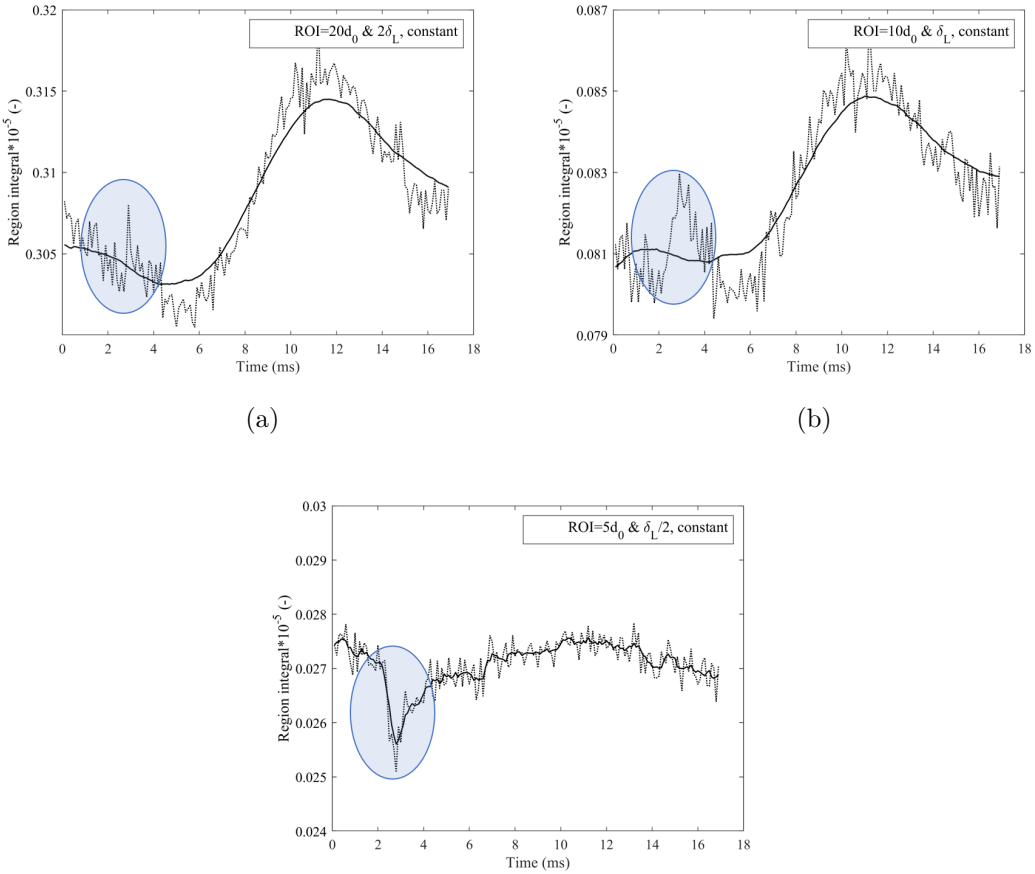


Figure 5.16: Variation in integral of signal on time due to droplet passage ($d_{p,0}$=51.9 $\mu$m) at SBP-4 with constant position ROI.

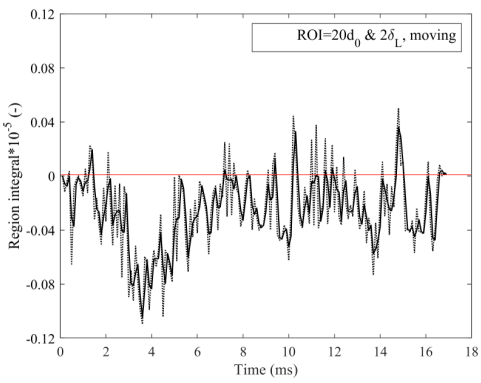


(a)

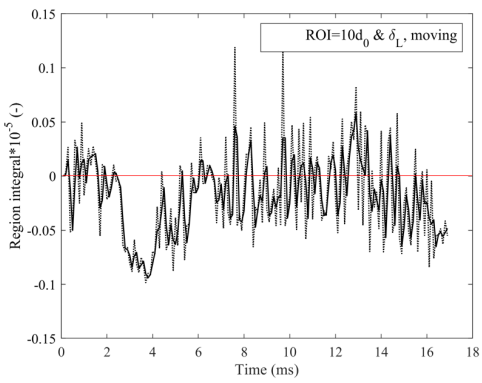


(b)

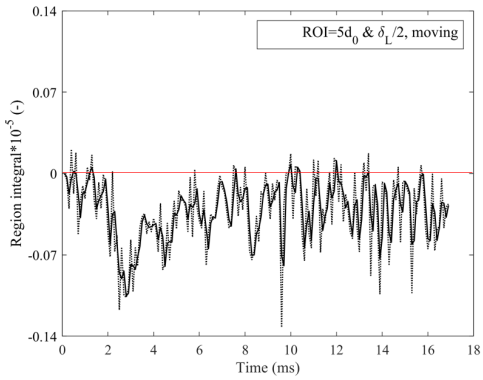


(c)

Figure 5.17: Variation in integral of signal on time due to droplet passage ($d_{p,0}$=51.9 $\mu$m) at SBP-4 with moving ROI.

At $\phi$=1.2, the detection for signal loss can only be captured with the large ROIs as 5.1 % on average during 3.6 ms, as given in Figure 5.18 and Figure 5.19. The recovery time after extinction is calculated as 2.9 ms while the droplet crossing time is 0.7 ms, even though it is the largest droplet injected. The flame temperature for this case is nearly 75 K higher than $\phi$=1.3 so the droplet will evaporate more inside the preheating and reaction zones. As a result, gaseous ethanol will build up near to flame region, leading to more time to recover the flame itself.

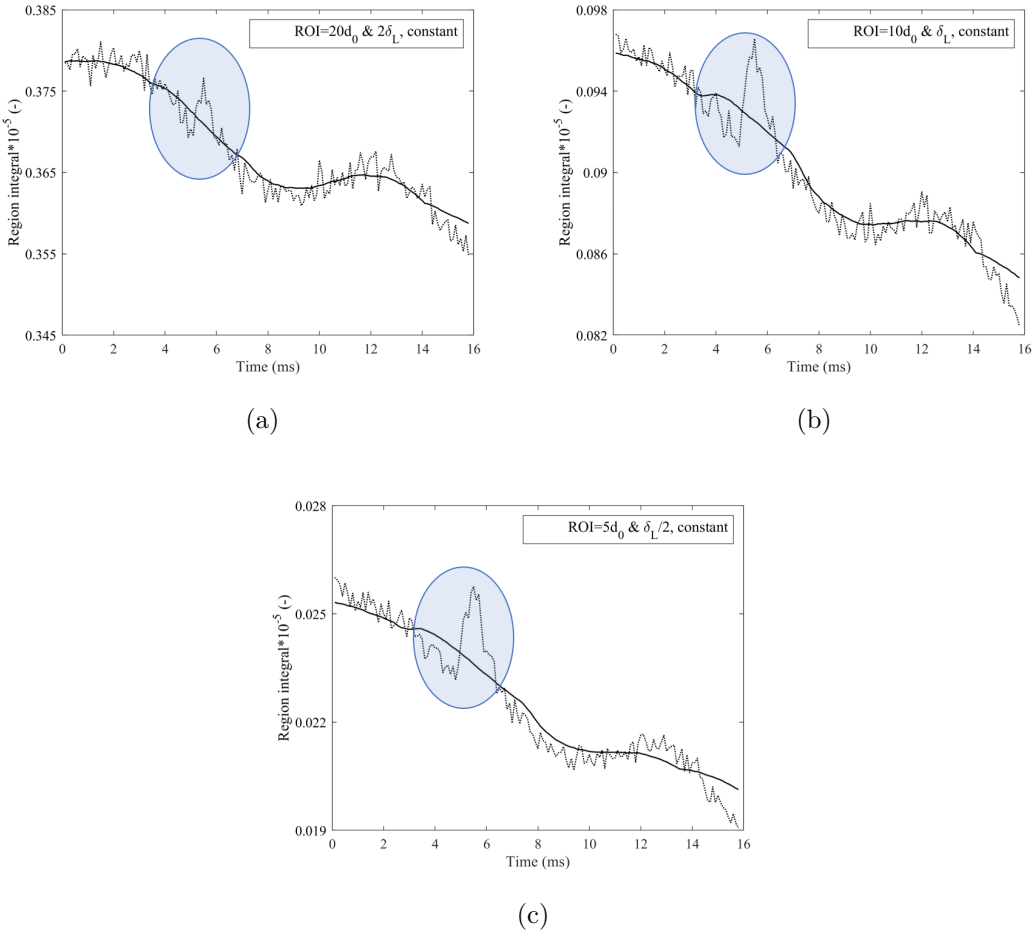


Figure 5.18: Variation in integral of signal on time due to droplet passage ($d_{p,0}$=58.9 $\mu$m) at SBP-3 with constant position ROI.

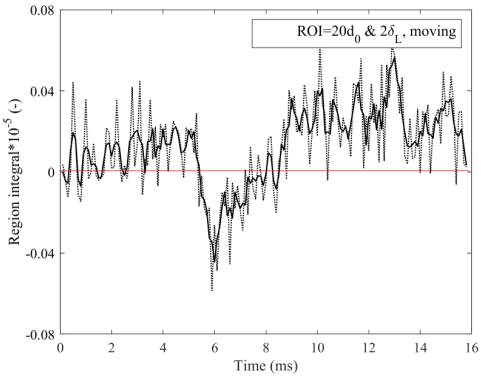


(a)

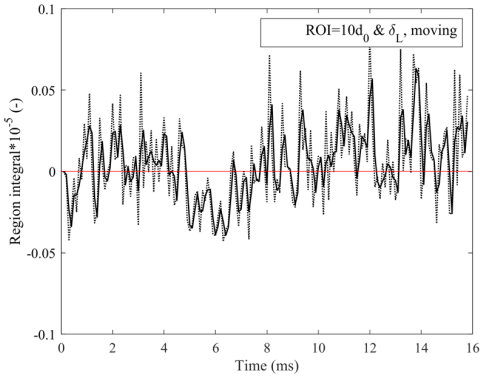


(b)

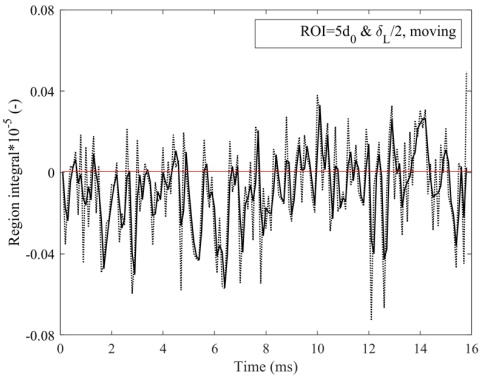


(c)

Figure 5.19: Variation in integral of signal on time due to droplet passage ($d_{p,0}$=58.9 $\mu$m) at SBP-3 with moving ROI.

In Figure 5.20 and Figure 5.21, total signal inside ROI is given for $\phi$=1.1. As can be seen clearly, it is almost impossible to detect signal loss with an adaptive ROI. However, from global computations, 1.8 % signal loss can be reported for 0.5 ms. It is hard to distinguish the signal with a smaller region of interest for near-to-stoichiometric cases. The first reason is that the luminosity of the flame will decrease when it becomes leaner. Secondly, leaner flames will be more stable, and they will be less sensitive to any changes.

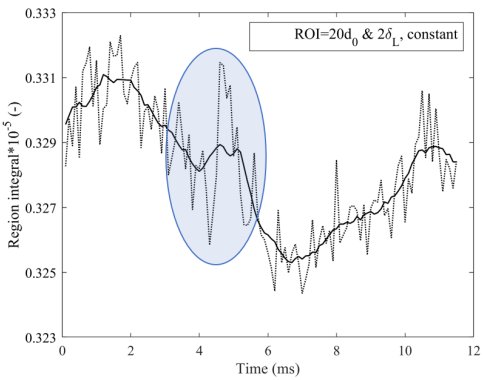


(a)

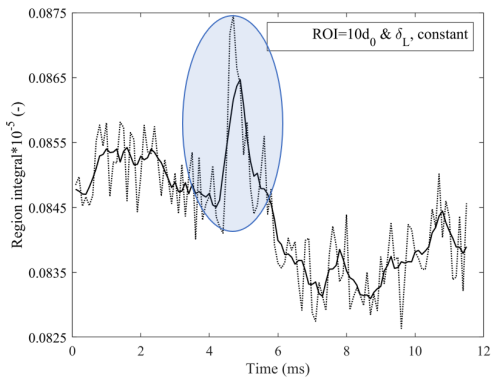


(b)

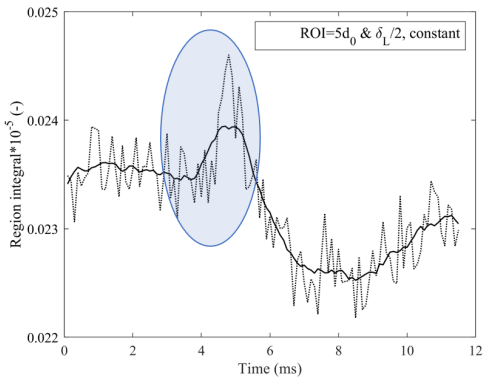


(c)

Figure 5.20: Variation in integral of signal on time due to droplet passage ($d_{p,0}$=55.4 $\mu$m) at SBP-2 with constant position ROI.

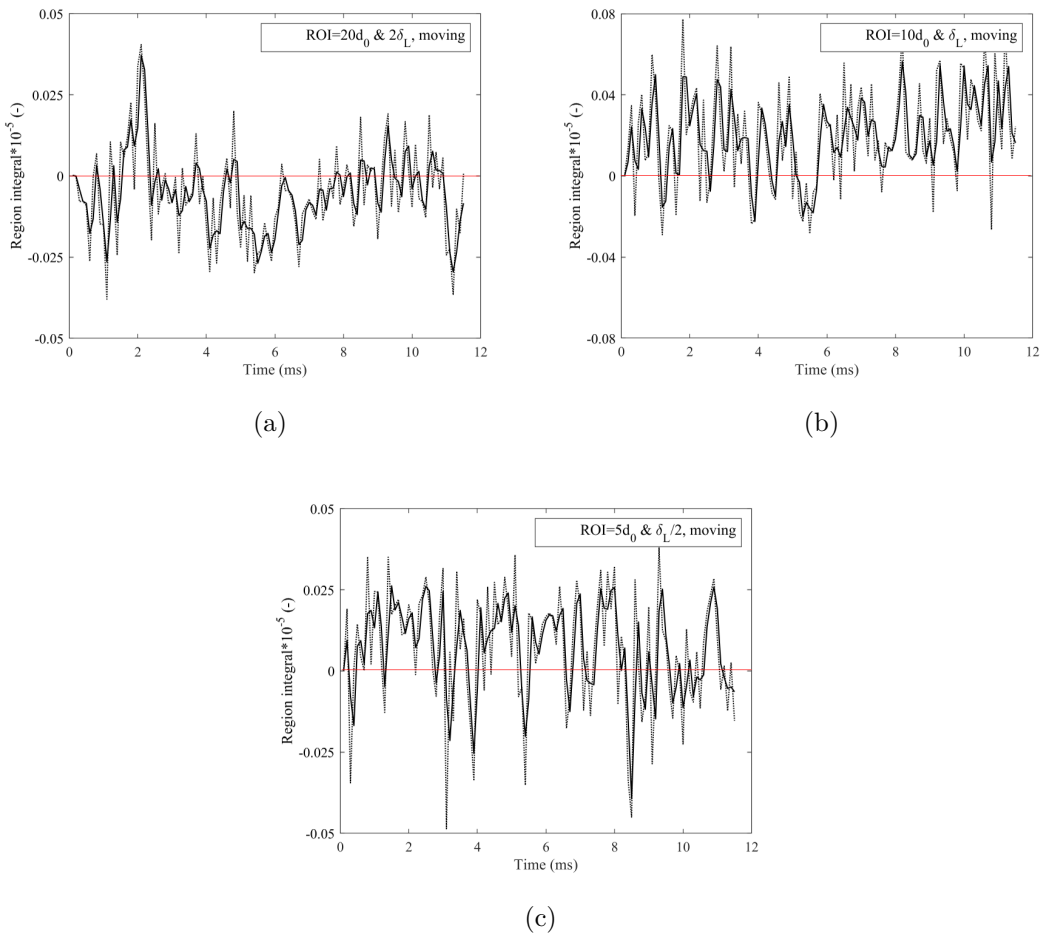


Figure 5.21: Variation in integral of signal on time due to droplet passage ($d_{p,0}$=55.4 $\mu$m) at SBP-2 with moving ROI.

#### 5.2.2.4 Wave Propagation on Flame Surface

The chemiluminescence experiments also showed that a wave occurs on the flame surface after the droplet passage. This wave, first, propagates with an increasing amplitude and then vanishes towards the edge of the bumped flame surface for propane/air flames at $\phi$=1.4, 1.3, and 1.2. Figure 5.22 gives an example of a propagating wave. At t=0, the flame is at rest and undisturbed, while at t=2.8 ms, the ethanol droplet crossed the flame surface. The lifetime of the wave is calculated as nearly 9.1 ms.

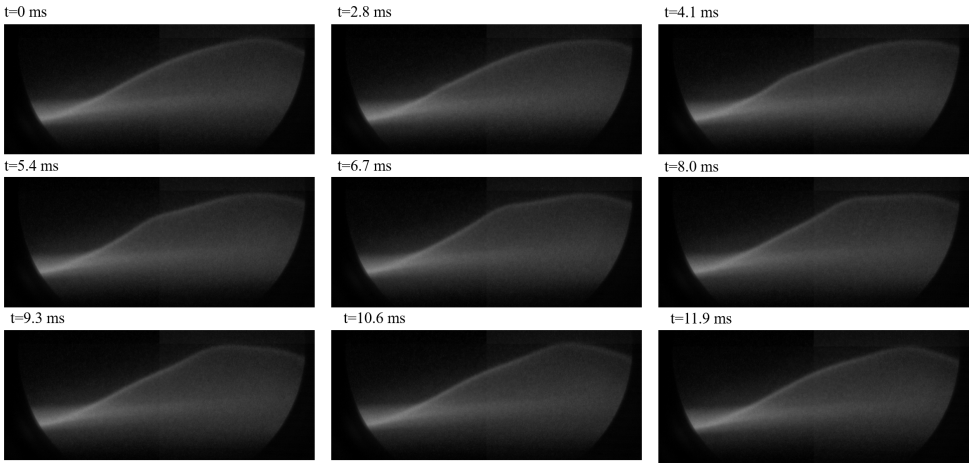


Figure 5.22: Propagation of a wave on the flame surface after the droplet passage at SBP-4 with ethanol droplet ($d_{p,0}$=51.93 $\mu$m) ($t$=0 ms: initially stable gaseous flame, $t$=2.8 ms: ethanol droplet passage through the flame front, $t$=4.1-10.6 ms: wave propagation on the flame surface, $t$=11.9 ms: recovered and stable gaseous flame).

When the droplet approaches the preheating zone, it starts to evaporate. Especially in the reaction zone, the evaporation process accelerates due to the steep temperature profile, and additional gas will build up. This situation causes an expansion of gases and an increase in fuel concentration, leading to the formation of perturbations on the flame surface. Due to the created bump on the flame surface, the wave propagates from a flat zone into a concave zone with negative curvature where the gas velocity increases, as in Figure 5.2. It should be noted that $Le_{eff}$ is greater than 1 for all performed conditions (Figure 5.8). Therefore, perturbations will most likely to be damped out and the flame will be stabilized due to high thermal diffusivity compared to mass diffusivity.

In order to understand the nature of the propagating wave on the flame surface, first, it is assumed that the flame is perturbed with a weak harmonic perturbation and the wave has a structure of the sinusoidal signal. The properties of a sinusoidal wave are given in Figure 5.23. Three main properties define the wave: amplitude, $A$, angular frequency, $\omega_0$, and phase difference, $\psi$. Accordingly, the signal equation can be written in Equation 5.12 as a function of time. In this study, the phase difference is assumed to be zero.

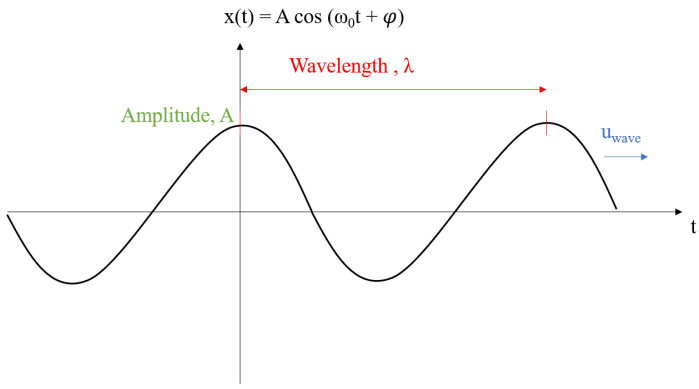


Figure 5.23: Continuous time sinusoidal signal.

$$x(t) = A.cos(\omega_0 t + \psi) \tag{5.12}$$

Angular frequency measures the displacement of any properties of the wave per unit time and can be defined in terms of frequency, $f$, given in Equation 5.13. Frequency is indicated as the number of cycles of signal taking place in a second, while the velocity of a wave is the distance traveled by a point on the wave. Hence, frequency and velocity are proportionate for any wave relation, and it can be related to the wavelength, $\lambda$:

$$\omega_0 = 2\pi f \tag{5.13}$$

$$f = \frac{u_{wave}}{\lambda} \tag{5.14}$$

In this study, the propagating wave captured at the initial frame is assumed to be the first rise of the sinusoidal wave; hence, the wavelength of the propagating wave is accepted as two times the parallel length of the captured perturbation with respect to flame, as it is described in Chapter 3. The distance between the flame and the peak of the perturbation is computed as the amplitude of the wave at each time sequence.

In Figure 5.24, the variation of the wavelength over time is reported at each condition. The initial wavelength of the disturbance is nearly equal to 11, 5, and 7 times the flame thickness, $\delta_L$, and 73, 45, and 90 times the initial droplet diameter, $d_0$ for $\phi$=1.2, 1.3 and 1.4, respectively. Although the largest droplet

is injected at $\phi$=1.2, the maximum impact of the droplet passage is observed for the richest case whose $Le_{eff}$ is close to unity and flame thickness is the largest with the lowest flame temperature. It can be emphasized that weak flames are more prone to droplet passage leading to the creation of intrinsic instabilities. The wavelength of the perturbation is nearly constant for a while after reaching a maximum value and then decreases towards the end time of the wave.

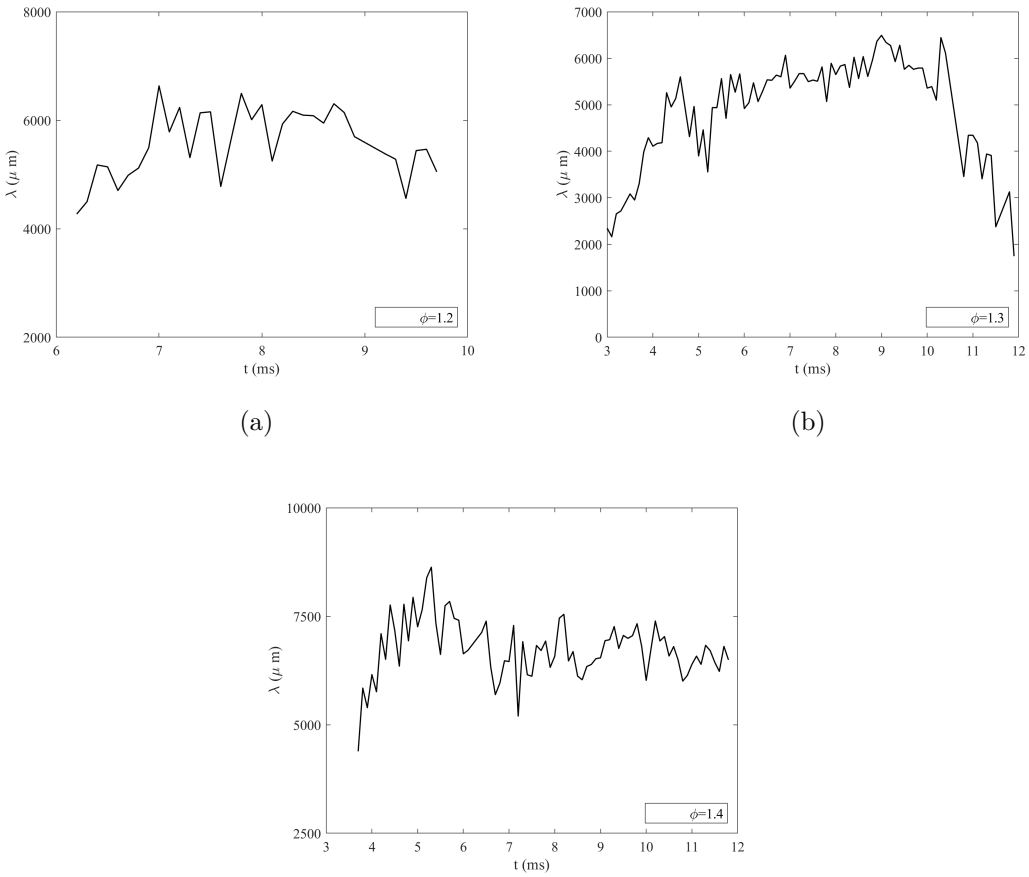


Figure 5.24: Variation of wavelength of the perturbation over time at (a) SBP-3, (b) SBP-4 and (c) SBP-5 for propane/air flames.

The variation in amplitude of the propagating wave over time at all conditions is given in Figure 5.25. It is seen that the amplitude of the wave increases after a certain time, and then it decreases as the wave decays. The starting point of the wave is just after the droplet injection point, where the flame is completely flat and strained. While it travels on the flame surface, the flame becomes

slightly concave, and in this region, the heat flux is more dominant than the mass dispersion. Consequently, the perturbation amplitude tends to be reduced in this region. It can also be concluded at the richest case, the wave can grow more than the other flame conditions and the observed maximum amplitude is increasing with the increase in fuel to oxidizer ratio.

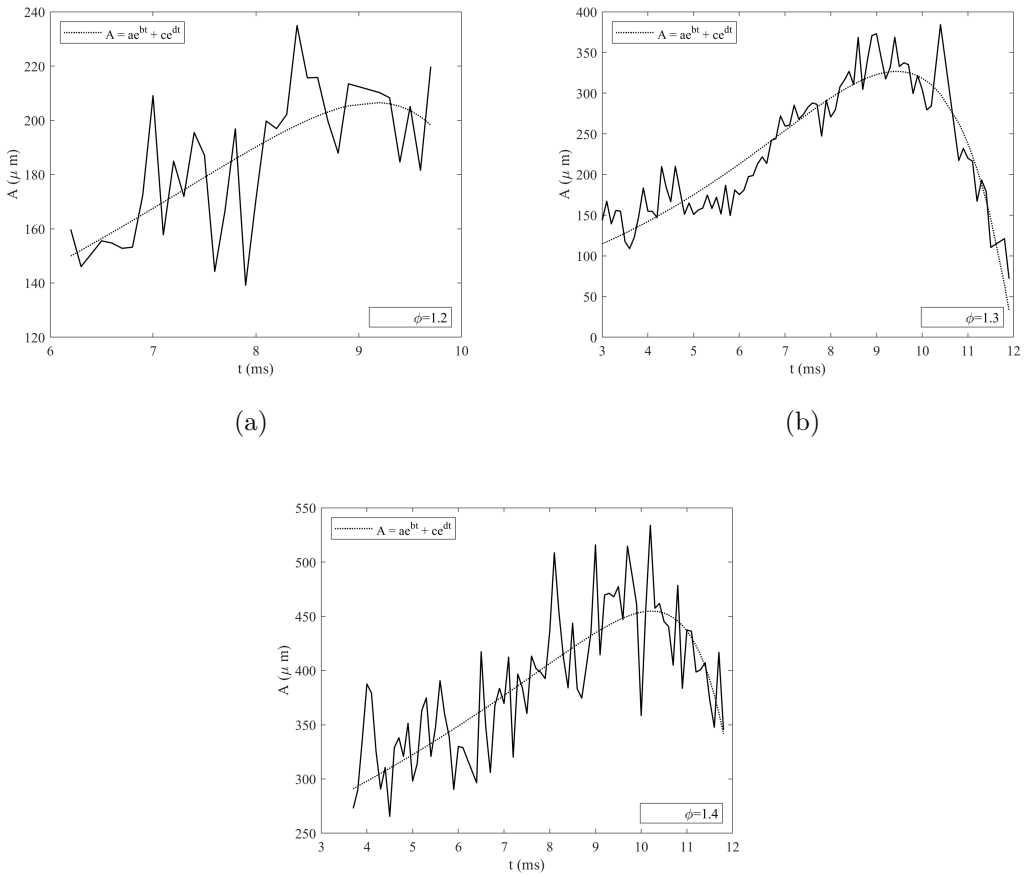


Figure 5.25: Variation of amplitude of the perturbation over time at (a) SBP-3, (b) SBP-4 and (c) SBP-5 for propane/air flames.

The amplitude variation is modeled as the summation of two exponential functions:

$$A(t) = a \exp(bt) + c \exp(dt) \tag{5.15}$$

Calculated parameters for the variation of amplitude in time are given in Table 5.2. It is seen that the modeled function fits well for $\phi$=1.3 and 1.4 while for the leanest case reported, the decaying part cannot be captured well. This situation can be explained by two main reasons. First of all, for $\phi$=1.2, the computation of wave properties is intricate due to the fact that the luminosity of the flame is low compared to richer cases and the isolation of the wave from the flame baseline is more complicated, leading to possible noise data calculation at certain time sequences. Secondly, $Le_{eff}$ is computed as 1.24 for $\phi$=1.2 making this condition is less prone to disturbances due to the stabilization of small perturbations.

In order to characterize the propagating wave, the frequency of the wave must be computed. Since the wavelength is known, the propagation velocity of the wave is first calculated, and then the frequency from Equation 5.14. The velocity of the wave is computed based on the displacement of the barycenter of the observed bump on the flame surface and reported in Figure 5.26. Although the calculated instantaneous velocity of the wave is noisy, it can be said that the wave propagates with a mean velocity of 2000 $\mu$m/ms. Accordingly, the frequency is computed and reported in Figure 5.27.

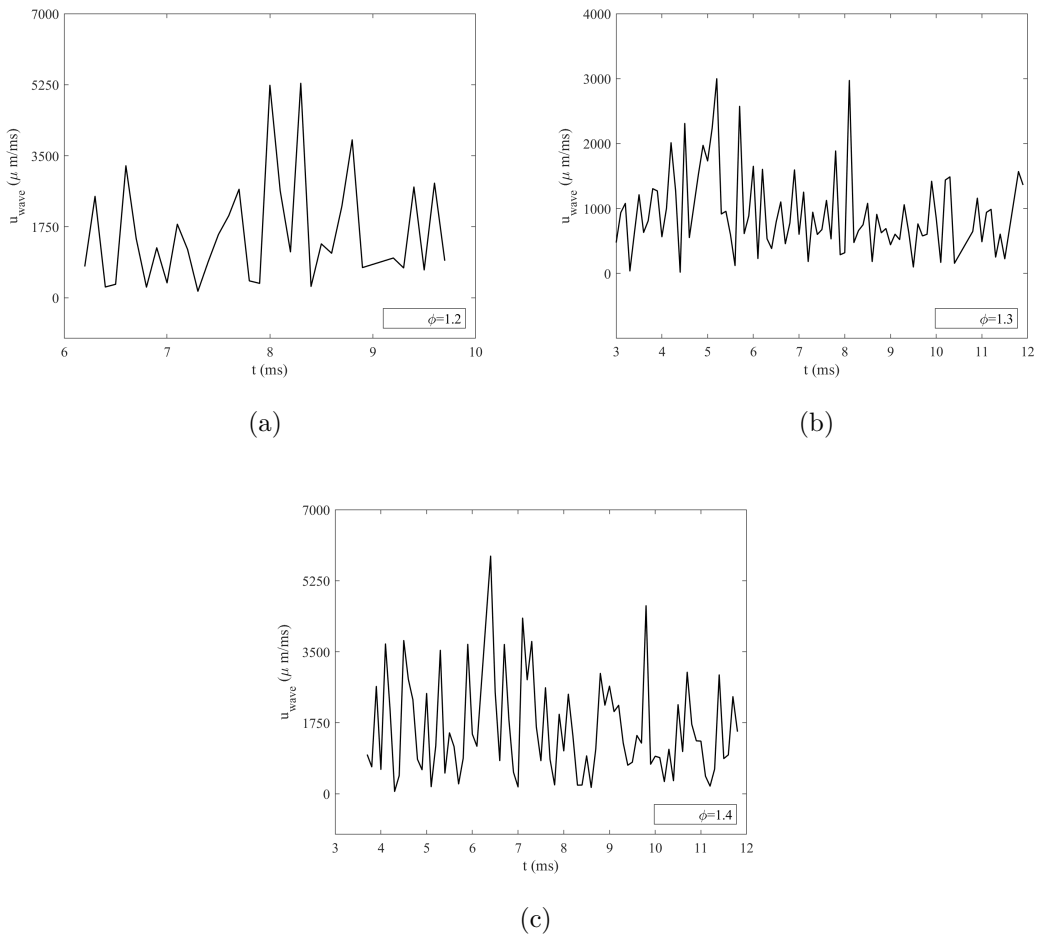


Figure 5.26: Variation of velocity of the perturbation over time at (a) SBP-3, (b) SBP-4 and (c) SBP-5 for propane/air flames.

Since the frequency of the wave varies as the wave propagates, mean frequency, $\bar{f}$ is defined in order to characterize more clearly the wave properties. Computed mean frequency values are given in Table 5.2. The highest frequency is calculated for the leanest case meaning that the mean angular displacement of the propagating wave per unit time is the highest. Accordingly, the wave equation is defined with a time-varying amplitude and mean frequency of the wave, as in Equation 5.16. The properties are reported in Table 5.2.

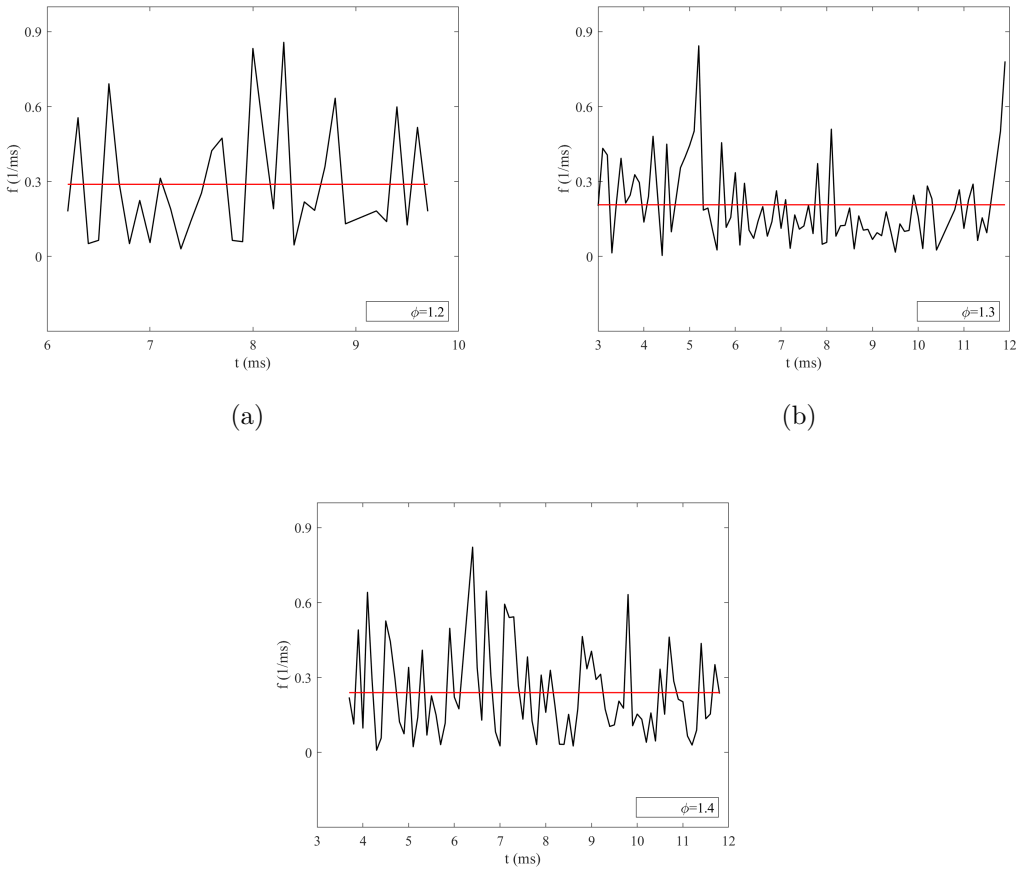


(a) (b)

(c)

Figure 5.27: Variation of frequency of the perturbation over time at (a) SBP-3, (b) SBP-4 and (c) SBP-5 for propane/air flames.

$$x(t) = A(t)cos(2\pi\bar{f}t) \tag{5.16}$$

Table 5.2: Experimentally determined properties of a propagating wave on the flame surface after droplet passage.

| | $\phi$ | A | | | | $\bar{f}$ |
|---|---|---|---|---|---|---|
| Condition | | a | b | c | d | (1/ms) |
| SBP-3 | 1.2 | -5.8x10$^{-5}$ | 1.410 | 61.6 | 0.144 | 0.289 |
| SBP-4 | 1.3 | -5.9x10$^{-1}$ | 0.615 | 59.4 | 0.230 | 0.207 |
| SBP-5 | 1.4 | -1.8x10$^{-4}$ | 1.180 | 217.3 | 0.079 | 0.239 |

The wave equation is graphically represented for all cases in Figure 5.28. Although all waves are damped out after a certain time, it is seen that for $\phi$=1.4, the wave grows more on the surface due to weaker thermodiffusive effects.

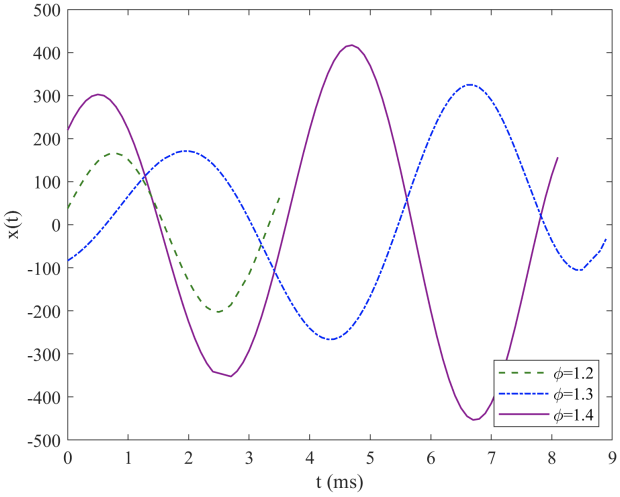


Figure 5.28: Propagation of the wave on the flame surface in time.

In order to understand the response of the flame to the perturbation, growth rate is calculated from dispersion relations given in Equation 5.2 and Equation 5.8. The former includes the hydrodynamic effects only, while the latter also includes the diffusion effects. Wavenumber, $k$ is computed as the reciprocal of the measured wavelength of the propagating waves, and it is nondimensionalized by multiplying with the laminar flame thickness, $\delta_L$. Change in nondimensional growth rate, $\omega\tau_f$ with $\tau_f = \delta_L/S_L$ being the characteristic flame time is plotted against the measured wavenumbers and high wavenumbers to understand the behaviour of the flame.

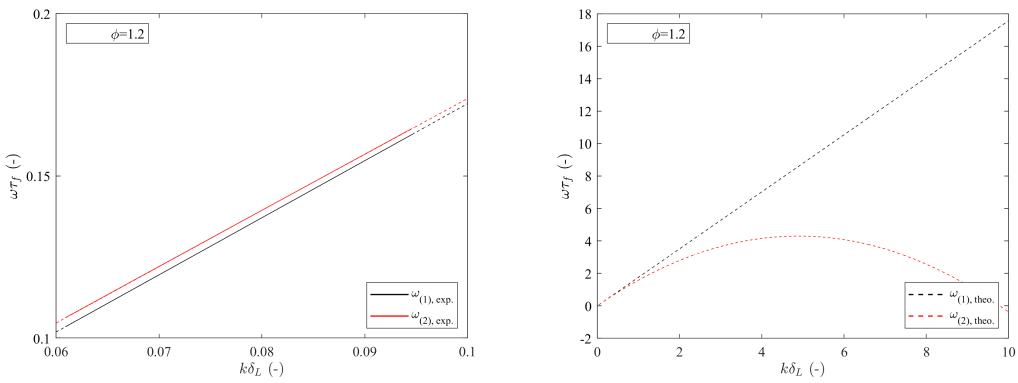


(a) (b)

Figure 5.29: Growth rate of (a) measured perturbations due to droplet passage and (b) perturbations at different wavelengths at SBP-3.

For all conditions, the growth rates related to the hydrodynamic instability mechanism (black dashed lines) are always above the one including the thermodiffusive effects (red dashed lines) at any wavenumber. Cases with high peak growth rates will be thought of as more unstable than cases with low peak growth rates because the dispersion relations generally allow quantifying the level of instability. Critical wavenumber, $k_c$ can be defined for the point at which the growth rate changes sign. For propane/air flame at the performed conditions, the critical wavenumber can be reported as $10\delta_L$, $4\delta_L$ and $3\delta_L$ for $\phi$=1.2, 1.3 and 1.4, respectively.

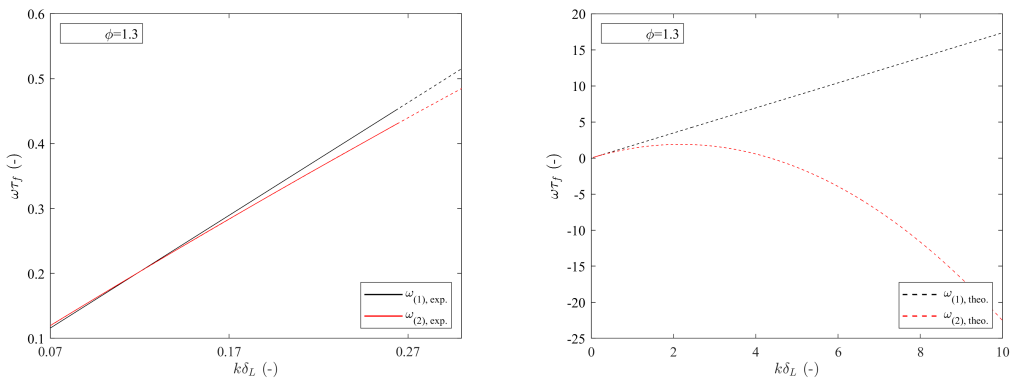


(a) (b)

Figure 5.30: Growth rate of (a) measured perturbations due to droplet passage and (b) perturbations at different wavelengths at SBP-4.

For the perturbations caused by the droplet passage, growth rate is calculated accordingly with the computed wavenumbers and reported in Figure 5.29a, Figure 5.30a and Figure 5.31a. The growth of the perturbation is observed to be at a linear phase and slightly disturbing the flame, having a positive growth rate. Since the flame tends to be stable at the performed flame conditions, small perturbations due to the droplet will not affect the structure vastly, and eventually, it will be damped out at all performed conditions.

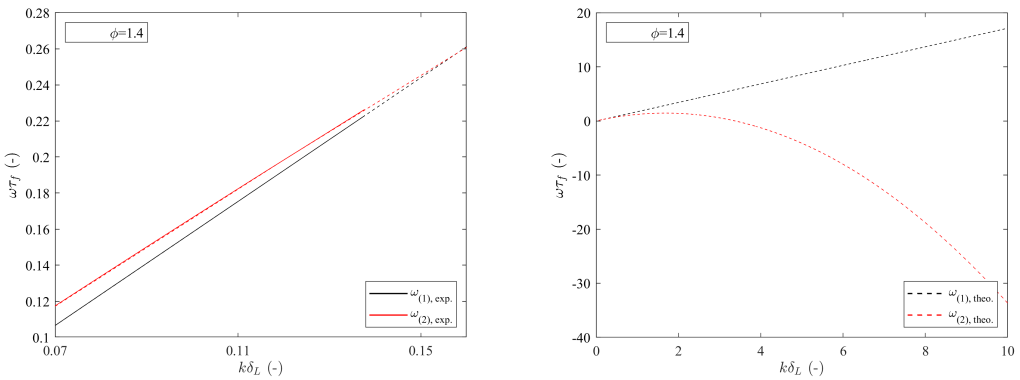


(a) (b)

Figure 5.31: Growth rate of (a) measured perturbations due to droplet passage and (b) perturbations at different wavelengths at SBP-5.

As pointed out previously, the flame structure is not directly affected for the droplets whose initial diameters are less than 20 $\mu$m and evaporating inside the reaction zone. At the conditions performed for the spherical expanding flames described in part 5.2.1, the droplets are small, and the ratio between flame thickness to the initial droplet size is nearly 20, meaning that there is enough space in the reaction zone for droplet evaporation. However, it is observed that the flames are intrinsically unstable, possibly due to low inter-droplet distance and a high number of droplets. As the flame approaches the droplets, the heat will be taken from the flame to the droplet for evaporation, leading to local extinction on the flame surface and vapor build-up. Since the number of droplets is high, there is no time in the chamber for the propagating flame to recover itself, considering the fact that the total propagation time of the flame is nearly 20 ms, whereas the recovery time is measured as 5 ms from propane/air flames.

As for the stagnation flame, although the disturbance can be created on the flame surface due to a single droplet passage, the flame is observed to be intrinsically stable. It can be interpreted that the instabilities are not observed due to the local interaction of the flame and the droplet, but they are triggered because of the droplets. Injection of a single droplet with a very large inter-distance provides enough time for the flame to recover itself since the lifetime of the perturbations is nearly 15 ms. There may also be a contribution of gravity for flame stabilization.

## 5.3 Conclusions

This chapter focuses on the onset of instabilities and changes in flame morphology due to droplet-flame interactions. The first set of experiments is performed under microgravity conditions with Schlieren visualization for spherically expanding $C_2H_5OH$/air flames. After observing local sinks due to droplets, a new set of experiments are configured with a stagnation burner to investigate the physical phenomenon deeply. The interaction of rich $C_3H_8$/air flames with an isolated ethanol droplet is investigated via chemiluminescence and ILIDS methods.

The main outcomes can be listed as follows:

i. Schlieren images revealed that at the beginning of the cellular structure formation, dark spots are observed linking to the signal loss in a density gradient. This phenomenon is assumed to be local extinction and quenching on the flame front due to either the presence or the evaporation of liquid droplets.

ii. From the gas phase change, it is observed that all evaporated ethanol reacts with oxygen in the flame zone, except from $\phi$=1.1, due to the lack of excess oxygen in the gaseous phase for methane/air flames.

iii. The heat is taken by the evaporating droplet in the flame zone, and the vaporized ethanol diffuses nearly to 800 $\mu$m along the flame for $d_{p,0}$=50 $\mu$m. This leads to local quenching of the flame. The quenching phenomenon is captured via chemiluminescence by computing the cumulative signal inside a region where the droplet crosses the flame.

iv. The height and length of the ROI is set to the multiples of flame thickness and initial droplet diameter, respectively. The signal decrease can be captured for all cases in an almost 200x250 $\mu m^2$ whereas, for flame conditions near to stoichiometry, it is hard to distinguish the signal loss, especially with an adaptive ROI due to the fact that the luminosity of the flame is decreasing as it becomes leaner.

v. The percentage of signal loss is reported as 13, 10.7, 5.1, and 1.8 % for $\phi$=1.4, 1.3, 1.2, and 1.1, respectively. As the flame becomes stronger, i.e., higher flame temperature with a shorter flame thickness, the recovery time decreases.

vi. Due to the evaporation of liquid fuel, the gaseous phase will be fed with more fuel thanks to the evaporated fuel around the droplet. This concentration gradient locally changes the properties of flame. The build-up of evaporated fuel may also cause flame field extinction, possibility of leading to hydrodynamic instabilities.

vii. A propagating wave on the flame surface is observed at the performed conditions after the droplet passage. The wave is modeled as a continuous sinusoidal wave propagating at 2000 $\mu$m/ms velocity, and its amplitude is first increasing and then decreasing for all performed conditions.

viii. From the dispersion relations, rich propane/air flames are found to be stabilized due to thermodiffusive effects, and the perturbations caused by the droplet passage will be damped out eventually. However, it causes a minor unstable structure on the flame.

ix. The intrinsic instabilities are triggered by the presence of droplets in the cases where the flame cannot recover its initial state and locally extincts due to the heat sink effect from the presence of droplets.

# CHAPTER 6

# CONCLUSIONS AND REMARKS

## 6.1 Conclusions

The main objective of this study is to investigate the interaction of a single droplet with a laminar flame and to understand several physical phenomena, such as evaporation and flame instabilities. In this scope, experiments are conducted at CNRS ICARE laboratories, and simulations are carried out with the YALES2 solver from CNRS CORIA.

The first part of the study includes the experimental investigation of single droplet evaporation in the fuel-rich, stoichiometric and fuel-lean flame conditions. A stagnation burner is utilized to track the droplet evaporation sequence through a stationary premixed laminar flame. An isolated ethanol droplet having nearly 50 $\mu$m initial diameter is injected through methane/air stagnation flames . The motion of the droplet and velocity of the unburnt gases are tracked via PTV and PIV, respectively. Simultaneously, the change in diameter of the droplet is tracked via ILIDS. Simulations are performed with different configurations, including stationary droplet evaporation surrounded by burnt gases at the flame conditions, the injection of an ethanol droplet to the stagnation flame field, and more realistic flame conditions with the real burner geometry. The whole sequence of droplet evaporation is tracked, and the properties of the droplet is computed using Lagrangian evaporation models, including Spalding and Abramzon-Sirignano models.

The flame temperature is found to be the most dominant effect on the evaporation rate rather than the burnt gas composition and flame strain rate. Addition-

ally, the evaporation constant is computed to be almost insensitive to the initial droplet diameter. Mean evaporation temperature is reported for the droplet passing through a temperature gradient, and the average evaporation rate is determined between 0.5-0.7 $mm^2/s$. The evaporation rate is also expressed empirically as an exponential function of flame parameters, and it is found to be slightly dependent on the flame speed and flame thickness. The critical diameter of an ethanol droplet is calculated to be nearly 20 $\mu$m indicating that a larger droplet can cross the flame region and cause local modifications.

The second part of the study covers the flame morphology changes due to the presence of droplets at different flame configurations. The first set of experiments is conducted at zero-g during the parabolic flights of CNES with spherically expanding aerosol ethanol/air flames via Schlieren method. The initiation of instabilities triggered by the droplets are evaluated qualitatively in the previously performed flame-rich conditions. Accordingly, stagnation burner experiments are designed with rich propane/air flames and ethanol droplet in order to observe local changes on the flame surface. Chemiluminescence technique is utilized with an intensifier to observe the flame structure, while ILIDS is used to compute the initial droplet diameter. Local extinction on the flame surface is evaluated when the droplet crosses the flame region, as well as the characteristics of a propagating signal triggered by the passage of the droplet.

Cellular instabilities are observed to be initialized by the dark spots on the surface of flame in the presence of droplets, leading to local quenching on the flame. The cumulative signal computations from the location of droplet passage on propane/air flames indicate that at the flame conditions close to stoichiometry, it is difficult to distinguish the signal loss because the luminosity of the flame decreases as it becomes leaner. The accumulation of vapor evaporated inside the flame zone may result in local extinction leading to hydrodynamic instabilities. Accordingly, a propagating wave on the flame surface is observed after the droplet passage and modeled as a continuous sinusoidal signal with varying amplitude. Rich propane/air flames are found to be stabilized by thermodiffusive effects, and the disturbances brought on by the passage of the droplet will eventually be damped out.

## 6.2 Remarks and Future Studies

In terms of experimental investigation, the deformation of the flame surface, as well as the droplet burning behavior, can be determined by OH PLIF method. Consequently, this technique can be used simultaneously via ILIDS for different flame configurations to characterize the flame surface recovery and to relate with the droplet parameters.

The coupling of the experiments with well-defined and detailed CFD simulations is essential to deeply understand the flame/droplet interactions. Accordingly, stagnation burner simulations can be performed for various flame conditions in 3D with detailed modeling of the flow field by introducing adaptive mesh refinement on the flame zone to capture the local changes due to the passage of droplets. Parametric studies can be conducted by changing the inter-distance between droplets and their velocities.

# REFERENCES


[1] B. Abramzon and W. A. Sirignano. Droplet vaporization model for spray combustion calculations. *International journal of heat and mass transfer*, 32(9):1605–1618, 1989.

[2] A. Adam, P. Leick, G. Bittlinger, and C. Schulz. Visualization of the evaporation of a diesel spray using combined mie and rayleigh scattering techniques. *Experiments in fluids*, 47(3):439–449, 2009.

[3] F. Atzler, F. X. Demoulin, M. Lawes, Y. Lee, and N. Marquez. Burning rates and flame oscillations in globally homogeneous two-phase mixtures (flame speed oscillations in droplet cloud flames). *Combustion Science and Technology*, 178:2177–2198, 2006.

[4] C. Bariki. *Interaction entre une flamme de prémélange et une structure tourbillonnaire*. PhD Thesis, Université d'Orléans, CNRS ICARE, 2018.

[5] J. Bechtold and M. Matalon. The dependence of the markstein length on stoichiometry. *Combustion and flame*, 127(1-2):1906–1913, 2001.

[6] L. Berger, A. Attili, and H. Pitsch. Intrinsic instabilities in premixed hydrogen flames: Parametric variation of pressure, equivalence ratio, and temperature. Part 1 - Dispersion relations in the linear regime. *Combustion and Flame*, 240:111935, 2022.

[7] R. B. Bird. Transport phenomena. *Appl. Mech. Rev.*, 55(1):R1–R4, 2002.

[8] M. Birouk and I. Gökalp. Current status of droplet evaporation in turbulent flows. *Progress in energy and combustion science*, 32(4):408–423, 2006.

[9] M. Bonanni and M. Ihme. Interaction of preferential evaporation and low-temperature chemistry in multicomponent counterflow spray flames. *Proceedings of the Combustion Institute*, 2022.

[10] N. Bouvet. *Experimental and numerical studies of the fundamental flame speeds of methane/air and syngas ($H_2$/CO)/air mixtures.* PhD Thesis, Université d'Orléans, CNRS ICARE, 2009.

[11] D. Bradley, M. Lawes, S. Liao, and A. Saat. Laminar mass burning and entrainment velocities and flame instabilities of i-octane, ethanol and hydrous ethanol/air aerosols. *Combustion and Flame*, 161:1620–1632, 2014.

[12] G. Brenn, L. J. Deviprasath, F. Durst, and C. Fink. Evaporation of acoustically levitated multi-component liquid droplets. *International Journal of Heat and Mass Transfer*, 50:5073–5086, 2007.

[13] R. S. Brokaw. Approximate formulas for the viscosity and thermal conductivity of gas mixtures. *The Journal of Chemical Physics*, 29(2):391–397, 1958.

[14] J. H. Burgoyne and L. Cohen. The effect of drop size on flame propagation in liquid aerosols. *Proceedings of the Royal Society of London. Series A. Mathematical and Physical Sciences*, 1954.

[15] C. M. Burt, A. J. Mutziger, R. G. Allen, and T. A. Howell. Evaporation research: Review and interpretation. *Journal of irrigation and drainage engineering*, 131(1):37, 2005.

[16] G. Castanet, B. Frackowiak, C. Tropea, and F. Lemoine. Heat convection within evaporating droplets in strong aerodynamic interactions. *International Journal of Heat and Mass Transfer*, 54:3267–3276, 2011.

[17] G. Castanet, P. Lavieille, M. Lebouché, and F. Lemoine. Measurement of the temperature distribution within monodisperse combusting droplets in linear streams using two-color laser-induced fluorescence. *Experiments in Fluids*, 35:563–571, 2003.

[18] G. Castanet, M. Lebouché, and F. Lemoine. Heat and mass transfer of combusting monodisperse droplets in a linear stream. *International journal of heat and mass transfer*, 48(16):3261–3275, 2005.

[19] C. Chauveau, M. Birouk, F. Halter, and I. Gökalp. An analysis of the droplet support fiber effect on the evaporation process. *International Journal of Heat and Mass Transfer*, 128:885–891, 2019.

[20] G. Darrieus. Propagation d'un front de flamme. *La Technique Moderne*, 30:18, 1938.

[21] P. Domingo-Alvarez. *High-Pressure Combustion Large-Eddy Simulation for an A Priori Optical Diagnostics Validation*. PhD Thesis, Normandie Université, CNRS CORIA, 2019.

[22] H. A. Dwyer. Calculations of droplet dynamics in high temperature environments. *Progress in Energy and Combustion Science*, 15(2):131–158, 1989.

[23] I. Düwel, J. Schorr, J. Wolfrum, and C. Schulz. Laser-induced fluorescence of tracers dissolved in evaporating droplets. *Applied Physics B*, 78:127–131, 2004.

[24] C. Espey, J. E. Dec, T. A. Litzinger, and D. A. Santavicca. Quantitative 2-D Fuel Vapor Concentration Imaging in a Firing D.I. Diesel Engine Using Planar Laser-Induced Rayleigh Scattering. *SAE Transactions*, 103:1145–1160, 1994. Publisher: SAE International.

[25] L. Fan, B. Tian, C. T. Chong, M. N. M. Jaafar, K. Tanno, D. McGrath, P. M. de Oliveira, B. Rogg, and S. Hochgreb. The effect of fine droplets on laminar propagation speed of a strained acetone-methane flame: Experiment and simulations. *Combustion and Flame*, 229:111377, 2021.

[26] H. Ghassemi, S. W. Baek, and Q. S. Khan. Experimental study on binary droplet evaporation at elevated pressures and temperatures. *Combustion Science and Technology*, 178(6):1031–1053, 2006.

[27] G. Godsave. Studies of the combustion of drops in a fuel spray—the burning of single drops of fuel. In *Symposium (international) on combustion*, volume 4, pages 818–830. Elsevier, 1953.

[28] D. G. Goodwin, R. L. Speth, H. K. Moffat, and B. W. Weber. Cantera: An object-oriented software toolkit for chemical kinetics, thermodynamics, and transport processes, 2018.

[29] J. Greenberg, A. McIntosh, and J. Brindley. Instability of a flame front propagating through a fuel-rich droplet–vapour–air cloud. *Combustion Theory and Modelling*, 3:567–584, 1999.

[30] J. B. Greenberg. Propagation and extinction of an unsteady spherical spray flame front. *Combustion Theory and Modelling*, 7:163–174, 2003.

[31] J. B. Greenberg. Finite-rate evaporation and droplet drag effects in spherical flame front propagation through a liquid fuel mist. *Combustion and Flame*, 148:187–197, 2007.

[32] J. B. Greenberg, A. C. McIntosh, and J. Brindley. Linear stability analysis of laminar premixed spray flames. *Proceedings of the Royal Society a-Mathematical Physical and Engineering Sciences*, 457:1–31, 2001.

[33] H. Grosshans, M. Griesing, M. Mönckedieck, T. Hellwig, B. Walther, S. R. Gopireddy, R. Sedelmayer, W. Pauer, H.-U. Moritz, N. A. Urbanetz, and E. Gutheil. Numerical and experimental study of the drying of bi-component droplets under various drying conditions. *International Journal of Heat and Mass Transfer*, 96:97–109, 2016.

[34] F. Halter, C. Chauveau, N. Djebaïli-Chaumeix, and I. Gökalp. Characterization of the effects of pressure and hydrogen concentration on laminar burning velocities of methane–hydrogen–air mixtures. *Proceedings of the Combustion Institute*, 30(1):201–208, 2005.

[35] K. Han, G. Song, X. Ma, and B. Yang. An experimental and theoretical study of the effect of suspended thermocouple on the single droplet evaporation. *Applied Thermal Engineering*, 101:568–575, 2016.

[36] W. Han and Z. Chen. Effects of finite-rate droplet evaporation on the ignition and propagation of premixed spherical spray flame. *Combustion and Flame*, 162:2128–2139, 2015.

[37] W. Han and Z. Chen. Effects of finite-rate droplet evaporation on the extinction of spherical burner-stabilized diffusion flames. *International Journal of Heat and Mass Transfer*, 99:691–701, 2016.

[38] S. Hayashi and S. Kumagai. Flame propagation in fuel droplet-vapor-air mixtures. *Symposium (International) on Combustion*, 15:445–452, 1975.

[39] S. Hayashi, S. Kumagai, and T. Sakai. Propagation velocity and structure of flames in droplet-vapor-air mixtures. *Combustion Science and Technology*, 15, 1977.

[40] R. Haywood, R. Nafziger, and M. Renksizbulut. A detailed examination of gas and liquid phase transient processes in convective droplet evaporation. 1989.

[41] J. O. Hirschfelder, C. F. Curtiss, and R. B. Bird. Molecular theory of gases and liquids. *Molecular theory of gases and liquids*, 1964.

[42] G. L. Hubbard, V. E. Denny, and A. F. Mills. Droplet evaporation: Effects of transients and variable properties. *International Journal of Heat and Mass Transfer*, 18:1003–1008, 1975.

[43] T. Kawaguchi, T. Kobayashi, and M. Maeda. Measurement of spray flow by an improved Interferometric Laser Imaging Droplet Sizing (ILIDS) system. In R. J. Adrian, D. F. G. Durao, M. V. Heitor, M. Maeda, C. Tropea, and J. H. Whitelaw, editors, *Laser Techniques for Fluid Mechanics*, pages 209–220, Berlin, 2002. Springer-Verlag Berlin.

[44] S. Kumagai, T. Sakai, and S. Okajima. Combustion of free fuel droplets in a freely falling chamber. *Symposium (International) on Combustion*, 13:779–785, 1971.

[45] A. Labergue, A. Delconte, G. Castanet, and F. Lemoine. Study of the droplet size effect coupled with the laser light scattering in sprays for two-color LIF thermometry measurements. *Experiments in Fluids*, 52:1121–1132, 2012.

[46] L. Landau. On the theory of slow combustion. *Acta Phys.*, 19:77–85, 1944.

[47] H. Larabi. *Vers la modélisation multi-composants des flammes de spray.* PhD Thesis, Normandie Université, CNRS CORIA, 2019.

[48] P. Lavieille, F. Lemoine, G. Lavergne, and M. Lebouché. Evaporating and combusting droplet temperature measurements using two-color laser-induced fluorescence. *Experiments in Fluids*, 31:45–55, 2001.

[49] C. Law. Recent advances in droplet vaporization and combustion. *Progress in energy and combustion science*, 8(3):171–201, 1982.

[50] M. Lawes, Y. Lee, and N. Marquez. Comparison of iso-octane burning rates between single-phase and two-phase combustion for small droplets. *Combustion and Flame*, 144:513–525, 2006.

[51] A. Lee and C. K. Law. An experimental investigation on the vaporization and combustion of methanol and ethanol droplets. *Combustion Science and Technology*, 86:253–265, 1992.

[52] Q. Li, H. Zhang, and C. Shu. Propagation of heterogeneous and homogeneous planar flames in fuel droplet mists. *International Journal of Multiphase Flow*, 133:103452, 2020.

[53] Q. Li, H. Zhang, and C. Shu. Propagation of weakly stretched premixed spherical spray flames in localized homogeneous and heterogeneous reactants. *Physics of Fluids*, 32:123302, 2020.

[54] X. Ma, F. Zhang, K. Han, B. Yang, and G. Song. Evaporation characteristics of acetone–butanol–ethanol and diesel blends droplets at high ambient temperatures. *Fuel*, 160:43–49, 2015.

[55] C. Maqua, G. Castanet, and F. Lemoine. Bicomponent droplets evaporation: Temperature measurements and modelling. *Fuel*, 87:2932–2942, 2008.

[56] M. Matalon. Intrinsic flame instabilities in premixed and nonpremixed combustion. *Annu. Rev. Fluid Mech.*, 39:163–191, 2007.

[57] M. Matalon, C. Cui, and J. K. Bechtold. Hydrodynamic theory of premixed flames: effects of stoichiometry, variable transport coefficients and arbitrary reaction orders. *Journal of Fluid Mechanics*, 487:179–210, 2003.

[58] L. A. Melton. Spectrally separated fluorescence emissions for diesel fuel droplets and vapor. *Applied Optics*, 22:2224–2226, 1983. Publisher: Optica Publishing Group.

[59] X. Mercier, M. Orain, and F. Grisch. Investigation of droplet combustion in strained counterflow diffusion flames using planar laser-induced fluorescence. *Applied Physics B*, 88(1):151–160, 2007.

[60] R. Miller, K. Harstad, and J. Bellan. Evaluation of equilibrium and non-equilibrium evaporation models for many-droplet gas-liquid flow simulations. *International Journal of Multiphase Flow*, 24(6):1025–1055, 1998.

[61] Y. Mizutani and A. Nakajima. Combustion of fuel vapor-drop-air systems: Part II—Spherical flames in a vessel. *Combustion and Flame*, 20:351–357, 1973.

[62] C. Morin, C. Chauveau, and I. Gökalp. Droplet vaporisation characteristics of vegetable oil derived biofuels at high temperatures. *Experimental Thermal and Fluid Science*, 21:41–50, 2000.

[63] V. Moureau, P. Domingo, and L. Vervisch. Design of a massively parallel CFD code for complex geometries. *Comptes Rendus Mécanique*, 339:141–148, 2011.

[64] C. J. Mueller, J. F. Driscoll, D. L. Reuss, M. C. Drake, and M. E. Rosalik. Vorticity generation and attenuation as vortices convect through a premixed flame. *Combustion and Flame*, 112:342–358, 1998.

[65] P. Narasu, S. Boschmann, P. Pöschko, F. Zhao, and E. Gutheil. Modeling and simulation of single ethanol/water droplet evaporation in dry and humid air. *Combustion Science and Technology*, 192:1233–1252, 2020.

[66] M. Nassouri. *Caractérisation expérimentale de la propagation d'une flamme laminaire dans un milieu diphasique (brouillard) à haute pression*

*et en microgravité*. PhD Thesis, Université d'Orléans, CNRS ICARE, 2014.

[67] Z. Naumann and L. Schiller. A drag coefficient correlation. *Z. Ver. Deutsch. Ing*, 77(318):e323, 1935.

[68] C. Nicoli, P. Haldenwang, and B. Denet. Premixed flame dynamics in presence of mist. *Combustion Science and Technology*, 191:197–207, 2019.

[69] H. Nomura, Y. Ujiie, H. J. Rath, J. Sato, and M. Kono. Experimental study on high-pressure droplet evaporation using microgravity conditions. *Symposium (International) on Combustion*, 26:1267–1273, 1996.

[70] S. Okajima and S. Kumagai. Further investigations of combustion of free droplets in a freely falling chamber including moving droplets. *Symposium (International) on Combustion*, 15:401–407, 1975.

[71] M. Orain and Y. Hardalupas. Droplet characteristics and local equivalence ratio of reacting mixture in spray counterflow flames. *Experimental thermal and fluid science*, 57:261–274, 2014.

[72] G. Ozel Erol, J. Hasslberger, M. Klein, and N. Chakraborty. A direct numerical simulation investigation of spherically expanding flames propagating in fuel droplet-mists for different droplet diameters and overall equivalence ratios. *Combustion Science and Technology*, 191(5-6):833–867, 2019.

[73] G. Parant, L. Zimmer, A. Renaud, and F. Richecoeur. Adaptation of a PTV method for droplets evaporating in vicinity of a flame. *Experiments in Fluids*, 63:100, 2022.

[74] D. Paulhiac, B. Cuenot, E. Riber, L. Esclapez, and S. Richard. Analysis of the spray flame structure in a lab-scale burner using large eddy simulation and discrete particle simulation. *Combustion and Flame*, 212:25–38, 2020.

[75] P. Pelce and P. Clavin. Influence of hydrodynamics and diffusion upon the stability limits of laminar premixed flames. *Journal of Fluid Mechanics*, 124:219–237, 1982.

[76] N. Peters. *Turbulent Combustion.* Cambridge University Press, Cambridge, England; New York, 2000.

[77] N. Peters and F. A. Williams. The asymptotic structure of stoichiometric methane-air flames. *Combustion and Flame*, 68:185–207, 1987.

[78] T. Poinsot and D. Veynante. *Theoretical and Numerical Combustion.* R.T. Edwards, Inc., 2005.

[79] V. Raghavan. Numerical modeling of evaporation and combustion of isolated liquid fuel droplets: a review. *Journal of the Indian Institute of Science*, 99(1):5–23, 2019.

[80] W. Ranz and J. Marshall. Wr: Evaporation from drops. *Chemical engineering progress*, 48:141–146, 1952.

[81] H. L.-u. Rehman, J. Weiss, and P. Seers. Effect of heat conduction on droplet life time and evaporation rate under forced convection at low temperatures. *Experimental Thermal and Fluid Science*, 72:59–66, 2016.

[82] G. Renoux. *Étude expérimentale de l'interaction goutte/flamme : propagation d'une flamme dans un aérosol en microgravité et passage d'une goutte à travers un front de flamme.* PhD Thesis, Université d'Orléans, CNRS ICARE, 2020.

[83] G. Renoux, F. Halter, and C. Chauveau. Experimental study of the morphology of two-phase flame instabilities in microgravity. *Atomization and Sprays*, 28:915–929, 2018.

[84] J. Reveillon. Direct numerical simulation of sprays: turbulent dispersion, evaporation and combustion. In *Multiphase reacting flows: modelling and simulation*, pages 229–269. Springer, 2007.

[85] J. Reveillon and L. Vervisch. Spray vaporization in nonpremixed turbulent combustion modeling: a single droplet model. *Combustion and flame*, 121(1-2):75–90, 2000.

[86] B. Rochette. *Modelisation et simulation de la combustion turbulente*

*diphasique dans les moteurs a´eronautiques*. PhD Thesis, Université de Toulouse, CERFACS, 2019.

[87] B. Rochette, E. Riber, and B. Cuenot. Effect of non-zero relative velocity on the flame speed of two-phase laminar flames. *Proceedings of the Combustion Institute*, 37(3):3393–3400, 2019.

[88] S. Russo and A. Gomez. The extinction behavior of small interacting droplets in cross-flow. *Combustion and flame*, 130(3):215–224, 2002.

[89] S. Russo and A. Gomez. Structure of laminar coflow spray flames at different pressures. *Proceedings of the Combustion Institute*, 29(1):601–608, 2002.

[90] F. L. Sacomano Filho, A. C. Santos, A. Vié, and G. C. Krieger Filho. A new robust modeling strategy for multi-component droplet heat and mass transfer in general ambient conditions. *International Journal of Heat and Mass Transfer*, 194:123102, 2022.

[91] S. B. Saharin, B. Lefort, C. Morin, C. Chauveau, L. L. Moyne, and R. Kafafy. Vaporization characteristics of ethanol and 1-propanol droplets at high temperatures. *Atomization and Sprays*, 22, 2012.

[92] S. Sahu, Y. Hardalupas, and A. M. K. P. Taylor. Simultaneous droplet and vapour-phase measurements in an evaporative spray by combined ILIDS and PLIF techniques. *Experiments in Fluids*, 55:1673, 2014.

[93] S. Sahu, Y. Hardalupas, and A. M. K. P. Taylor. Interaction of droplet dispersion and evaporation in a polydispersed spray. *Journal of Fluid Mechanics*, 846:37–81, 2018.

[94] J. Sangiovanni and M. Labowsky. Burning times of linear fuel droplet arrays: a comparison of experiment and theory. *Combustion and flame*, 47:15–30, 1982.

[95] M. Sanjosé, J. Senoner, F. Jaegle, B. Cuenot, S. Moreau, and T. Poinsot. Fuel injection model for euler–euler and euler–lagrange large-eddy simulations of an evaporating spray inside an aeronautical combustor. *International Journal of Multiphase Flow*, 37(5):514–529, 2011.

[96] A. Santos, A. Vié, and F. L. Sacomano Filho. Modeling droplet evaporation of multi-component liquid fuel. In *Proceedings of the European Combustion Meeting*, page 6, 2021.

[97] S. Sazhin, W. Abdelghaffar, E. Sazhina, and M. Heikal. Models for droplet transient heating: effects on droplet evaporation, ignition, and break-up. *International journal of thermal sciences*, 44(7):610–622, 2005.

[98] S. S. Sazhin. Advanced models of fuel droplet heating and evaporation. *Progress in energy and combustion science*, 32(2):162–214, 2006.

[99] S. S. Sazhin. Modelling of fuel droplet heating and evaporation: Recent results and unsolved problems. *Fuel*, 196:69–101, 2017.

[100] S. S. Sazhin, I. N. Shishkova, I. G. Gusev, A. Elwardany, P. Krutitskii, and M. Heikal. Fuel droplet heating and evaporation: new hydrodynamic and kinetic models. In *International Heat Transfer Conference*, volume 49385, pages 43–52, 2010.

[101] C. Schulz and V. Sick. Tracer-LIF diagnostics: quantitative measurement of fuel concentration, temperature and fuel/air ratio in practical combustion systems. *Progress in Energy and Combustion Science*, 31:75–121, 2005.

[102] W. A. Sirignano. Fuel droplet vaporization and spray combustion theory. *Progress in Energy and Combustion Science*, 9(4):291–322, 1983.

[103] D. B. Spalding. Combustion of liquid fuels. *Nature*, 165(4187):160–160, 1950.

[104] E. Starinskaya, N. Miskiv, A. Nazarov, V. Terekhov, V. Terekhov, O. Rybdylova, and S. Sazhin. Evaporation of water/ethanol droplets in an air flow: Experimental study and modelling. *International Journal of Heat and Mass Transfer*, 177:121502, 2021.

[105] J. Stengele, K. Prommersberger, M. Willmann, and S. Wittig. Experimental and theoretical study of one- and two-component droplet vaporization in a high pressure environment. *International Journal of Heat and Mass Transfer*, 42:2683–2694, 1999.

[106] P. A. Strizhak, R. S. Volkov, G. Castanet, F. Lemoine, O. Rybdylova, and S. S. Sazhin. Heating and evaporation of suspended water droplets: Experimental studies and modelling. *International Journal of Heat and Mass Transfer*, 127:92–106, 2018.

[107] A. L. Sánchez, J. Urzay, and A. Liñán. The role of separation of scales in the description of spray combustion. *Proceedings of the Combustion Institute*, 35:1549–1577, 2015.

[108] W. Thielicke and E. J. Stamhuis. PIVlab – Towards user-friendly, affordable and accurate digital Particle Image Velocimetry in MATLAB. *Journal of Open Research Software*, 2, 2014.

[109] R. Thimothée. *Caractérisation de la propagation d'une flamme dans un milieu diphasique (brouillards) en microgravité*. PhD Thesis, Université d'Orléans, CNRS ICARE, 2017.

[110] R. Thimothée, C. Chauveau, F. Halter, and I. Gökalp. Characterization of cellular instabilities of a flame propagating in an aerosol. In *Proceedings of ASME Turbo Expo 2015: Turbine Technical Conference and Exposition*, 2015.

[111] R. Thimothée, C. Chauveau, F. Halter, and I. Gökalp. Experimental investigation of the mechanisms of cellular instabilities developing on spherical two-phase flames. *Combustion Science and Technology*, 188:2026–2043, 2016.

[112] R. Thimothée, C. Chauveau, F. Halter, and I. Gökalp. Experimental investigation of the passage of fuel droplets through a spherical two-phase flame. *Proceedings of the Combustion Institute*, 36:2549–2557, 2017.

[113] R. Thimothée, C. Chauveau, F. Halter, C. Nicoli, P. Haldenwang, and B. Denet. Microgravity experiments and numerical studies on ethanol/air spray flames. *Comptes Rendus Mécanique*, 345:99–116, 2017.

[114] M. C. Thurber, F. Grisch, and R. K. Hanson. Temperature imaging with single- and dual-wavelength acetone planar laser-induced fluorescence. *Optics Letters*, 22:251–253, 1997.

[115] University of California San Diego, Mechanical and Aerospace Engineering-Combustion Research. Chemical-kinetic mechanisms for combustion applications v. 2016-12-14, 2016.

[116] A. Verdier, J. Marrero Santiago, A. Vandel, S. Saengkaew, G. Cabot, G. Grehan, and B. Renou. Experimental study of local flame structures and fuel droplet properties of a spray jet flame. *Proceedings of the Combustion Institute*, 36:2595–2602, 2017.

[117] A. Verdier, J. M. Santiago, A. Vandel, G. Godard, G. Cabot, and B. Renou. Local extinction mechanisms analysis of spray jet flame using high speed diagnostics. *Combustion and Flame*, 193:440–452, 2018.

[118] R. S. Volkov and P. A. Strizhak. Using planar laser induced fluorescence and micro particle Image Velocimetry to study the heating of a droplet with different tracers and schemes of attaching it on a holder. *International Journal of Thermal Sciences*, 159:106603, 2021.

[119] C. H. Wang, X. Q. Liu, and C. K. Law. Combustion and microexplosion of freely falling multicomponent droplets. *Combustion and Flame*, 56:175–197, 1984.

[120] J. Wang, X. Huang, X. Qiao, D. Ju, and C. Sun. Experimental study on effect of support fiber on fuel droplet vaporization at high temperatures. *Fuel*, 268:117407, 2020.

[121] Z. Wang, B. Yuan, Y. Huang, J. Cao, Y. Wang, and X. Cheng. Progress in experimental investigations on evaporation characteristics of a fuel droplet. *Fuel Processing Technology*, 231:107243, 2022.

[122] A. Williams. Combustion of droplets of liquid fuels: a review. *Combustion and flame*, 21(1):1–31, 1973.

[123] C. T. R. Wilson. On a method of making visible the paths of ionising particles through a gas. *Proceedings of the Royal Society of London. Series A, Containing Papers of a Mathematical and Physical Character*, 85:285–288, 1911.

[124] J. G. Wilson. *The principles of cloud-chamber technique.* Cambridge University Press, 2014.

[125] M. S. Wu and S. I. Yang. Combustion characteristics of multi-component cedar bio-oil/kerosene droplet. *Energy*, 113:788–795, 2016.

[126] S. I. Yang and M. S. Wu. The droplet combustion and thermal characteristics of pinewood bio-oil from slow pyrolysis. *Energy*, 141:2377–2386, 2017.

[127] A. L. Yarin, G. Brenn, O. Kastner, D. Rensink, and C. Tropea. Evaporation of acoustically levitated droplets. *Journal of Fluid Mechanics*, 399:151–204, 1999.

[128] A. L. Yarin, G. Brenn, and D. Rensink. Evaporation of acoustically levitated droplets of binary liquid mixtures. *International Journal of Heat and Fluid Flow*, 23:471–486, 2002.

[129] W. Zeng, M. Xu, Y. Zhang, and Z. Wang. Laser sheet dropsizing of evaporating sprays using simultaneous LIEF/MIE techniques. *Proceedings of the Combustion Institute*, 34:1677–1685, 2013.

[130] Y. Zhang, R. Huang, Y. Huang, S. Huang, Y. Ma, S. Xu, and P. Zhou. Effect of ambient temperature on the puffing characteristics of single butanol-hexadecane droplet. *Energy*, 145:430–441, 2018.

[131] Y. Zhang, S. Li, B. Lin, Y. Liu, J. Wu, and B. Xu. A review on laser diagnostics on atomization and evaporation of liquid fuel. In *International Conference on Optical Particle Characterization (OPC 2014)*, volume 9232, page 923202. SPIE, 2014.

[132] Z. Zhifu, W. Guoxiang, C. Bin, G. Liejin, and W. Yueshe. Evaluation of evaporation models for single moving droplet with a high evaporation rate. *Powder technology*, 240:95–102, 2013.

# APPENDIX A

# CHANGE IN GAS PROPERTIES IN 2D STAGNATION FLAME SIMULATIONS

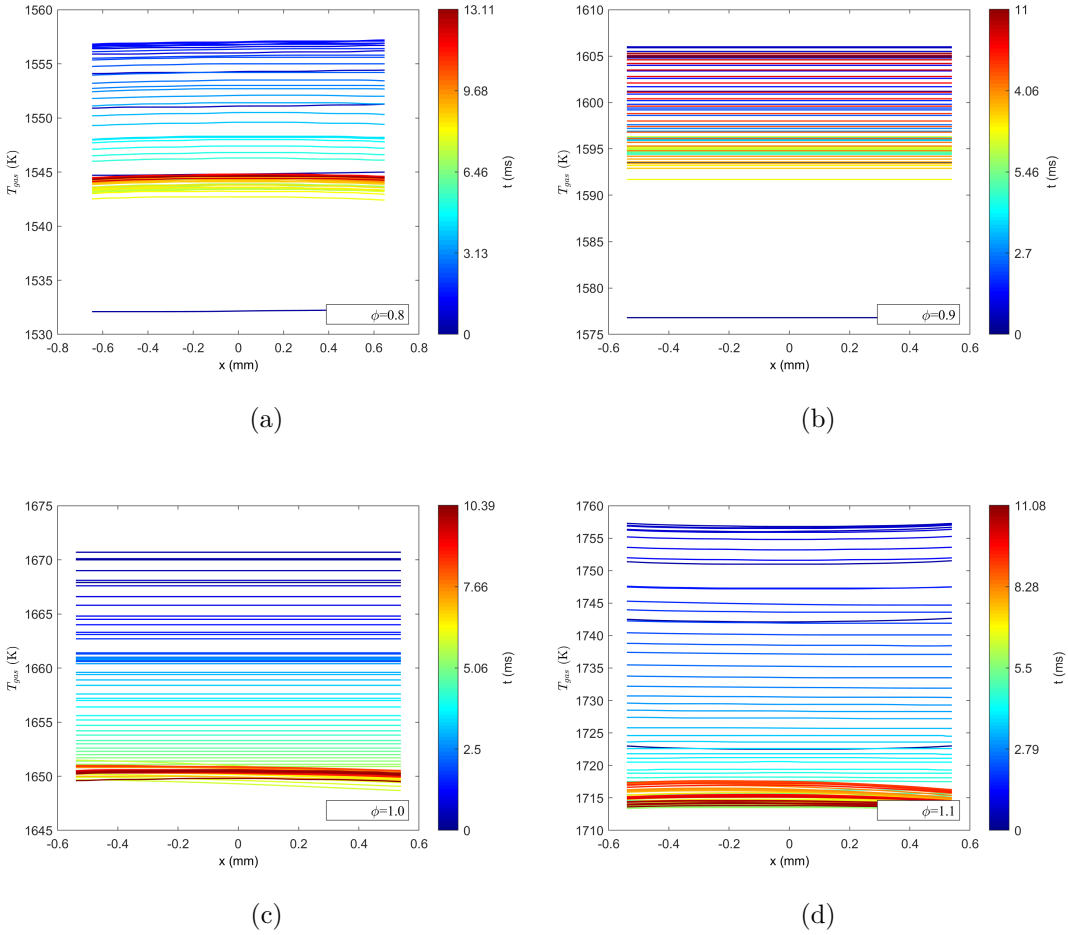


Figure A.1: Variation in gas temperature at the flame over time.

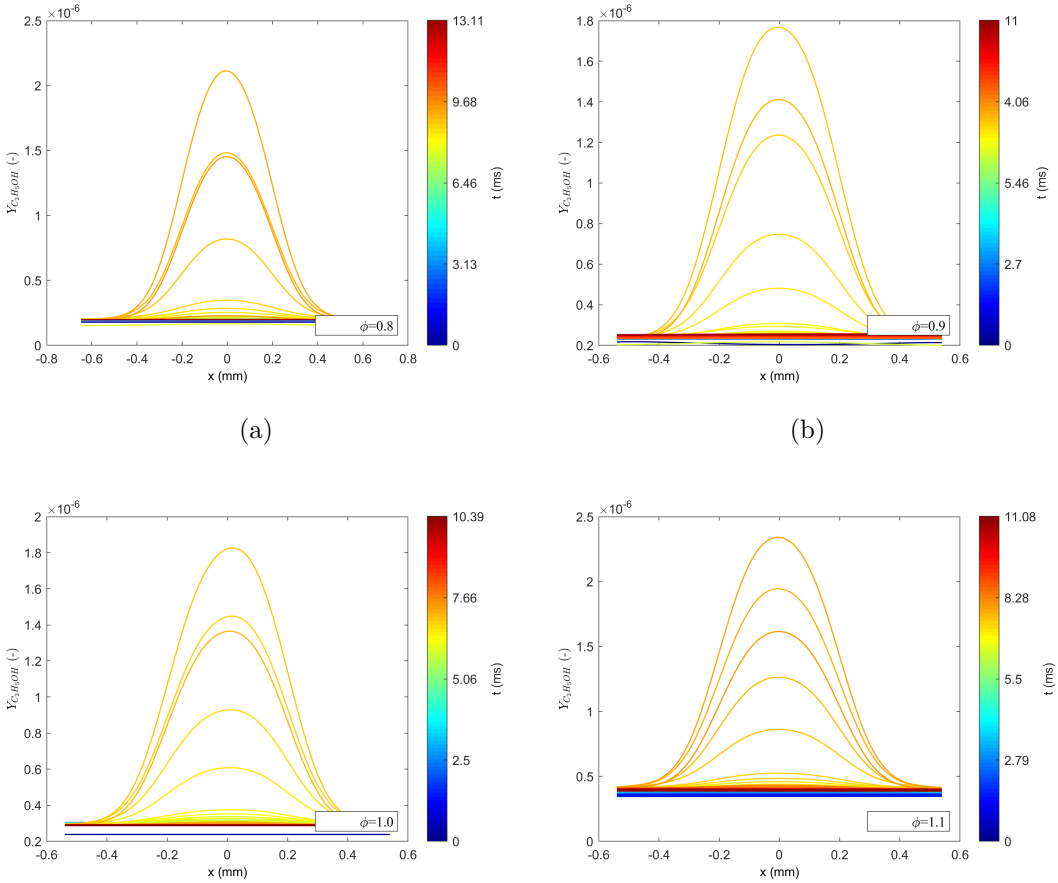


Figure A.2: Variation in $C_2H_5OH$ mass fraction at the flame over time.

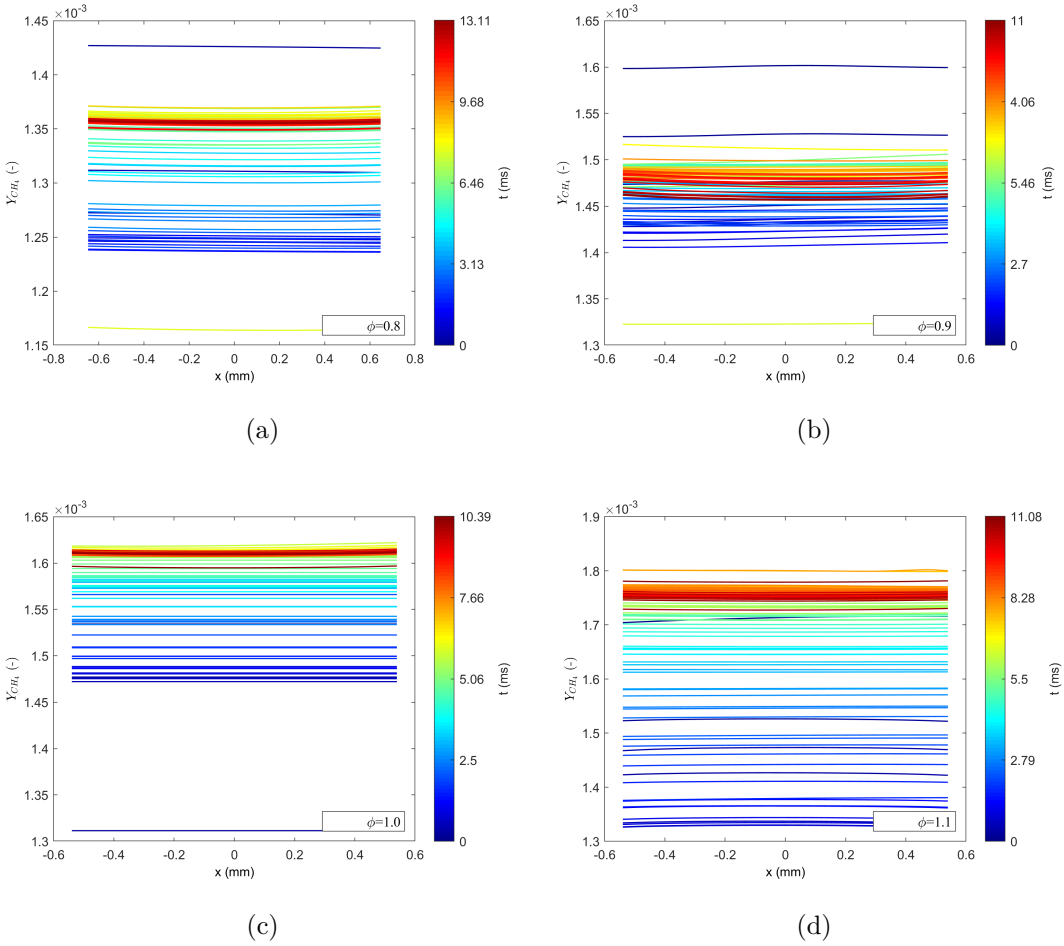


Figure A.3: Variation in $CH_4$ mass fraction at the flame over time.

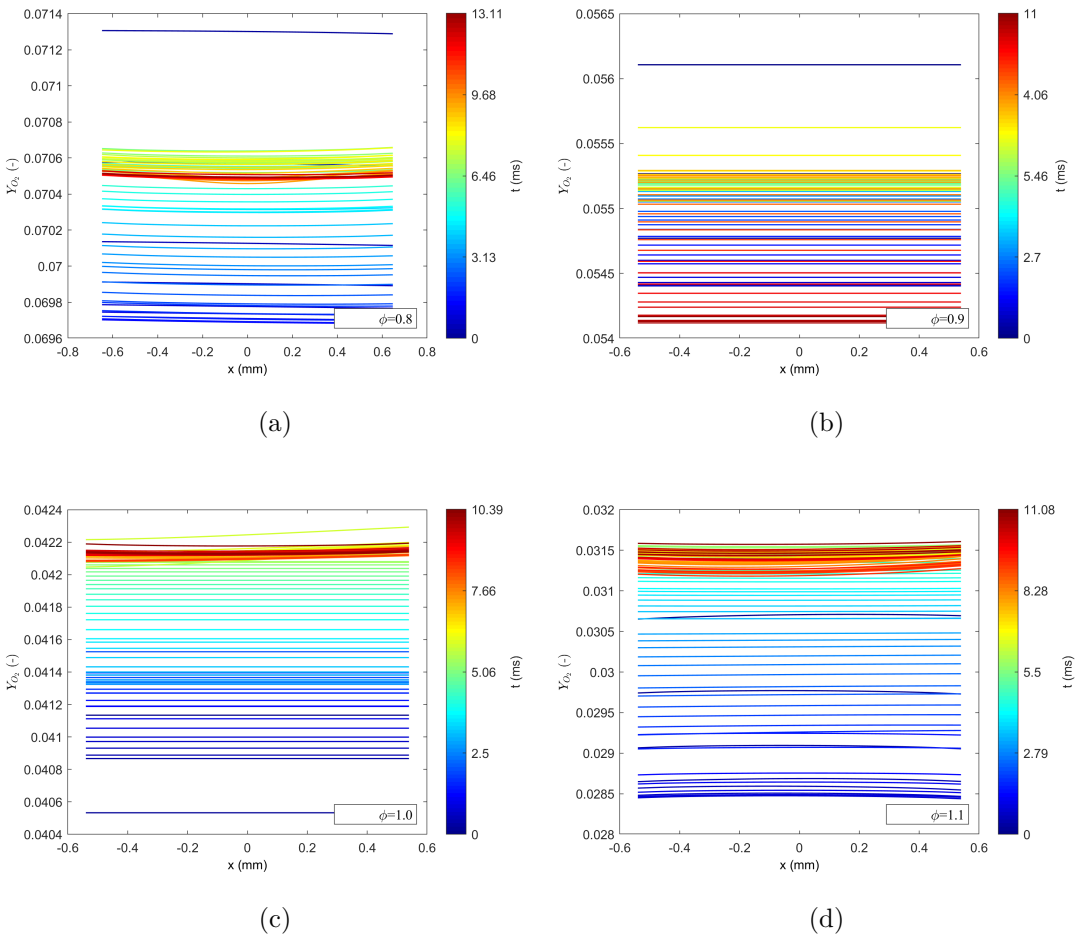


Figure A.4: Variation in $O_2$ mass fraction at the flame over time.

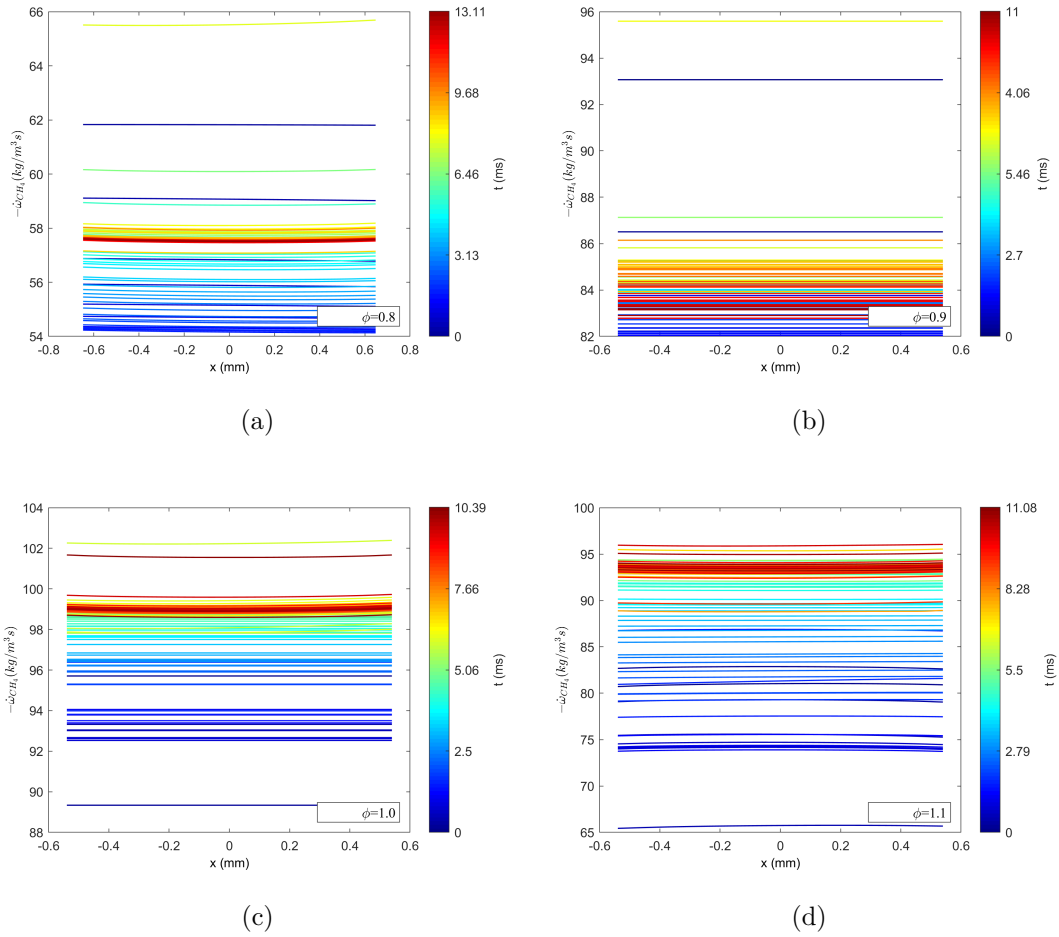


Figure A.5: Variation in $CH_4$ reaction source term at the flame over time.

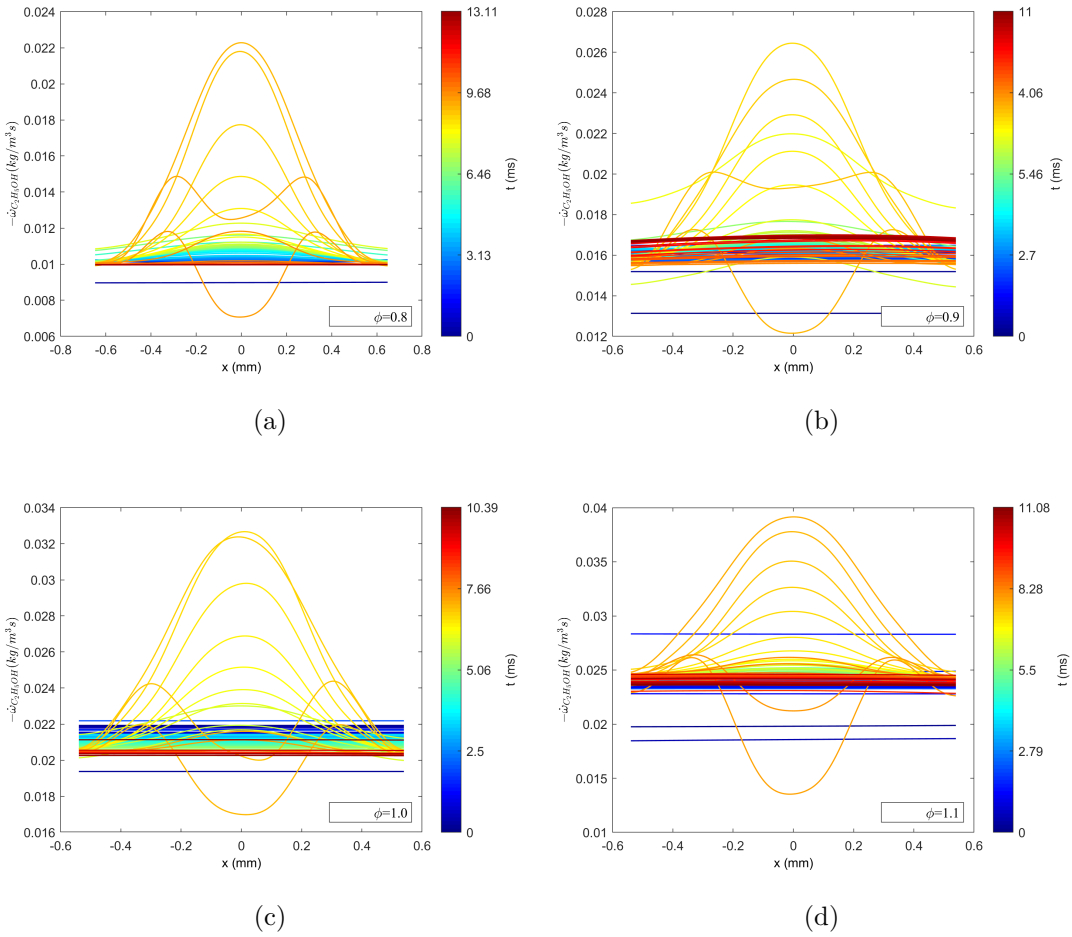


Figure A.6: Variation in $C_2H_5OH$ reaction source term at the flame over time.

**Deniz KAYA EYICE**

# Etude des interactions entre gouttelette et flamme par des approches expérimentales et numériques

Résumé :
Les applications de combustion par pulvérisation impliquent des phénomènes très complexes tels que l'atomisation, la vaporisation des gouttelettes, le mélange, la turbulence, la cinétique chimique, ainsi que l'interaction de ces processus. Dans la combustion diphasique, l'un des processus de base est l'interaction d'une seule gouttelette avec une flammelette. Par conséquent, il est essentiel de comprendre la physique de l'évaporation des gouttelettes isolées et des effets sur le front de flamme pour étudier des flammes plus complexes.

Le but de cette étude est d'étudier l'évaporation des gouttelettes, les caractéristiques de la flamme et les changements sur la morphologie de la flamme pour les flammes laminaires en présence de gouttelettes via des approches expérimentales et numériques. La partie expérimentale de l'étude est menée au CNRS ICARE, y compris des expériences de microgravité pour étudier les instabilités de flamme en présence de gouttelettes d'éthanol isolées pour une flamme éthanol/air à expansion sphérique à l'aide de la méthode Schlieren et des expériences au sol pour étudier les caractéristiques d'évaporation d'une gouttelette d'éthanol traversant une flamme stabilisée contre une plaque. Les modifications induites par le passage de la goutte dans la flamme sont détaillées à l'aide de différents diagnostics optiques tels que PIV, PTV, ILIDS et Chimiluminescence. Dans la partie numérique de l'étude, le solveur YALES2 est utilisé pour simuler l'évaporation des gouttelettes dans différentes conditions ambiantes à des températures élevées via une approche Eulérienne-Lagrangienne. Dans ce cadre, l'évaporation des gouttelettes stationnaires est calculée aux compositions de gaz brûlés via le modèle de Spalding, ainsi que l'évaporation d'une gouttelette en mouvement à travers un champ de flamme de stagnation via le modèle d'Abramzon-Sirignano. Enfin, des simulations non réactives et réactives sont réalisées avec une géométrie de brûleur à stagnation réelle.

Mots clés : combustion diphasique, interactions gouttelette/flamme, instabilité de la flamme, évaporation

# Investigation of droplet flame interactions through experimental and numerical approaches

Summary :
Spray combustion applications involve complex phenomena such as atomization, droplet vaporization, mixing, turbulence, chemical kinetics, and the interaction of these processes. In two-phase combustion, one of the fundamental processes is the interaction of a single droplet with a flamelet. Therefore, it is essential to understand the physics of isolated droplet evaporation and its effects on the flame front to study more complex flames.

The aim of this study is to investigate droplet evaporation, flame characteristics, and changes in the flame morphology for laminar flames in the presence of droplets via experimental and numerical approaches. The experimental part of the study is conducted in CNRS ICARE, including microgravity experiments to study the flame instabilities of spherically expanding ethanol/air flame in the presence of isolated ethanol droplets using the Schlieren method. Additionally, ground experiments are performed to investigate the evaporation characteristics of an ethanol droplet evaporating through flat methane/air flame and the structural changes in propane/air flames due to the passage of an ethanol droplet using optical laser diagnostics including PIV, PTV, ILIDS, Chemiluminescence. In the numerical part of the study, the YALES2 solver is utilized to simulate droplet evaporation under different ambient conditions at elevated temperatures via the Eulerian-Lagrangian approach. In this scope, stationary droplet evaporation is computed at burnt gas compositions via the Spalding model, as well as the evaporation of a moving droplet through a stagnation flame field via the Abramzon-Sirignano model. Finally, nonreactive and reactive simulations are performed with stagnation burner geometry.

Keywords : multiphase combustion, droplet/flame interactions, flame instabilities, evaporation

**Institut de Combustion Aérothermique**
**Réactivité et Environnement**
**UPR 3021 du CNRS**
**1C, avenue de la Recherche Scientifique**
**45071 Orléans, Cedex 2**